**Title**
Laboratory Studies of Nonlinear and Breaking Surface Waves

**Author**
Drazen, David

**Publication Date**
2006

UNIVERSITY OF CALIFORNIA, SAN DIEGO

# Laboratory Studies of Nonlinear and Breaking Surface Waves

A dissertation submitted in partial satisfaction of the
requirements for the degree Doctor of Philosophy
in
Oceanography

by

David Drazen

Committee in charge:

W. Kendall Melville, Chair
Robert T. Guza
Paul F. Linden
Michael S. Longuet-Higgins
Daniel L. Rudnick
Sutanu Sarkar

2006

The dissertation of David Drazen is approved, and it is acceptable in quality and form for publication on microfilm:

Chair

University of California, San Diego

2006

For my parents, Jeffrey and Erica,
and my wife Genevieve.

## TABLE OF CONTENTS

# LIST OF SYMBOLS

Chapter II

| | |
|---|---|
| $a$ | Wave amplitude |
| $ak$ | Wave slope |
| $c$ | Wave phase speed |
| $f$ | Wave frequency |
| $g$ | Gravitational acceleration |
| $G$ | Gain factor |
| $\rho$ | Density |
| $\sigma$ | Radian wave frequency |
| $\tau$ | Dimensionless time |
| $T$ | Wave period |
| $\zeta$ | Wave elevation |

Chapter III

| | |
|---|---|
| $a$ | Wave amplitude |
| $a_H$ | Hinze scale |
| $b$ | Breaking parameter |
| Bo | Bond number |
| $C_g$ | Group velocity |
| $\chi$ | Normalized dissipation rate |
| $d$ | Bubble diameter |
| $\epsilon_l$ | Dissipation rate per unit length of crest |
| $\epsilon_m$ | Dissipation rate per unit mass |
| $\eta$ | Surface elevation |
| $f$ | Wave frequency |
| $F$ | Energy flux |
| $g$ | Gravitational acceleration |

| | |
|---|---|
| $\gamma$ | Surface tension |
| $\Gamma$ | Surface tension |
| $h$ | Height of the breaking region |
| $k$ | Wavenumber |
| $\lambda$ | Wavelength |
| $L$ | Length of the spilling breaker |
| $\mu_w$ | Viscosity of water |
| $\mu_a$ | Viscosity of air |
| $N$ | Action spectral density |
| $\nu$ | Kinematic viscosity |
| $\phi_n$ | Phase of wave packet component |
| $\psi$ | Energy spectral density |
| Re | Reynolds number |
| $\mathrm{R}_\lambda$ | Taylor microscale Reynolds number |
| $\rho$ | Density of water |
| $\rho'$ | Fluid density in the breaking region |
| $\rho_w$ | Density of water |
| $\rho_a$ | Density of air |
| $\sigma$ | Radian wave frequency |
| $S$ | Input slope |
| $\tau$ | Shear stress |
| $t_b$ | Time of breaking |
| $t$ | Time |
| $\tau$ | Duration of breaking |
| $T$ | Wave period |
| $\theta$ | Angle of inclination above horizontal |
| $u, v, w$ | Cartesian velocity components |
| $u_*$ | Friction velocity |
| $x_b$ | Breaking location |

| | |
|---|---|
| $x, y, z$ | Cartesian coordinates |
| We | Weber Number |

Chapter IV

| | |
|---|---|
| $A$ | Area of the breaking region |
| $a$ | Wave amplitude |
| $b$ | Breaking parameter |
| $C_g$ | Group velocity |
| $C_c$ | Phase speed of center wave component |
| $\epsilon$ | Dissipation rate |
| $\epsilon_l$ | Dissipation rate per unit length of crest |
| $\epsilon_m$ | Dissipation rate per unit mass |
| $\eta$ | Surface elevation |
| $\eta$ | Kolmogorov lengthscale |
| $E_{11}, E_{33}$ | Wavenumber spectra |
| $E_m$ | Kinetic energy density of the mean flow |
| $E_t$ | Turbulent kinetic energy density |
| $f$ | Wave frequency |
| $g$ | Gravitational acceleration |
| $H$ | Depth of the fluid |
| $k$ | Wavenumber |
| $k$ | TKE density per unit mass |
| $\lambda$ | Wavelength |
| $\lambda_f$ | Taylor microscale |
| $L_{11}$ | Integral lengthscale |
| $M$ | Momentum |
| $\nu$ | Kinematic viscosity |
| $q$ | TKE density |
| $p$ | Pressure |

| | |
|---|---|
| $\phi_n$ | Phase of wave packet component |
| $\Psi$ | Streamlines |
| $\Psi_{11}$ | Compensated wavenumber spectrum |
| Re | Reynolds number |
| $\mathrm{Re}_\lambda$ | Taylor microscale Reynolds number |
| $\rho$ | Density of water |
| $\sigma$ | Radian wave frequency |
| $S$ | Input slope |
| $S_{ij}$ | Mean strain rate tensor |
| $s_{ij}$ | Fluctuating rate of strain tensor |
| $t_b$ | Time of breaking |
| $\tau_t$ | Decay timescale of the turbulence |
| $t$ | Time |
| $t^*$ | Non-dimensional time since breaking |
| $T$ | Wave period |
| TKE | Turbulent kinetic energy density |
| $u, v, w$ | Cartesian velocity components |
| $\mathcal{W}$ | Mean square vorticity |
| $x_b$ | Breaking location |
| $x^*$ | Non-dimensional distance from breaking |
| $x, y, z$ | Cartesian coordinates |

# LIST OF FIGURES

# LIST OF TABLES

# ACKNOWLEDGMENTS

I would like to begin with expressing my gratitude to Ken Melville for his guidance, insight, and support during my time as a graduate student. His trust and confidence in my abilities has allowed me to grow and accomplish much more than I thought was possible. The scope of Ken's knowledge continues to amaze me and I only hope that I can provide for others in the future as he has done for me. I would also like to thank the members of my committee, Bob Guza, Paul Linden, Michael Longuet-Higgins, Dan Rudnick, and Sutanu Sarkar for providing me with helpful comments and suggestions on my work. My graduate school career was spent conducting experiments in the Hydraulics Laboratory and anyone who has worked there has encountered Dave Aglietti, John Lyons, and Charly Coughran. I owe a large debt of gratitude to them, their help in setting up experiments has been incredible. I would like to thank John especially for his uncanny ability to build me whatever contraption was needed to complete the job at hand, no matter what the time frame. Mike Kirk and Skip Mikuls also lent me a huge hand when it came to electronics, specifically the interface to the wave paddle. Their help was greatly appreciated. I would also like to thank Grant Deane and Dale Stokes for their flexibility in allowing me to finish up needed experiments and for lending me the hydrophone I used in Chapter III.

I also need thank everyone I've encountered during my time here in both Ken's and Eric Terrill's research groups. Thanks to Peter Matusov, Mike Ritter, Ronan Gray, Fabrice Veron, Genevieve Lada, Axel Pierson, Joel Hazard, Lisa Hazard, Mark Otero, Luc Lenain, Jim Lasswell, Jessica Kleiss, and Leonel Romero. Joel helped me get an underwater housing constructed at the last minute so I could perform the underwater DPIV measurements described in Chapter IV. Luc showed up at the tail end of my time here and not only helped with some experimental setup, but served as a sounding board for various ideas. Our discussions on PIV and related measurements have been especially enlightening. Eric Terrill has also been a source of support in terms of both equipment and needed encouragement. Ronan Gray shared an office with me during my first few years in the lab and helped to keep me sane during classes. A special

thanks goes out to Fabrice. He was the first person I met when arrived at SIO as a summer student in 1998. His encouragement and enthusiasm that he had convinced me to return to conduct laboratory work at Scripps with Ken. Ever since then he has answered my many questions, helped me along, been a source of support, and introduced me to Aoinagi karate. While I was in the midst of my laboratory experiments we had a visitor in our lab, Atle Jensen, who was on sabbatical from the University of Oslo. We worked on some projects together and he assisted me in setting up and validating my PIV experiments. His friendship and help is greatly appreciated and I look forward to further collaboration in the future.

My family has been a tremendous source of support and inspiration over the years. To put into words all that they have done could easily fill a volume of itself. I have fond memories of time spent on Nantucket Island with my brother, parents, grandparents, and aunt and uncle. It is during these times that I began to explore the world around me and which fostered my interest in science. I have been truly lucky to have such a wonderful and loving family, they have done so much for me over the years, and I wish to thank them all for everything they have done. I met my wife, Genevieve, in March of 2001 and my life has not been the same since. She has been a tremendous source of support, and despite her non-scientific background has tried her best to understand any problems and help me along when I was stuck. She kept me company during long nights of experimenting, made sure I was fed and focused during the difficult times, and helped me with the illustrations. Her love and support have been tremendous and I thank her for that. In addition I would like to thank Genna's parents and her extended family. They have taken me in as one of their own and provided me with love and support.

Chapter II, in full, is a reprint of the material as it appears in "On steep gravity waves meeting a vertical wall: a triple instability." Longuet-Higgins, M.S. and Drazen, D.A., *Journal of Fluid Mechanics*, **466**, 305–318, 2002. The dissertation author contributed to this work by collecting and handling the experimental data. Michael S. Longuet-Higgins provided the theory, assisted and directed the experimental work, and wrote the paper.

# VITA

| | |
|---|---|
| 1999 | B.A., Earth and Planetary Science,<br>Johns Hopkins University |
| 1999–2006 | Research Assistant<br>Scripps Institution of Oceanography,<br>University of California, San Diego |
| 2006 | Ph.D., Physical Oceanography<br>Scripps Institution of Oceanography,<br>University of California, San Diego. |

# PUBLICATIONS

Longuet-Higgins, M.S., and Drazen, D.A., 2002: On steep gravity waves meeting a vertical wall: a triple instability. *J. Fluid Mech.*, **466**, 305–318.

# PRESENTATIONS

Drazen, D.A. and M.S. Longuet-Higgins, 2001: On steep gravity waves meeting a vertical wall, *54th Annual Meeting of the American Physical Society's Division of Fluid Dynamics*, San Diego, CA, USA.

Drazen, D.A. and W.K. Melville, 2005: Turbulence measurements under unsteady deep-water breaking waves, *58th Annual Meeting of the American Physical Society's Division of Fluid Dynamics*, Chicago, IL, USA.

# FIELDS OF STUDY

Studies in Physical Oceanography
Professors M. Hendershott and L. Talley

Studies in Fluid Mechanics
Professor C. Winant

Studies in Mathematics
Professors G. Ierley, B. Young, and R. Salmon

Studies in Data Analysis
Professors R. Pinkel, R. Davis, and D. Rudnick

Studies in Large Scale Ocean Observations
Professor D. Roemmich

Studies in Linear and Non-Linear Waves
Professors M. Hendershott, R. Guza, and W.K. Melville

Studies in Dynamical Oceanography
Professors P. Cessi and P. Niiler

Studies in Acoustics
Professor W. Kuperman

Studies in Turbulence
Professor S. Sarkar

Studies in Biological Oceanography
Professor P. Franks

# ABSTRACT OF THE DISSERTATION

## Laboratory Studies of Nonlinear and Breaking Surface Waves

by

David Drazen
Doctor of Philosophy in Oceanography
University of California, San Diego, 2006
Professor W. Kendall Melville, Chair

A laboratory investigation of nonlinear and breaking surface waves is presented in two parts. The first focuses on the instability of progressive surface gravity waves incident on a vertical wall and the second on the measurement of the kinematics and dynamics of breaking progressive waves and the turbulence they generate.

In Part I, Theoretical arguments suggest that progressive gravity waves incident on a vertical wall can produce periodic standing waves only if the incident wave steepness $ak$ is quite small. Laboratory experiments are carried out in which an incident wave train of almost uniform amplitude meets a vertical barrier. When $ak > 0.236$, a growing instability is observed in which every third wave crest is steeper than its neighbours. The instability grows by a factor of about 2.2 for every three wave periods, almost independently of the incident wave steepness.

In Part II, the measurement of the dissipation of wave energy by breaking over a significant range of parameter space allows the kinematics of breaking to be related to the underlying dynamics. Control volume analysis yields a measure of the change in energy flux across the volume and is related to the dissipation through the duration of active breaking. Assuming the plunging wave toe follows a ballistic trajectory, an inertial estimate of the dissipation is developed and found to predict the dissipation rate within an order of magnitude.

Detailed measurements of the post-breaking velocity field using DPIV are conducted in the longitudinal and transverse planes. Statistical measures of the turbulence are presented. Separation of the surface-wave induced velocity from the full measured velocity helps isolate the effects of breaking, including the generation of coherent vorticity. Turbulent wavenumber spectra exhibit a deviation from the inertial subrange at high wavenumbers, thought to be caused by an imbalance between the flux of energy from large scales and the dissipation at small scales. Measurements of terms in the turbulent kinetic energy density equation are presented. The relationship between the three-dimensional turbulent kinetic energy density and two-dimensional approximations are discussed. A comparison between various estimates of the rate of viscous dissipation is also given.

# Chapter I

# Summary

The research conducted for this dissertation is focused on laboratory studies of surface waves. The work can be broken into two parts, the first on the formation of an instability in standing waves generated by progressive waves incident upon a vertical wall, and the second on the kinematics and dynamics of a breaking progressive wave. Each chapter was written to be freestanding and thus has an introduction and review relevant to the topic followed by a discussion of the results.

In Part I, standing waves generated by progressive waves incident upon a vertical wall are discussed. Theoretical arguments suggest that progressive gravity waves incident on a vertical wall can produce periodic standing waves only if the incident wave steepness $ak$ is quite small, certainly less than 0.284. Laboratory experiments are carried out in which an incident wave train of almost uniform amplitude meets a vertical barrier. At wave steepnesses greater than 0.236 the resulting motion near the barrier is non-periodic. A growing instability is observed in which every third wave crest is steeper than its neighbours. The steep waves develop sharp crests, or vertical jets. The two neighbouring crests are rounded, flat-topped, or of intermediate form. The instability grows by a factor of about 2.2 for every three wave periods, almost independently of the incident wave steepness. This part of the dissertation is presented in Chapter II and consists of a reprint in full of the material contained in Longuet-Higgins and Drazen (2002). For the material in Chapter II, Michael S. Longuet-Higgins provided the theory and directed and assisted in the experiments. The experimental data was collected and handled by the author of this dissertation. The paper which comprises the material of Chapter II was written by Michael S. Longuet-Higgins.

In Part II, which comprises the major portion of this dissertation, the focus is on breaking progressive waves. The dynamics of breaking waves play a significant role in the air-sea boundary layer. The breaking process transfers momentum to the upper ocean from the surface waves generating currents. Breaking waves are intermittent in both time and space which makes field measurements difficult. The environments in which large-scale breaking occurs in the field are not hospitable nor conducive to making detailed measurements. Laboratory measurements of wave breaking allow for measurements of the dynamics of breaking with a high degree of control over the initial-conditions. The laboratory provides a connection between the kinematics and dynamics of breaking which will help to further our understanding of the breaking process.

Chapter III describes the measurement of the dissipation rate from breaking over a significant range of parameter space. The normalized dissipation rate is given by

$$b = \frac{\epsilon_l g}{\rho c^5} \tag{I.1}$$

where $\epsilon_l$ is the dissipation rate per unit length of wave crest, $g$ acceleration due to gravity, $\rho$ density, and $c$ the phase speed. The estimates of $b$ in the literature have varied over an order of magnitude from $O(10^{-4})$ in the field (Phillips, Posner, and Hansen, 2001) to $O(10^{-2})$ for quasi-steady breaking in the laboratory (Duncan, 1981, 1983). Estimates of $b$ from unsteady breaking (Melville, 1994) indicate that there is a dependence of $b$ on the slope of the waves as opposed to previous studies which found it to be approximately constant.

The amount of energy lost by unsteady breaking is measured through a control volume analysis. If the ends of the control volume are far enough away from breaking the packet can be considered to be weakly non-linear at those locations and we can apply equipartition of energy. The dissipation rate is then defined to be the energy lost over the duration of active breaking as measured acoustically using a hydrophone.

The path of a breaking wave toe is shown to be described by a ballistic trajectory and the velocity is then related to the distance over which the wave toe falls. An inertial estimate of the dissipation rate, $\epsilon$, of plunging breaking is presented, where $\epsilon \approx u^3/l$, $u$ is a velocity scale and $l$ a length scale related to the energy-containing or largest scales of the flow. The dependence on the slope of the dissipation as predicted by this model is found to agree well with the experimentally measured dissipation rate. A similar argument is used for spilling waves, scaling the velocity using the friction velocity and the length by the vertical distance over which the breaking is occurring. The spilling wave model provides an explanation for differences in $b$ seen between quasi-steady and unsteady spilling breaking waves.

Chapter IV describes the measurement of the post-breaking velocity field using DPIV in both longitudinal and transverse planes. The measurements in the longitudinal plane are conducted with a field of view of 2 m x 0.6 m, which permits measurement of the entire turbulent cloud as it evolves in time. This is contrasted with previous work in which the turbulent region was imaged using a mosaic of windows of size O(10cm × 10cm). Ensemble-averaged quantities of the turbulence are presented for selected times after breaking in both planes.

Using the spatial Fourier transform of the surface elevation allows us to compute the theoretical velocity of the surface waves as given by a 2nd order Stoke's expansion. The removal of the surface-wave induced velocity from the velocity field measured by breaking helps to isolate the effects of breaking, including the generation of coherent vorticity. The length of the breaking region increases rapidly and the depth of the mixing follows a $x^{1/2}$ dependence, from which an estimate of the eddy viscosity, $\nu_T$ can be obtained.

Wavenumber spectra of the velocity are measured and for times shortly after breaking a large inertial subrange is seen. For later times there is evidence of a "bump" in the spectra near the high-wavenumber end of the inertial subrange. This bump has been seen previously in both field measurements (Doron, Bertuccioli, Katz, and Osborn, 2001; Nimmo Smith, Katz, and Osborn, 2005) and laboratory measurements (Saddoughi and Veeravalli, 1994). This phenomenon is attributed to a "bottleneck" effect in which the flux of energy from large scales exceeds the rate at which the energy can be dissipated by the small scales leading to a pileup of energy at the intermediate scales.

The experimental configuration used allows us to compute the full three-dimensional turbulent kinetic energy density at four vertical lines within the flow. We compare estimates of the three-dimensional turbulent kinetic energy density with that collected only in the longitudinal plane, allowing us to determine an appropriate scaling for the two-dimensional estimate of the turbulent kinetic energy. Selected terms in the turbulent kinetic energy density are also shown and the turbulent transport term is seen to be significant for times soon after breaking. Integral measures of the dissipation rate are also presented and compared with the inferred dissipation rate from the volume-integrated turbulent kinetic energy equation, in which a balance between evolution, production, and dissipation occurs. An estimate of the normalized dissipation rate $b$, as computed using the momentum flux from the surface waves to the fluid is conducted and found to agree with the value predicted by the model presented in Chapter III.

# Chapter II

# On steep gravity waves meeting a vertical wall: a triple instability

## II.1 Abstract

Theoretical arguments suggest that progressive gravity waves incident on a vertical wall can produce periodic standing waves only if the incident wave steepness *ak* is quite small, certainly less than 0.284. Laboratory experiments are carried out in which an incident wave train of almost uniform amplitude meets a vertical barrier. At wave steepnesses greater than 0.236 the resulting motion near the barrier is non-periodic. A growing instability is observed in which every third wave crest is steeper than its neighbours. The steep waves develop sharp crests, or vertical jets. The two neighbouring crests are rounded, flat-topped, or of intermediate form. The instability grows by a factor of about 2.2 for every three wave periods, almost independently of the incident wave steepness.

## II.2 Introduction

Surface gravity waves of low amplitude, when reflected from a vertical wall, will produce standing waves of double the amplitude of the incident waves. If on the other hand the incident waves are steep enough, they are found to throw up vertical jets of water against the reflecting barrier; see for example Chan and Melville (1988). The same phenomenon is often observed when incoming waves meet a cliff or harbour wall. Moreover, this is not merely a shallow-water phenomenon but occurs also in deep water. As will be seen below, it follows from a simple energy argument that progressive waves of more than a certain steepness *cannot* produce periodic standing waves; they must be aperiodic.

In his well-known experiments on steep standing waves Sir Geoffrey Tayor (1954) considered only periodic waves, whose maximum slope he found to be about 45°. In accurate computations Mercer and Roberts (1992) showed that periodic standing waves of given wavelength cannot have more than a certain energy, although at energies slightly below that maximum two different periodic waves having the same energy can exist. Jiang, Perlin, and Schultz (1998) have carried out experiments on deep-water standing waves forced subharmonically by a vertical oscillation of the wave tank. It was shown that the waves could be made to break periodically once every three wave "periods." Numerical studies of "super-energetic" standing waves, with various initial conditions, have been carried out by Longuet-Higgins and Dommermuth (2001a,b) and it was found that either single jets could be produced, which fell back vertically into the trough of the wave, creating a semi-circular cavity; or in other cases, starting with a circular cavity, the wave crests could become flat-topped and then break on either side of the wave crest, like a pair of spilling or plunging breakers.

The purpose of the present paper is to describe experiments in which free progressive waves are allowed to impinge on a vertical wall, and the complete history of the motion is then followed. There is no forcing of the wave motion by a vertical or other kind of oscillation of the boundary, apart from the remote wavemaker. It is found that when the steepness *ak* of the incident wave train exceeds about 0.236 the waves in the neighbourhood of the boundary develop a growing instability in which every third wave (in time) is the steepest, the two intermediate waves having flat-topped or rounded crests, or of a mixed type. The steepest waves become sharp-crested; see Section II.6.

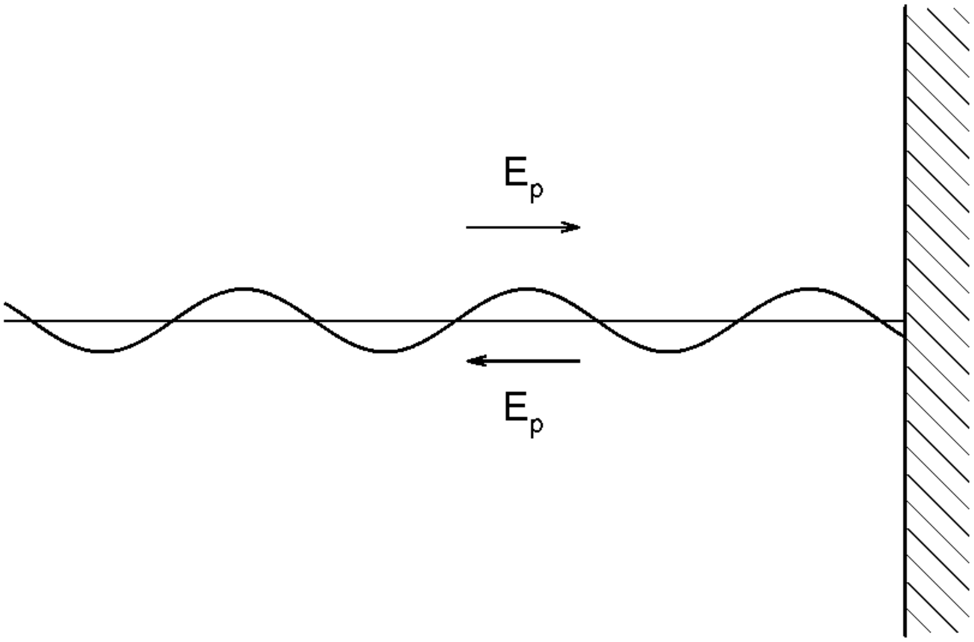

Figure II.1: Reflection of a progressive wave from a vertical wall, when the maximum surface slope is small.

A discussion and conclusions follow in Section II.7.

## II.3 Energy and periodicity

Some general conclusions may be drawn immediately from a consideration of the total energy density of the waves; see Figure II.1.

Let $E_p$ denote the mean energy density of the incident progressive wave, averaged over time and horizontal distance. On the *linearised* theory of surface waves, in which the surface slopes are small, we have

$$E_p = \frac{1}{2}\rho g a^2 \tag{II.1}$$

where $\rho$ is the density, $g$ the acceleration of gravity and $a$ the wave amplitude. The reflected wave is similar, and the two waves combine to form a standing wave of maximum amplitude $2a$ (crest-to-trough height $4a$) and of time-averaged energy

$$E_s = 2E_p. \tag{II.2}$$

Hence

$$E_p = \frac{1}{2}E_s. \tag{II.3}$$

On the linearised theory there is no limit to either $E_p$ or $E_s$, assuming the wavelength $L$ to be fixed. However on the fully *nonlinear* theory of gravity waves the total energy $E_s$ of a standing wave has a maximum given by

$$(E_s)_{\max} = 0.07774 \tag{II.4}$$

in units where $\rho$, $g$ and the wavenumber $k$ are all unity; see Mercer and Roberts (1992). Hence, if we assume that all the energy of the incident and the reflected wave go to form a periodic standing wave, and if we ignore the contribution of the higher harmonics to the total energy (but not to the surface profile), then we must have

$$E_p \leq \frac{1}{2}(E_{s\,\max}) = E_{crit} \tag{II.5}$$

say, where from (II.4)

$$E_{crit} = 0.03887. \tag{II.6}$$

If on the other hand $E_p > E_{crit}$ we see that the resulting motion cannot be periodic.

Now a plot of the energy density $E_p$ of a progressive wave against its steepness $ak$ (Figure II.2) shows that a progressive wave may have an energy as great as

$$(E_p)_{\max} = 0.0745 \tag{II.7}$$

which is achieved when

$$ak = 0.429. \tag{II.8}$$

The maximum wave steepness $ak$ for a progressive wave is 0.4432. So from Figure II.2 and equation (II.6) there is a certain range of progressive wave steepnesses, namely

$$0.285 < ak < 0.443 \tag{II.9}$$

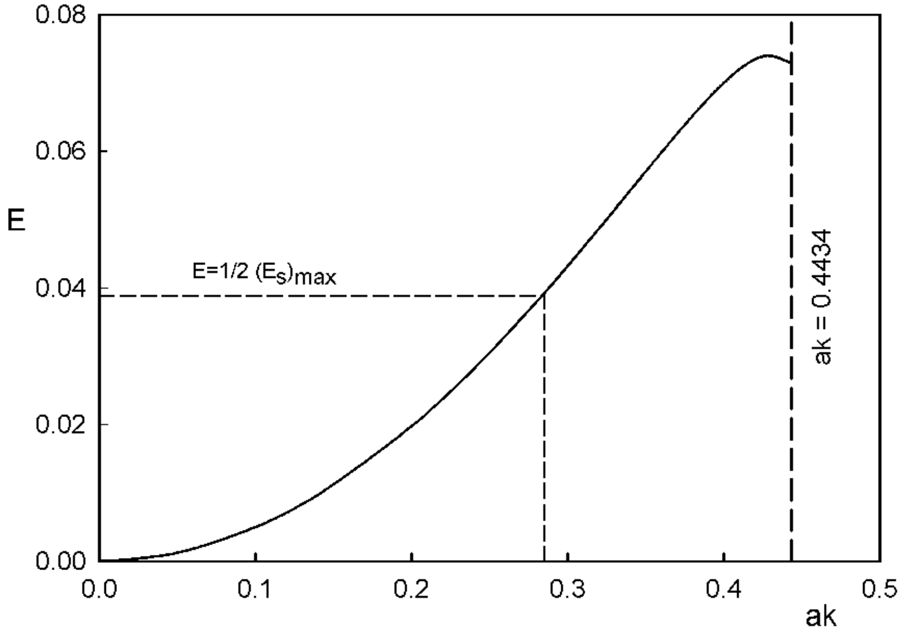

Figure II.2: Graph of the energy density $E_p$ of a progressive gravity wave of finite steepness $ak$.

for an incident wave, such that the incident-plus-reflected wave system cannot be a perfectly periodic standing wave. The resulting motion must be irregular or chaotic in some way, leading possibly to breaking.

Incident progressive waves whose steepness lies in the range $0 < ak < 0.285$ we shall call *subcritical*, while those that lie in the range (II.8) we shall call *supercritical*. It is not of course implied that all subcritical incident waves will necessarily produce motions that are perfectly periodic. This is a matter for experiment.

## II.4 Experimental apparatus

The experiments were carried out in a glass-sided wave tank in the Hydraulics Laboratory at the Scripps Institution of Oceanography. A sketch is shown in Figure II.3.

A computer-controlled, horizontal-movement wavemaker was at $A$, and an impervious, sloping beach with gradient 1:10 was at $C$. A removeable plane wall, or

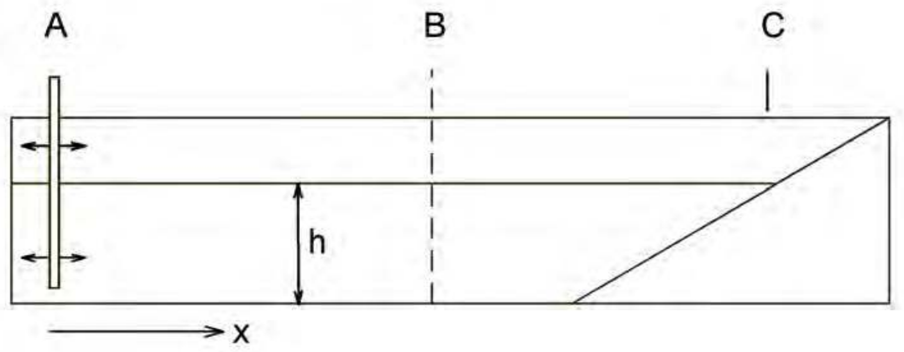

Figure II.3: Sketch of the wave tank.

barrier, was inserted at $B$. The distances $AB$ and $AC$ were 15.65 m and 26.96 m respectively. The width $W$ of the tank and the stillwater depth $h$ were both equal to 0.50 m.

The vertical displacement of the water surface was measured with resistence-wire gauges, each consisting of two parallel vertical wires separated by 0.3 cm and oriented across the tank at $B$, near the mid-plane of the wave tank. With the barrier in place, the wires were 2 mm from the surface of the wall. Calibration before and after each run indicated that the gauges were linear to within about 1 percent over the range of measurement. The output from the gauges was digitised and recorded at a rate of 100 Hz.

A video recording of the surface at a rate of 30 frames/s was made from a position slightly above the mean water level and to the left (wave side) of the barrier. Blue vegetable dye added to the water was used to increase the contrast between air and water, the background on the far wall being white.

## II.5 Procedure

The experiments were conducted at a wave frequency $f = 1.0$ or $1.1 s^{-1}$, which is somewhat less than the cut-off frequency ($1.25 s^{-1}$) for the lowest-order 3-dimensional waves in a channel of width 0.5 m. Nevertheless, after a certain duration (about $45s$) some higher-order 3D instabilities invariably made their appearance. The most prominent of these was a cross-wave with wavelength 25 cm (half the width of the channel) which appeared when $f = 1.0s^{-1}$. Therefore most experiments were done at $f = 1.1s^{-1}$.

As is well known, if a wavemaker is started from rest, the wave front advances down the channel with the group velocity $c_g$. If the wavemaker is switched on suddenly at time $t = 0$, then according to linear theory the surface elevation $\zeta(x, t)$ at a horizontal distance $x$ from the wavemaker is given by

$$\zeta = \mathrm{i}BF(\tau)\mathrm{e}^{\mathrm{i}\sigma(t-\sigma x/g)} \tag{II.10}$$

approximately, where $B$ is a constant depending on the type of wavemaker, $\sigma$ is the radian frequency of the waves, $\tau$ is a dimensionless time:

$$\tau = \left(\frac{g}{2\pi x}\right)^{1/2}\left(t - \frac{2\sigma x}{g}\right) \tag{II.11}$$

which vanishes at the wave front $t = 2\sigma x/g$, and $F(\tau)$ describes the complex wave envelope:

$$F(\tau) = \frac{1}{2} + \frac{1}{1+\mathrm{i}}\int_0^\tau e^{\frac{1}{2}\mathrm{i}\pi\mu^2}d\mu; \tag{II.12}$$

see for example Miles (1962). The function $F(\tau)$ is related to the Fresnel integral (Abramowitz and Stegun, 1964). A sketch of the envelope $|F(\tau)|$ as a function of time is shown in Figure II.4.

The wave amplitude at first increases exponentially, reaches the value $\frac{1}{2}B$ at time $\tau = 0$ and then oscillates about its final value $B$ as $\tau \to \infty$. The first maximum in the amplitude is about 19 percent greater than the final amplitude. It has been shown experimentally (see Longuet-Higgins, 1974) that the effect of finite wave steepness is to increase the effective group-velocity so that the wave front arrives slightly sooner than predicted by the linear theory, and to increase the maximum wave amplitude considerably.

In the present experiments, in order to suppress the oscillations of the envelope, the wavemaker was started gradually from rest with a horizontal displacement

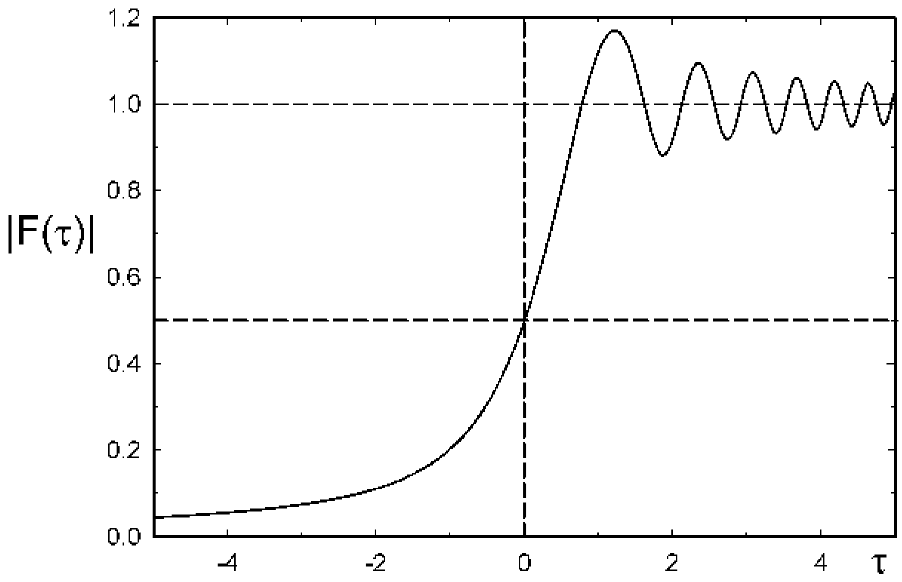

Figure II.4: Theoretical envelope of the surface elevation in the neighbourhood of a wave front, from equation (II.10).

given by

$$\zeta = \begin{Bmatrix} 0, & t < 0 \\ \\ C \tanh \lambda t \sin 2\pi f t, & t > 0 \end{Bmatrix} \tag{II.13}$$

where $C$ and $\lambda$ are constants. It was found convenient to take $\lambda = 0.1$. When $\lambda$ was much smaller, the wave train often did not approach its final amplitude ($e^{-2\lambda t}$ negligible) before the onset of the 3-dimensional instabilities mentioned above.

On the other hand, it was found useful to terminate the wave train after a certain number $N$ of wave cycles, by switching off the wavemaker suddenly. This produced a corresponding Fresnel pattern of the wave envelope at the *rear* of the wave train, including some waves which were steeper than the steady waves.

The input voltage to the wavemaker was governed by a certain gain factor, which we have denoted by $G$. Experiments were carried out over the range $1.6 \leq G \leq 2.6$; see Table II.1 for the corresponding wave parameters.

At each value of the gain $G$, four types of measurements were made. First, the surface elevation $\zeta$ was recorded at a point close to the wavemaker ($x$ = 2.30 m) but still far enough away that local effects were negligible, in general. The barrier at $B$ was not in place. Second, similar measurements were made at the point $B$, still without the barrier, so that the waves passed by as progressive waves. Thirdly the barrier was inserted, and the surface elevation was recorded at the same point $B$. In all three cases the wave gauge was situated on the center line of the channel. Simultaneously with the third recording, a video sequence of the waves near the barrier was taken as described above.

In order to prevent any horizontal displacement of the barrier it was constructed of 3/8in laminated plywood, strengthened by angle brackets, and was secured in place by a steel bar at the top, clamps above the water level and a firm tubular rubber seal at each side-wall. During the experiment no surface waves on the down-wave side of the barrier were detected.

A step-calibration of the wire wave gauges was carried out at the beginning and end of each series of experiments.

Table II.1: Range of experiments with $\lambda = 0.1, N = 40$

| G | $a_o$ (cm) | $a$ (cm) | $a\sigma^2/g$ | $ak$ | $a_s$ (cm) |
|---|---|---|---|---|---|
| 1.6 | 4.53 | 4.22 | 0.206 | 0.200 | 7.50 |
| 1.8 | 5.19 | 4.63 | 0.226 | 0.216 | 6.95 |
| 2.0 | 5.52 | 5.66 | 0.251 | 0.236 | 7.87 |
| 2.2 | 5.82 | 5.51 | 0.268 | 0.252 | 8.49 |
| 2.4 | 6.61 | 5.85 | 0.285 | 0.266 | 9.28 |
| 2.6 | 7.52 | 6.36 | 0.310 | 0.285 | 10.89 |

## II.6 Results

Figures II.5 and II.6 show the case $G = 1.6$. In Figure II.5 we see the wave amplitude at $x = 2.30$ m starting almost immediately to increase monotonically towards the value 4.5 cm, which is attained after about 25s. At $t = 38$s one can see the maximum $T$ of the Fresnel envelope created by the abrupt shut-off of the wavemaker after 40 cycles (36s).

Figure II.6a shows the same progressive wave train on arriving at $B$ ($x = 15.65$ m). The final amplitude $a$ is now only 4.2 cm, attained at about $t = 35$s. It remains constant until about $t = 42$s, after which it is affected by the Fresnel pattern from the wave cut-off. From equation (II.11) the width of the Fresnel pattern is proportional to $(2x/g)^{1/2}$ and so is increased over the width at $x = 2.30$ m by a factor 2.61. When $t > 30$s there are slight indications of a Benjamin-Feir instability, but these are small compared to the oscillations of the Fresnel envelope. The period of the envelope oscillations diminishes with distance from $T$. When $t = 43$s their period is less than two wave periods.

Figure II.6b shows the same situation as II.6a but with the barrier in place. Note the difference in vertical scales. The wave amplitude $a_s$ is roughly equal to $2a$ (see Table II.1) as one would expect on linear theory.

The corresponding three records when $G = 1.8$ were quite similar to those in

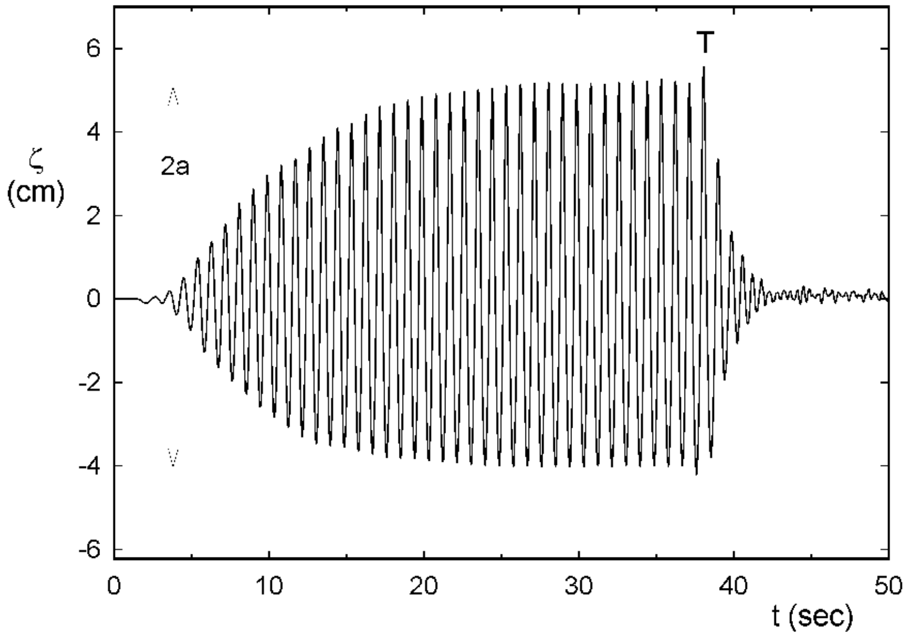

Figure II.5: Record of the surface elevation at $x$ = 2.30 m when $\lambda$ = 0.1 and $N$ = 40 (progressive wave: $G$ = 1.6).

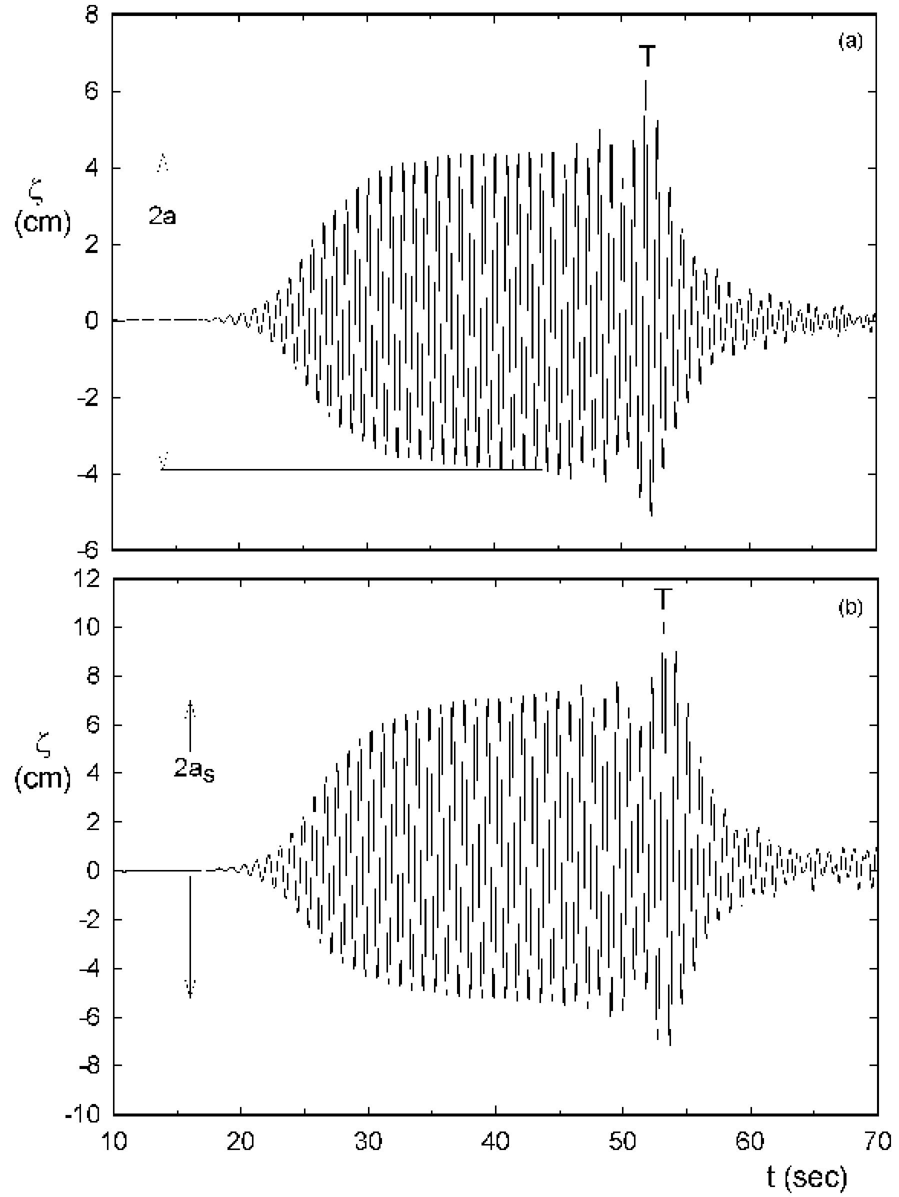

Figure II.6: Surface elevation at $x$ = 15.65 m when $G$ = 1.6, (a) with no barrier, and (b)with the barrier in place.

Figures II.5 and II.6, but with larger amplitudes; see Table II.1. However when $G$ = 2.0 some qualitatively new features appeared. Figures II.7a and II.7b show the records taken at the point $B$ ($x$ = 15.65 m) without the barrier and with the barrier in place, respectively.

Figure II.7a shows the usual Fresnel envelope for a progressive wave, with the maximum at $T$. Before $t$ = 40s there is a slight modulation of the envelope due either to a Benjamin-Feir instability or to some 3-dimensionality in the motion. Figure II.7b, however, taken with the barrier in place, shows that between $t$ = 40s and $t$ = 50s there is apparently a new instability in which every third wave, marked with the symbol $S_i$, ($i$ = 1 to 4) is higher than its two neighbours.

This is confirmed by Figures II.8a and II.8b, taken when $G$ = 2.2. In Figure II.8b, which shows the surface elevation in the reflected wave, the three-fold pattern now extends as far as from $t$ = 35s to $t$ = 50s. It appears to have overwhelmed the Fresnel pattern even as far as the maximum $T$.

Figure II.9b, corresponding to $G$ = 2.4, shows the same pattern extending as far back as $t$ = 30s, but by $t$ = 45s the waves have become chaotic and the Fresnel pattern is quite ragged. A similar phenomenon is apparent in Figure II.10b, corresponding to $G$ = 2.6. Here the pattern begins and breaks down even earlier.

An examination of the photographic record, see Figure II.11 for the case $G$ = 2.4, reveals that the highest peaks in each triplet are always sharp-pointed. The lower peaks are either round-crested on flat-topped or sometimes have profiles that are intermediate between flat-topped and sharp-crested; see Figure II.12. After the crest $S_5$, at $t$ = 40s, the motion becomes markedly three-dimensional, which contributes to the chaotic appearance of the record of surface elevation.

## II.7 Discussion and conclusions

A rough measure of the amplitude of the instability noted in Figures II.7b to II.10b is the difference $\Delta\zeta$ in crest height between the highest and lowest waves of each

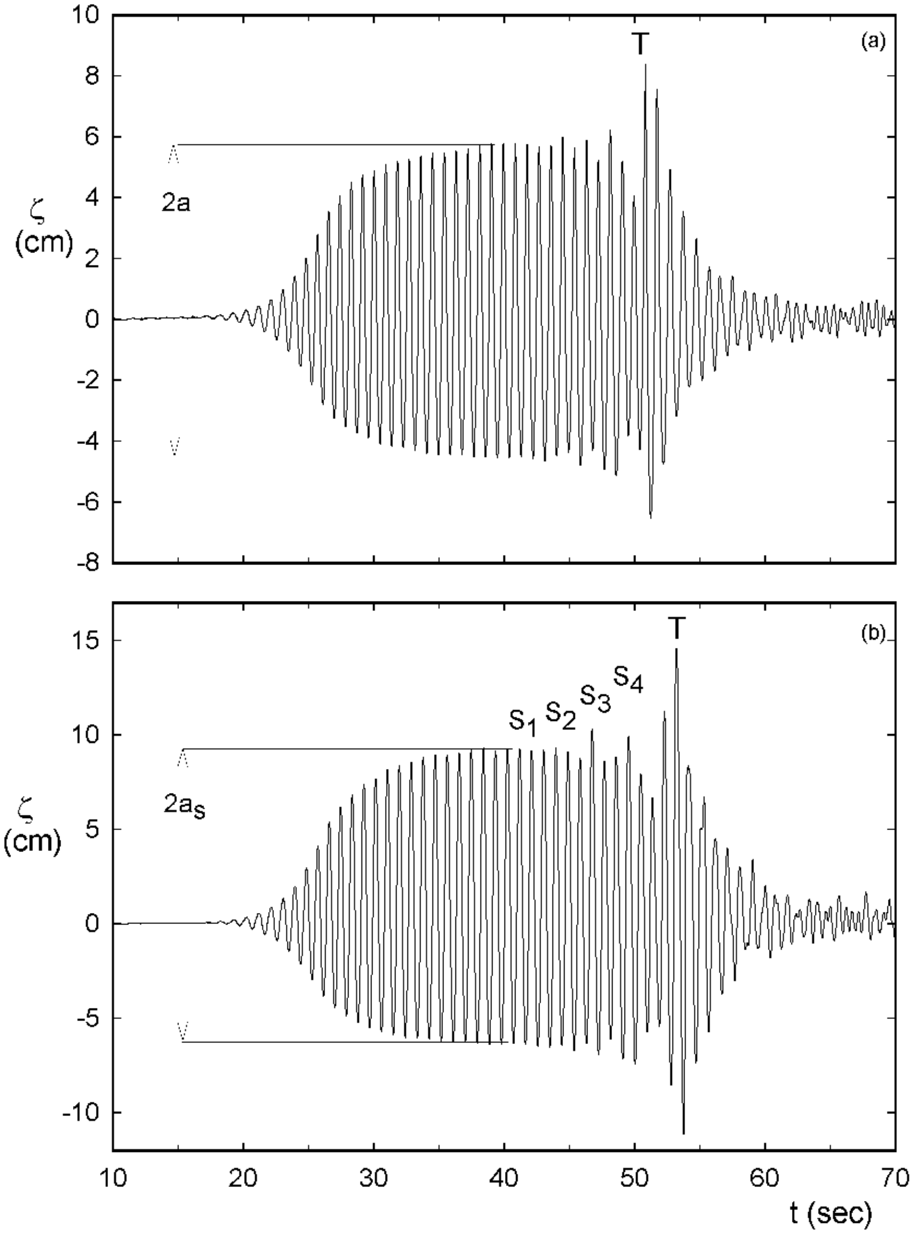

Figure II.7: Surface elevation at $x$ = 15.65 m when $G$ = 2.0 (a) with no barrier (b) with the barrier in place.

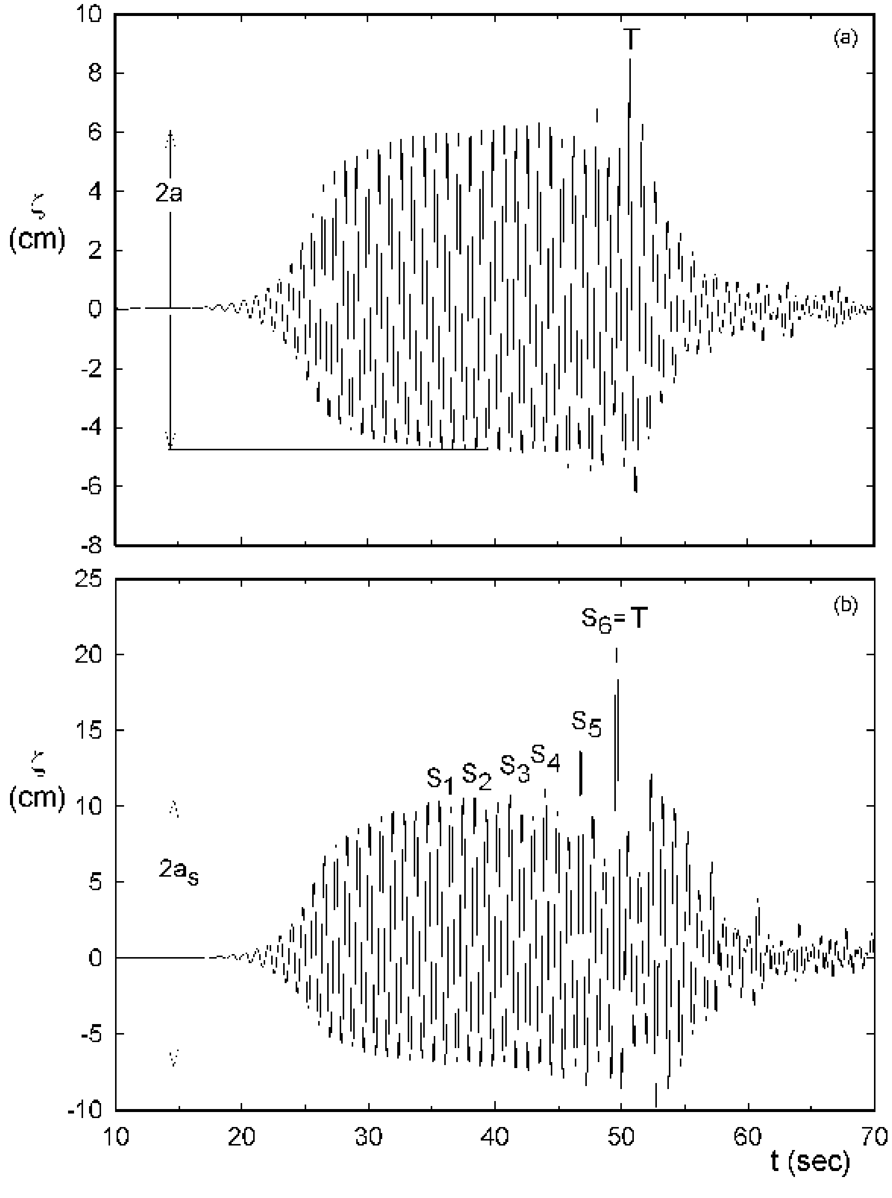

Figure II.8: Surface elevation at $x$ = 15.65 m when $G$ = 2.2 (a) with no barrier (b) with the barrier in place.

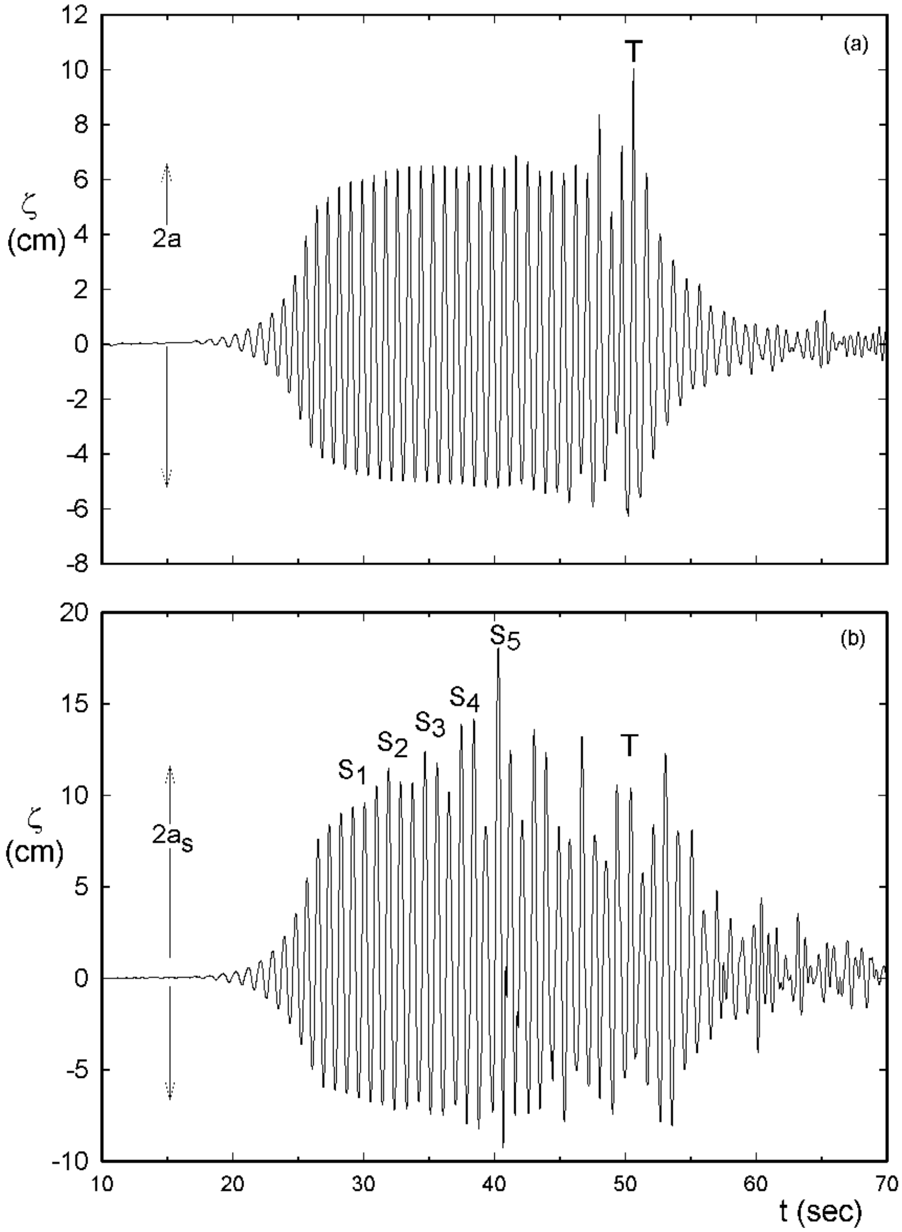

Figure II.9: Surface elevation at $x$ = 15.65 m when $G$ = 2.4 (a) with no barrier (b) with the barrier in place.

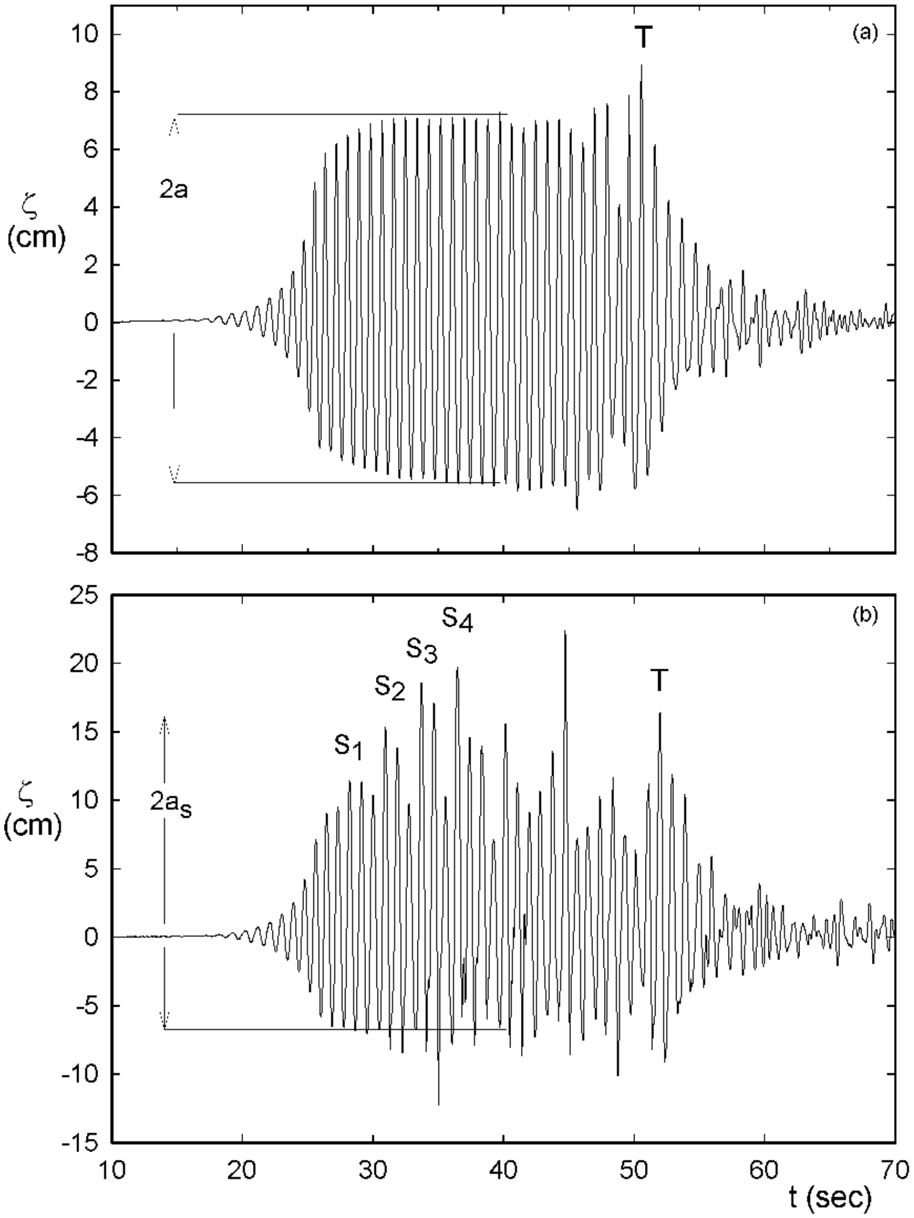

Figure II.10: Surface elevation at $x$ = 15.65 m when $G$ = 2.6 (a) with no barrier (b) with the barrier in place.

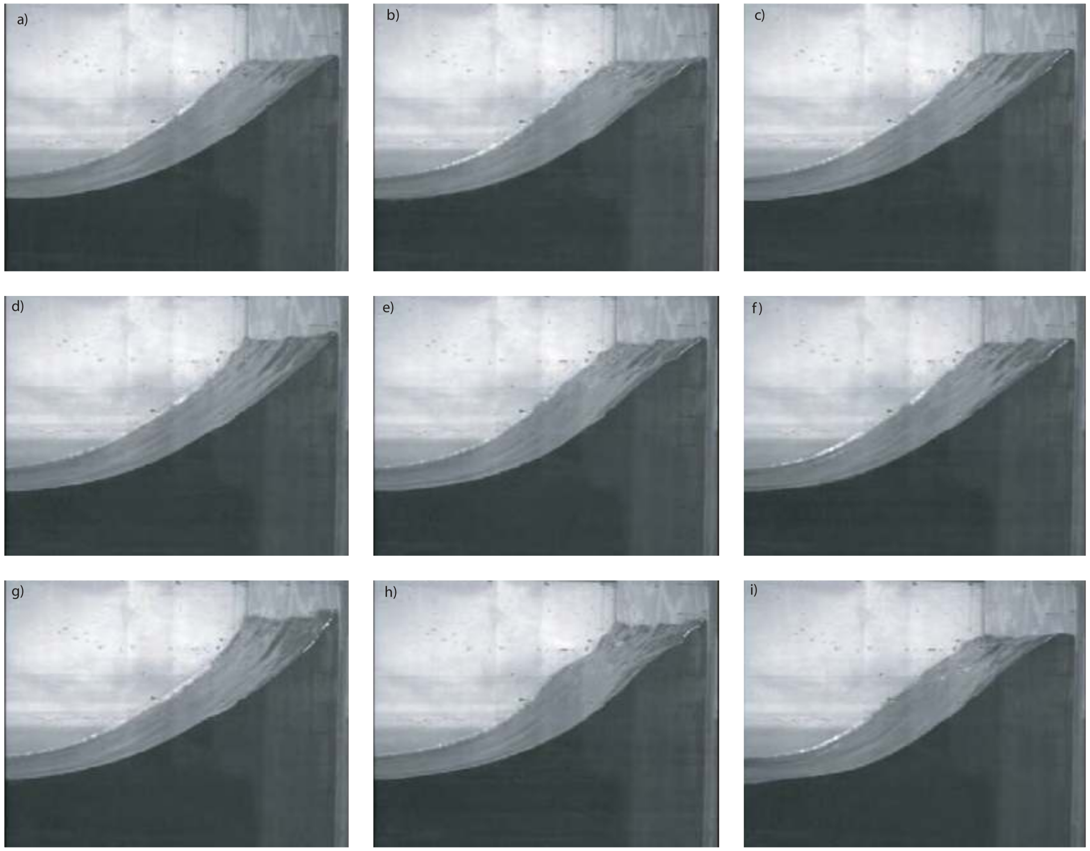

Figure II.11: A sequence of frames from the video corresponding to Figure II.9b ($G = 2.4$), showing consecutive wave crests between $t = 28$s and 42s. The video was taken at 30 frames/sec, and the timing of each frame is as close as possible to a maximum of the surface elevation shown in Figure II.9b, that is within 1/60s. Each frame in the left-hand column above corresponds to one of the maxima marked $S_i$ in Figure II.9b.

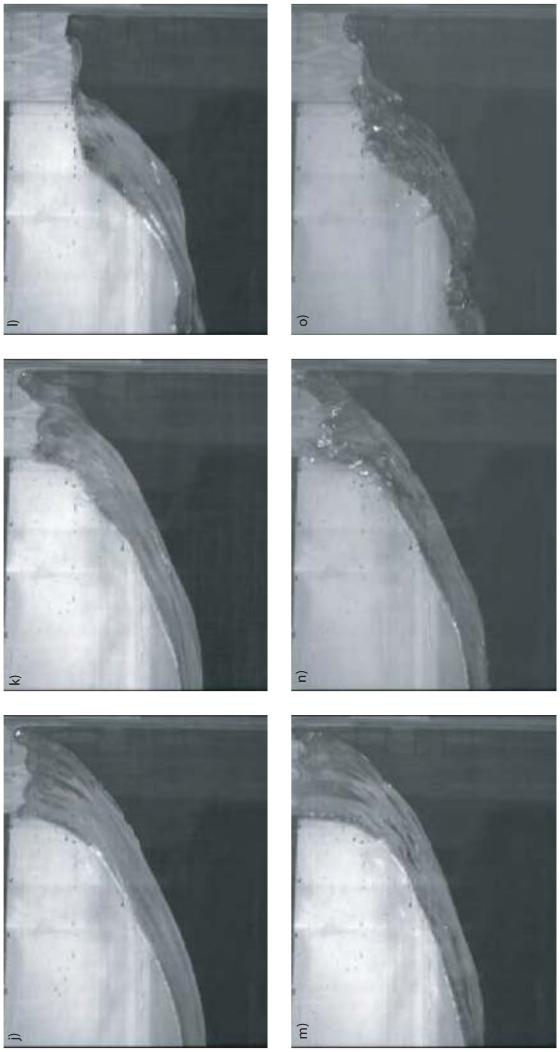

Figure II.11 continued. See caption on previous page.

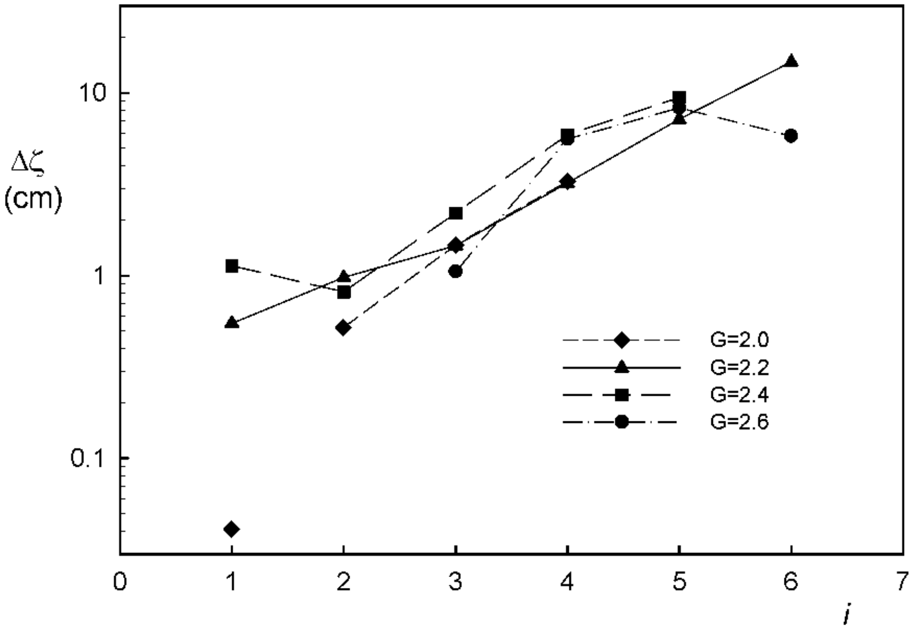

Figure II.12: Growth of the triple-period instability, as measured by the difference $\Delta\zeta$ in crest-elevation between the highest and lowest waves of a triplet.

triplet. In Figure II.12, $\Delta\zeta$ has been plotted against the suffix $i$ in $S_i$ on a log-linear scale, for each value of $G$, except that when $G = 2.6$, $i$ has been increased by 2 to bring the plots closer together. (This does not of course affect the proportional rate of increase of $\Delta\zeta$.) It will be seen that in every case except one, namely $i = 1$ and $G = 2.0$, the plots lie close to the same straight line. This indicates an increase in $\Delta\zeta$ by a factor of about 2.2 for every 3 wave cycles, that is an increase of 1.3 per wave cycle. The exceptional plotted point ($x$) corresponds to a very small value of $\Delta\zeta$, lying within the noise-level of the experiment.

Thus we have detected a subharmonic instability which tends to occur at values of $G$ greater than about 2.0, that is to say incident wave steepnesses $ak \geq 0.236$ (see Table II.1). The observed rate of growth is about 1.3 per wave cycle, practically independent of the incident wave amplitude.

The above instability is probably related dynamically to the “period tripling" phenomenon observed by Jiang et al. (1998) in forced standing waves. There are some differences, however.

(1) In Jiang et al. (1998) standing waves were forced subharmonically by oscillating the wave tank vertically at a frequency twice that of the resulting surface waves. Such a method of excitation is of course unlikely to be found in nature except, for example, in an earthquake at sea. In our experiments the “quasi-standing" waves were the result of the reflection of free progressive waves from a vertical cliff or wall.

(2) In the experiments of Jiang et al. (1998) a *steady* state was achieved by balancing the input of wave energy from the vertical forcing against the loss of energy due to wave breaking. In our experiments there was no energy input due to vertical motion of the bottom, the loss of energy due to wave breaking was negligible, and the instability grew in time.

(3) In their experiments the observed sequence of wave crests was: sharp-crested → flat-topped → rounded → sharp-crested, and so on. In our experiments a sharp-crested wave was often *preceded* by a flat-topped wave, though not invariably. Other types of crest-form were also observed, as illustrated in Figure II.10.

Note that some instabilities of periodic standing waves that are subharmonic in space were found analytically by Mercer and Roberts (1992). Those described here, however, were subharmonic in time. Recording of the spacial behaviour of the instability as a function of the horizontal coordinate $x$ would have involved much more elaborate instrumentation, particularly since the position of the wave crests, other than at the wall, appeared to be slightly variable.

In the profiles shown in Figure II.11 the effects of both viscosity and surface tension are apparently negligible. Viscous effects at the vertical barrier would tend to be reduced by the oscillatory nature of the boundary layer. Although surface tension may affect the wave profiles at smaller scales, at larger scales one can expect Froude scaling to apply.

# Appendix. Determination of the steepness parameter *ak*

Given the crest-to-trough wave height $2a$ and the radian frequency $\sigma = 2\pi/T$, where $T$ is the wave period, our problem is to find the wave steepness $ak$, where $k$ is the wavenumber.

It is assumed that the waves are effectively in deep water, that is to say if $h$ is the still-water depth, then $e^{-2kh}$ is negligible. Now in Table II.2 of Longuet-Higgins (1975), the phase-speed $c$ and the quantity

$$a/\pi = 2a/L = 2ak \tag{II.14}$$

are both given as functions of a monotonic parameter $\omega$ which runs from 0 to 1 as the wave passes from zero steepness to its limiting configuration with a sharp-angled crest. See also Figure 1 of that paper, where $ak$ and $(c^2 - 1)$ are both plotted against $\omega$. From the tabulated entries we may thus obtain the first three columns of Table II.2 below. Hence for each value of $ak$ we find the corresponding value of

$$a\sigma^2/g = (c^2/g)\, ak. \tag{II.15}$$

The values are plotted in Figure II.13. In the experiments, $\sigma^2/g$ is a known constant. Hence for every value of $a$ we can calculate $a\sigma^2/g$ and by interpolation in Figure II.13 find the corresponding value of $ak$.

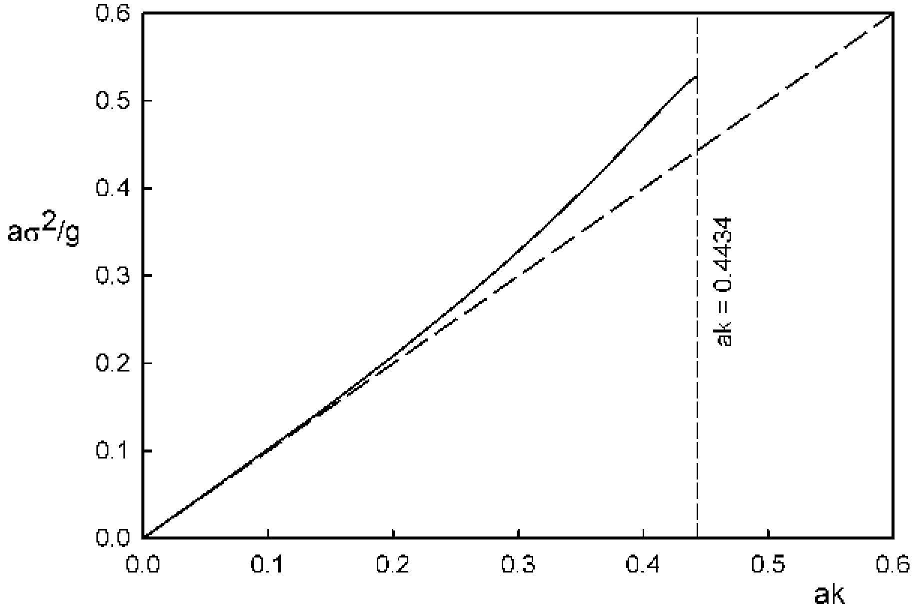

Figure II.13: Graph of $a\sigma^2/g$ against $ak$ for nonlinear progressive gravity waves in deep water.

*Acknowledgements* M.S.L.H. was supported by the Office of Naval Research under Contract N00014-00-1-0248, and D.A.D. by the National Science Foundation under Grant OCE-98-12182 to W.K. Melville. The authors thank C. Coughran, J. Lyons and D. Aglietti for technical assistance. An account of the experiments was presented at the I.N.I. Program on Surface Water Waves, Cambridge, England, 13-31 August 2001, and at the I.M.A. Conference on Wind-over-Waves, Churchill College, Cambridge, 3-5 September 2001 by M.S.L.H.. D.A.D presented results of these experiments at the 54th APS Division of Fluid Dynamics Annual Meeting, San Diego, California, 18-20 November, 2001.

This chapter, in full, is a reprint of the material as it appears in "On steep gravity waves meeting a vertical wall: a triple instability." Longuet-Higgins, M.S. and Drazen, D.A., *Journal of Fluid Mechanics*, **466**, 305–318, 2002. The dissertation author contributed to this work by collecting and handling the experimental data. Michael S. Longuet-Higgins provided the theory, assisted and directed the experimental work, and wrote the paper.

Table II.2: Corresponding values of $ak$ and $a\sigma^2/g$ for deep-water gravity waves of finite amplitude

| $\omega$ | $ak$ | $(c^2 - 1)$ | $a\sigma^2/g$ |
|---|---|---|---|
| 0.00 | .00000 | .00000 | .00000 |
| .10 | .14222 | .02042 | .14512 |
| .20 | .20216 | .04173 | .21060 |
| .30 | .24877 | .06385 | .26465 |
| .40 | .28843 | .08674 | .31349 |
| .50 | .32346 | .11020 | .35911 |
| .55 | .33958 | .12203 | .38102 |
| .60 | .35488 | .13384 | .40238 |
| .65 | .36936 | .14552 | .42311 |
| .70 | .38303 | .15687 | .44312 |
| .75 | .39582 | .16767 | .46219 |
| .80 | .40765 | .17757 | .48000 |
| .85 | .41839 | .18601 | .49621 |
| .90 | .42782 | .19211 | .51001 |
| .95 | .43578 | .19454 | .52056 |
| 1.00 | .4432 | .1931 | .5288 |

# Chapter III

# Measurement of the normalized dissipation rate from unsteady breaking

## III.1 Introduction

The dynamics of breaking waves play a significant role in the air-sea boundary layer. The breaking process transfers momentum to the upper ocean from the surface waves and in turn generates currents. In addition the transfer of heat and gases is enhanced through the breaking process. The widespread distribution and ubiquitous nature of breaking stresses the need to understand the role breaking plays in air-sea interactions, (Duncan, 2001; Melville, 1996; Banner and Peregrine, 1993). This enhanced knowledge of breaking would help to further improve models of the atmosphere-ocean boundary layer.

Modeling of the evolution of ocean surface waves is usually done through use of a radiation transfer equation. In this model the evolution of the action spectral density is balanced by a series of forcing terms (Komen, Hasselmann, and Hasselmann, 1984; Phillips, 1985). The action spectral density is $N(\vec{k}) = g\psi(\vec{k})/\sigma$, where $\psi(\vec{k})$ is the energy spectral density, $\vec{k}$ is the wavenumber, and $\sigma$ is the intrinsic frequency. The evolution is described by

$$\frac{\partial N}{\partial t} + (\vec{c_g} + \vec{U}) \cdot \nabla N = S_{nl} + S_{in} + S_{diss} \tag{III.1}$$

where $S_{nl}$, $S_{in}$, and $S_{diss}$ are the source terms for non-linear interactions, wind input, and dissipation. Of these terms the dissipation is the least understood and is assumed to be dominated by wave breaking processes.

Breaking is intermittent in both space and time, which makes detailed field measurements difficult. This is compounded by the fact that the environments in which large-scale breaking occurs are not hospitable nor conducive to making detailed measurements. Laboratory measurements of wave breaking permit detailed measurements of dynamical quantities as well as controlled initial conditions. The laboratory is an essential setting to further understand the dynamics of breaking.

Duncan (1981) studied quasi-steady breaking waves in the laboratory generated by a submerged hydrofoil. Through analysis of the integrated horizontal and vertical momentum balances he arrived at the following scaling for the dissipation rate,

$$\epsilon_l = 0.009 \frac{\rho c^5}{g \sin\theta}. \tag{III.2}$$

Here $\epsilon_l$ is the dissipation per unit length of crest, $\rho$ the density of water, $g$ the gravitational acceleration, $c$ the phase speed of the wave, and $\theta$ the angle of inclination above horizontal of the breaking region, see figure III.1a. For the range of $\theta$ used, $\epsilon = b\rho c^5/g$ with the breaking parameter, $b = 0.044 \pm 0.008$. Subsequent work by Duncan (1983) to further resolve the drag on the hydrofoil show a marked change in $\theta$ with varying hydrofoil depth. The results from this later work implied a new range for $b = 0.032 - 0.075$. A summary of various estimates of the breaking parameter, $b$, found in the literature is given in table III.1.

Phillips (1985) used the results of Duncan (1981) in a statistical description of breaking based on the distribution of breaking fronts per unit area of ocean surface. He then defined the average rate of energy loss for breaking waves with speeds in the range $(\mathbf{c}, \mathbf{c} + \mathrm{d}\mathbf{c})$ to be

$$\epsilon(\mathbf{c})\, \mathrm{d}\mathbf{c} = b\rho g^{-1} c^5 \Lambda(\mathbf{c})\, \mathrm{d}\mathbf{c}. \tag{III.3}$$

Here $\Lambda(\mathbf{c})$ is a distribution of breaking fronts on the ocean surface where $\Lambda(\mathbf{c})d\mathbf{c}$ is the average total length of breaking fronts per unit surface area within the range $(\mathbf{c}, \mathbf{c} + d\mathbf{c})$. The breaking parameter, $b$, was assumed to be constant by Phillips (1985) using a value of $b = 0.06$ from Duncan (1981).

Measurements of the loss of momentum and energy fluxes from surface waves due to unsteady breaking were performed by Rapp and Melville (1990). It was found that up to 30% of the initial energy of a wave packet could be lost through breaking of an individual event. Rapp and Melville (1990) extended these measurements and found that approximately 90% of the energy loss occurred within the first four wave periods after breaking. Analysis of the growth of the turbulent patch generated by breaking showed that the depth of mixing was on the order of the breaking wave height. Subsequent work done by Lamarre and Melville (1991) showed that up to 50% of the energy lost was due to work done in entraining air against buoyancy effects. The large levels of energy lost along with high void fractions suggest that the post-breaking region is well-mixed and highly dissipative.

Loewen and Melville (1991) performed measurements of the acoustics and microwave scattering of breaking waves in the laboratory. It was found that the amount of acoustic energy radiated by the breaking wave scaled with the dissipation of energy during the breaking process. While these experiments were not designed to measure dissipation outright, Melville (1994) undertook a re-analysis of the data to find that the non-dimensional dissipation rate $b$ varied approximately linearly with the slope, $b = [4 - 12] \cdot 10^{-3}$, where the slope is defined as the sum of all of the components that make up the wave packet, $S = \sum a_n k_n$. Using an inertial estimate of the dissipation rate, $\epsilon_m \approx u^3/l$, with $u$ and $l$ representative velocity and length scales of the flow, Melville obtained $b = [3 - 16] \cdot 10^{-3}$ based on scaling arguments from Rapp and Melville (1990). The correlation between these two measures of $b$ is quite good considering that the argument used is based on an order of magnitude estimate.

Deane and Stokes (2002) measured bubble size distributions within a breaking wave in the laboratory using seawater. To quantify the bubble size distribution high-

Table III.1: Estimates of $b$ from the literature. For a given estimate, pertinent information about its measurement is given. All quasi-steady and unsteady assumptions refer to laboratory measurements of $b$.

| Experiments | $b$ | Measurement Details |
|---|---|---|
| Duncan (1981) | $[4.4 \pm 0.8] \cdot 10^{-2}$ | Quasi-steady breaking |
| Duncan (1983) | $[3.2, 7.5] \cdot 10^{-2}$ | Quasi-steady breaking |
| Melville (1994) | $[4, 12] \cdot 10^{-3}$ | Unsteady breaking |
| Melville (1994) | $[3, 16] \cdot 10^{-3}$ | Inferred from $\epsilon \approx u^3/l$ |
| Phillips et al. (2001) | $[7, 10] \cdot 10^{-4}$ | Remote Field measurements |
| Deane and Stokes (2002) | $8.6 \cdot 10^{-3}$ | Unsteady breaking |
| Melville, Veron, and White (2002) | $7 \cdot 10^{-3}$ | Unsteady breaking |

speed video imagery and hydrophone measurements were used. The Weber number, $\mathrm{We} = (\rho/\gamma)u^2 d$, is a measure of the ratio of the pressure forces to the surface tension on a bubble, where $\rho$ is the fluid density, $\gamma$ is the surface tension, $u$ a turbulent velocity scale, and $d$ the bubble diameter. Above a critical value of We a bubble will undergo breakup. Assuming the turbulent velocity field to be within an inertial subrange the authors found that $a_H \approx \epsilon^{-2/5}$, where $a_H$ is the Hinze scale, the smallest size of bubble undergoing fragmentation by the turbulence. Based on their results, they computed $\epsilon_l = 12.46$ kg m s$^{-3}$, yielding $b = 8.6 \cdot 10^{-3}$. Deane and Stokes (2002) state that the breaking event considered was a multiple breaking event, which is consistent with the range of $b$ found for multiple breaking events in Melville (1994).

Through analysis of radar measurements of wind generated ocean waves Phillips et al. (2001) inferred an estimate of $b = [7 - 13] \cdot 10^{-4}$. The indirect method of measurement made it difficult at times to distinguish individual breaking events, especially when they were being overtaken by faster events. This could account for the lower levels of $b$ seen relative to those in the laboratory. The upper limits of these estimates of $b$ however are close to the lower range of Melville (1994) and would be consistent with weaker breaking events.

Melville and Matusov (2002) used airborne video imagery of the ocean surface to measure distributions of breaking waves. Measurements of $\Lambda(\mathbf{c})$ were made and its various moments were calculated. In order to calculate the momentum flux and energy dissipation, $b$ was assumed to be constant, $b = 8.5 \cdot 10^{-3}$. This estimate was obtained using the results of Melville (1994). The various moments normalized by $U_{10}^3$ collapse well at smaller values of $c$, where $U_{10}$ is the mean wind speed at 10 m above the ocean surface. The techniques employed by Melville and Matusov (2002) allow for large statistical datasets from which kinematic details of breaking can be inferred. The breaking parameter, $b$ provides the link between the dynamics and the kinematics of breaking, which is necessary in order to estimate momentum fluxes and dissipation rates in the field.

Sullivan, McWilliams, and Melville (2004) developed a stochastic model of breaking waves on the ocean surface and evaluated the model through the use of direct numerical simulation, DNS. The model was based on the Navier-Stokes equations with an additional forcing term, $\mathbf{A}$, that represents the effects of breaking. The breaking was randomly added to the surface of the domain and had a specified whitecap coverage. The forcing $\mathbf{A}$ was modeled on the laboratory results of Rapp and Melville (1990) and Melville et al. (2002), as well as the field measurements of Melville and Matusov (2002). Sullivan et al. (2004) found that the model agreed well with experimental data from a single unsteady breaking wave (Melville et al., 2002). Additionally they found that with a small fraction of active breaking there was significant turbulent mixing, transport of vertical momentum, and that the impact of a single breaking event was long-lived as compared to the duration of active breaking.

We see that the estimate of the breaking parameter, $b$, varies significantly when comparing results from unsteady and quasi-steady breaking in the laboratory to field measurements. The quasi-steady measurements conducted by Duncan (1981, 1983) were on forced breaking events generated by a towed hydrofoil. The forced nature of the breaking could account for the larger values of $b$ as compared to those from unsteady breaking. Much of the variability of $b$ in unsteady breaking in the laboratory is due to wave slope effects which are difficult to directly measure in the field. The ability to quantify the dissipation rate in terms of measurable pre-breaking variables is necessary to relate the kinematics of breaking to the subsequent dynamics. In this chapter we present laboratory measurements of $b$ for unsteady breaking waves that range from gently spilling to plunging.

In section III.2 we present a dimensional analysis of the dissipation rate and propose a model of $\epsilon_l$ for plunging breaking waves. Section III.3 describes the experimental setup. Section III.4 describes the measurement of the dissipation rate, section III.5 presents the results, while section III.6 discusses these results in terms of the proposed model and implications for field measurements.

## III.2 Scaling of the dissipation rate

### III.2.A Dimensional analysis

We consider a breaking event which is two-dimensional in the mean. Let $(x_b, t_b)$ be the location of the breaking in space and time, with $x$ the downstream distance and $t$ time. We can express the post-breaking velocity field as

$$\vec{u} = \vec{u}(\vec{x}, t; \rho_w, \rho_a, g, \Gamma, a, k, \delta k, \mu_w, \mu_a) \tag{III.4}$$

where $\rho_w$ is the density of water, $\rho_a$ the density of air, $g$ gravity, $\Gamma$ surface tension, $a$ the characteristic wave amplitude, $k$ the characteristic wavenumber, and $\mu_w, \mu_a$ the viscosity of water and air respectively. Through dimensional analysis we can arrive at the following relationship

$$\frac{\vec{u}}{c} = f_{n1}\left(\vec{x}k, \frac{t}{T}; Bo, \mathrm{Re}_w, \mathrm{Re}_a, ak, \frac{\delta k}{k}, \frac{\rho_a}{\rho_w}\right) \tag{III.5}$$

where $c = \sqrt{g/k}$ is the characteristic phase speed and $T = 2\pi/\sqrt{gk}$ is the characteristic period of linear deep water gravity waves, $\mathrm{Re}_\mathrm{w} = \frac{2\pi c \rho_w}{k\mu_w}$, $\mathrm{Re}_\mathrm{w} = \frac{2\pi c \rho_a}{k\mu_a}$ is the Reynolds number for the water and air respectively, and $Bo = \frac{\rho g}{\Gamma k^2}$ is the Bond number. Using the dimensional arguments from above, the loss of energy from the wave field per unit wave crest length per unit time through breaking, $\epsilon_l$ can be written as

$$\frac{\epsilon_l}{\rho c^5/g} = f_{n2}\left(\frac{t}{T}; Bo, \mathrm{Re}_w, ak, \frac{\delta k}{k}, \frac{\rho_a}{\rho_w}\right) \tag{III.6}$$

The wave dissipation defined here does not represent the rate at which mechanical energy is lost to heat, but rather it is the energy lost from the wave field.

We assume now that the flow becomes independent of the Reynolds number for sufficiently large values of $Re$. For the flow we consider here, typical Reynolds numbers for water and air are on the order of $10^5 - 10^6$ and $10^4 - 10^5$ respectively. If we also assume that the air-water density ratio and Bond number remains constant then (III.6) should only be dependent on $ak$ and $\delta k/k$. Thus we have,

$$\frac{\vec{u}}{c} = f_{n1}\left(\vec{x}k, \frac{t}{T}; ak, \frac{\delta k}{k}\right) \tag{III.7}$$

$$\frac{\epsilon_l}{\rho_w c^5/g} = f_{n2}\left(\frac{t}{T}; ak, \frac{\delta k}{k}\right) \tag{III.8}$$

### III.2.B Scaling for quasi-steady and unsteady breaking

The scaling of the dissipation rate can come from a more physically based argument based on both Duncan (1981) and Melville (1994). Duncan created quasi-steady breaking waves in the laboratory using a towed hydrofoil (figure III.1a). The cross-sectional area of the breaking region can be scaled as $\lambda^2 = (c^2/g)^2$, where $\lambda$ is the wavelength of the breaking wave. Duncan then used the time and spatially averaged horizontal and vertical momentum equations to arrive a scaling for $\tau$, the shear stress at the bottom boundary of the breaking region, given by

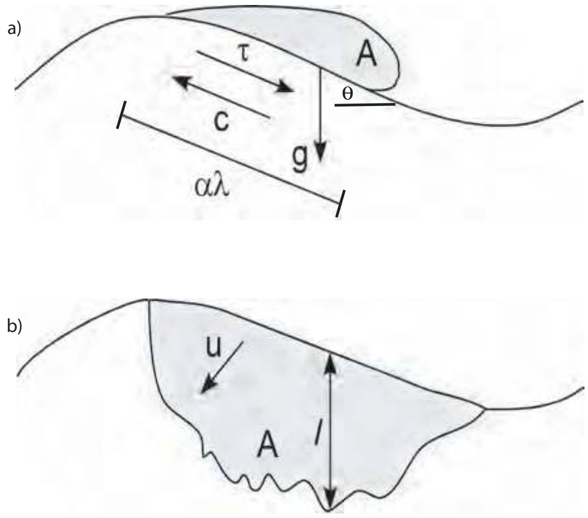

Figure III.1: Schematic describing the layout used for physically based arguments for scaling the dissipation rate. a) is based on arguments made by Duncan (1981), with A being the area enclosed by the breaker, $\alpha\lambda$ the fractional extent of the breaking, $g$ acceleration due to gravity, $\tau$ the stress caused by the breaking, $\theta$ the angle of inclination above horizontal, and $c$ the speed of the breaking wave. b) is based on arguments made by Melville (1994), with $A$ being the area enclosed by breaking, $u$ a representative velocity scale, and $l$ the outer length scale.

$$\tau \propto \left(\frac{c^2}{g}\right)^2 \frac{g}{\lambda} = \frac{c^4}{g\lambda} \tag{III.9}$$

This expression shows that the forces generated by the shear stress balance the weight of the breaking region. The force per unit length exerted by the breaker then on the underlying fluid is simply $\tau\lambda$ and we can now scale the dissipation per unit length per unit mass as

$$\epsilon_l = \tau\lambda C \propto \frac{c^5}{g} \tag{III.10}$$

Melville (1994) arrived at a similar scaling based on the inertial estimate of the dissipation, $\epsilon_m \approx u^3/l$, using unsteady breaking as a model. Use of the wavelength and phase speed to scale the length and velocity we get

$$\epsilon_l \approx \rho A \epsilon_m \propto \rho\lambda^2 \frac{c^3}{\lambda} \propto \rho c g \lambda^2 \propto \frac{\rho c^5}{g} \tag{III.11}$$

here $\epsilon_l$ refers to the dissipation rate per unit length per unit mass.

Both of these results are consistent with the dimensional analysis and this agreement implies that the basic scaling should be independent of the details of the processes which generate the breaking. Rapp and Melville (1990); Loewen and Melville (1991) used dispersive focusing to generate a single breaking wave group. Each group consists of $N$ waves, with the input slope of the wave given by $S = \sum a_n k_n$, with $a_n, k_n$ the amplitude and wavenumber of the nth component. The packet has a spectral bandwidth, $\delta k/k$, and a non-dimensional breaking location, $k_c x_b$. (Rapp and Melville, 1990; Loewen and Melville, 1991) have shown that the the dominant dependence of the energy loss is on the input wave slope, and not on the bandwidth of the envelope, or the non-dimensional distance to breaking.

### III.2.C Model of the dissipation rate for plunging waves

It has been shown that the dissipation rate is strongly dependent on the wave slope. Melville (1994) showed that use of the inertial estimate of dissipation, $\epsilon \approx u^3/l$,

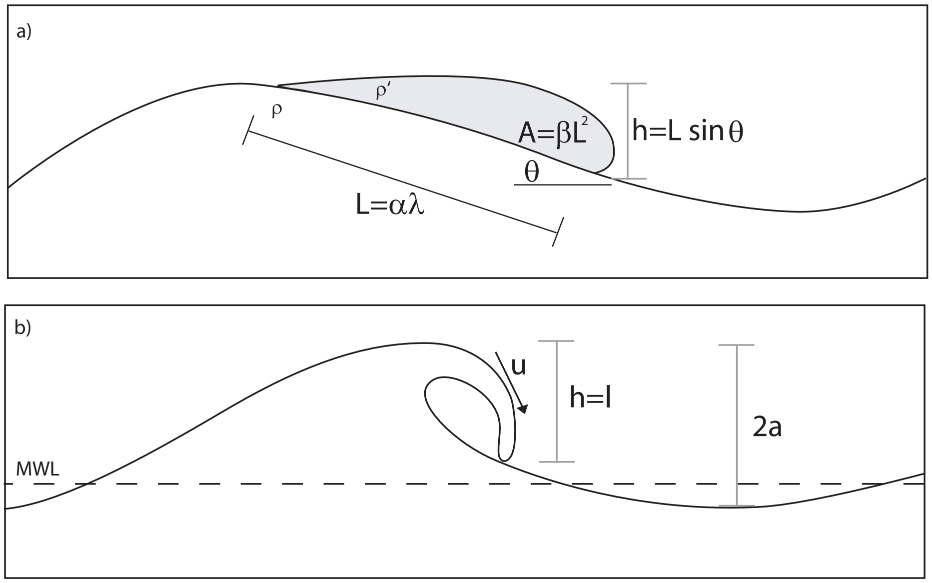

Figure III.2: A definition sketch for a) a spilling wave, and b) a plunging wave. The dashed line in b) is the mean water level. $\rho$ is the density of the underlying fluid and $\rho'$ the density of the fluid within the breaking region. $h$ is the height of the breaking region, $2a$ is the distance from the crest to the trough, and $u$ is the vertical speed of the falling wave tip. In a) $L$ is the length of the breaking region, and $\theta$ is the angle of the breaking region relative to the horizontal.

yields estimates of the breaking parameter $b$ which agree with those based on the laboratory measurements of Loewen and Melville (1991).

An inertial model of the dissipation rate is sought with the local wave height $h$ and velocity at breaking as the length and velocity scales of the flow. Using a plunging breaking wave as our model we assume that the toe of the breaking wave undergoes freefall during breaking and $h$ will be defined as the vertical distance that the toe falls (figure III.2). Figure III.3 shows the trajectory of the toe of a plunging breaking wave as measured by a high speed camera. The elevation is the height above the impact point and the time origin is when the toe of the breaking wave first appears. The solid line is the ballistic path under gravity, $\frac{1}{2}g(t-t_0)^2$, where $t_0$ is the time of maximum elevation. These results show that to a good approximation the toe is in freefall. The vertical velocity of the toe at impact on the surface below is

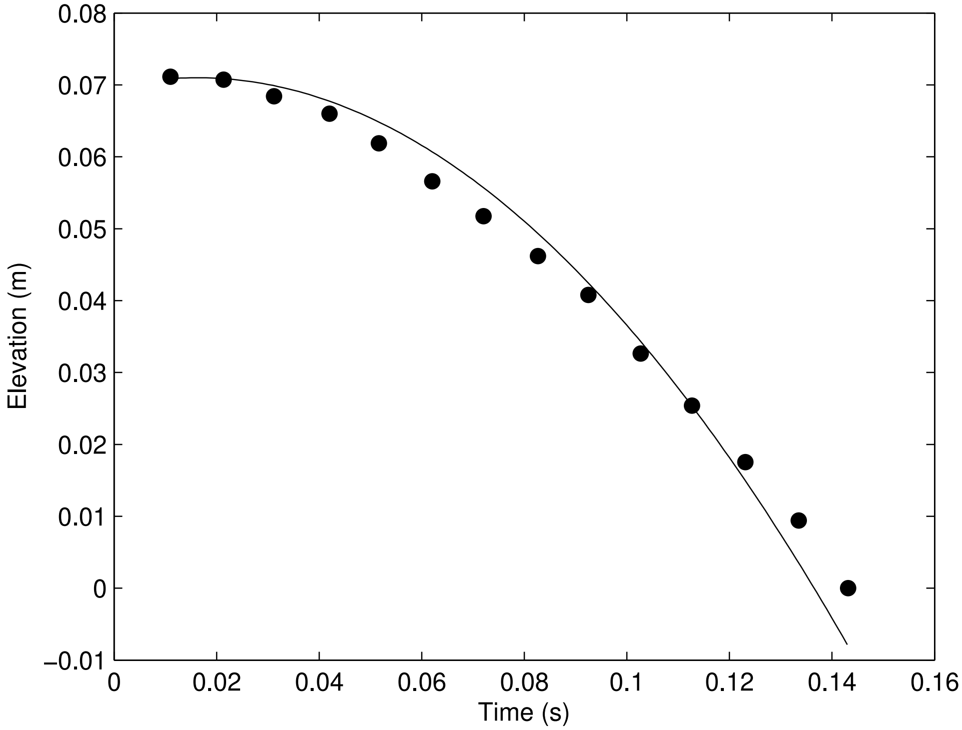

Figure III.3: Location of the toe of a plunging breaking wave with the ballistic trajectory (solid line) as predicted by projectile motion, $\frac{g}{2}(t - t_0)^2$ where $t_0$ is the point of maximum elevation. Time equal to zero is the time of initial toe formation. Elevation is the height above the point where the toe impacts the water surface. The distance between the first and last points shown here is $h$ (defined in figure III.2).

$$u = \sqrt{2gh}, \tag{III.12}$$

and $h$ is the length scale of the volume of fluid that will collapse under gravity into a turbulent cloud. For this cloud of turbulence, dissipation per unit mass should scale with

$$\epsilon_m = O\left(\frac{u^3}{h}\right) \propto (2g)^{3/2} h^{1/2}, \tag{III.13}$$

and the dissipation per unit length is simply

$$\epsilon_l \propto \rho A \epsilon_m \propto \rho h^2 (2g)^{3/2} h^{1/2} \tag{III.14}$$

$$\propto \rho \pi (2g)^{3/2} h^{5/2} \tag{III.15}$$

assuming that the area of the cloud of turbulence scales with the height, $A \propto h^2$.

Expressing (III.15) as

$$\epsilon_l = \frac{b \rho c^5}{g} \tag{III.16}$$

gives

$$b = \chi 2^{3/2} (hk)^{\frac{5}{2}} \tag{III.17}$$

where $\chi$ is a constant of order unity. Thus we can see that this model predicts that $b$ should have a dependence on the slope parameter, $hk$ which we call the local slope.

The experiments described here were conducted to test (III.17). Additional experiments were performed in order to directly measure the post-breaking velocity field. Measurements of the turbulent kinetic energy density, dissipation rate, and various other turbulent quantities are described in Chapter IV.

## III.3 Experimental Setup

### III.3.A Facilities

The experiments described were performed using the small glass channel in the Hydraulics Laboratory at the Scripps Institution of Oceanography (SIO). The tank is 30 m long, 0.5 m wide, and 1 m deep. Waves are generated by a computer-controlled

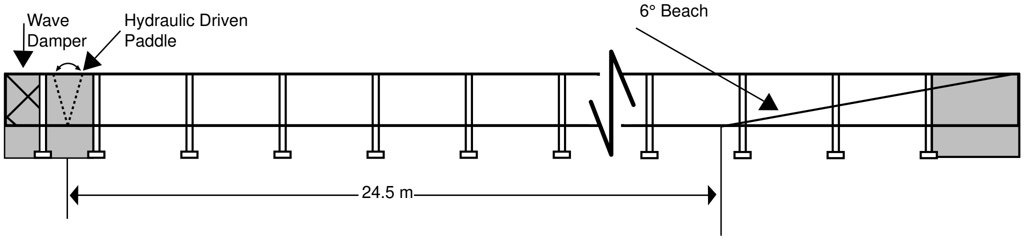

Figure III.4: Schematic showing the small glass channel in Hydraulics Laboratory at the Scripps Institute of Oceanography.

hydraulically-driven wave paddle at one end of the tank and are dissipated on a beach of 6° slope covered with a thick fibrous mat, see figure III.4. The toe of the beach starts 24.5 m from the resting position of the wave maker and the tank was filled to a working depth of 0.6 m with tap water.

### III.3.B Packet Generation

The wave maker was programmed to generate a breaking event at $(x_b, t_b)$ using dispersive focusing, a technique initially proposed by Longuet-Higgins (1974). Each wave packet has 32 separate frequency components spread across a bandwidth of $\Delta f / f_c$ centered at a frequency of $f_c$. The slope of each wave component was constant and the theoretical surface elevation at $(x, t)$ is given by

$$\eta(x,t) = \sum_{n=1}^{N} a_n \cos[k_n(x - x_b) - \sigma_n(t - t_b)] \tag{III.18}$$

where $a_n$, $k_n$, and $\sigma_n$ are the amplitude, wavenumber, and radian frequency of the $n$th component and $(x_b, t_b)$ the theoretical location and time of breaking. The phase of each component is determined by $(x_b, t_b)$ using

$$\cos(k_n x_b - \sigma_n t_b - \phi_n) = 1. \tag{III.19}$$

The maximum slope given by linear theory is $S = \sum a_n k_n$ and will be referred to as the input slope. Further details on the generation of a breaking wave packet can be found in Melville and Rapp (1985), Rapp and Melville (1990), and appendix A. The formulation here varies from that of Rapp and Melville (1990), in making the slope of each component equal as opposed to keeping the amplitude constant. It has been shown by Rapp and Melville (1990) that the important non-dimensional parameters for measuring energy loss are $S$, $\Delta f/f_c$, and $x_b k_c$, and our parameter space will be defined by these quantities. For the experiments described here we varied the frequency over $f_c = [0.88, 1.08, 1.28]$Hz, the bandwidth over $\Delta f/f_c = [0.5, 0.75, 1.00]$, and the breaking location over $x_b k_c = [28.5, 41.50, 57.92]$. For each of these 27 total cases the range of the input slope varied over $S = [0.28 : 0.02 : 0.54]$.

## III.3.C Measurements

To record surface wave height in the channel seven resistance wire wave gauges constructed at SIO were used with resistance measuring electronics from Danish Hydraulics Institute (Model 80-74G). Each gauge consisted of a pair of 0.25 mm diameter Nichrome 80 wires spaced 5 mm apart mounted to the flume from above with a rack and pinion which allowed for precise vertical positioning of the instrument. During the course of the experiments the gauges were placed along the midline of the tank and spaced approximately 3 m apart to minimize any flow disturbance on downstream gauges. For a given set of experimental conditions the six furthest wave gauges were shifted by 1 m while the first gauge remained fixed to serve as a control. This was repeated until the desired spatial resolution was obtained.

The A/D board (National Instruments PCI-6031E) had a maximum sample rate of 100kHz, so the ten channels used were each sampled at 10 kHz for 89 seconds, with an inter-channel delay of 1$\mu$s between each sample. The high data rate used was necessary for the hydrophone, which measured the acoustical signature of the breaking wave in order to obtain a measure of the duration of breaking. Prior to analysis the surface elevation timeseries were resampled to 100Hz. Along with the surface elevation and hydrophone data, the system also recorded the input signal to and resultant motion of the wavemaker. The control system then wrote the data to hard disk and waited eight minutes before repeating. This delay was sufficient to allow surface wave motions to die down before starting over. See appendix A. Variability of the amplitude and the phase of the surface elevation at the control gauge was within 0.8 mm and 1 ms or 0.1% of the wave period.

Results from Loewen (1991) (see also Deane and Stokes (2002)) showed that there was still significant energy in the hydrophone signal for frequencies above 5kHz. Use of a single wave gauge as a repeatability check along with the hydrophone allowed for an increased sampling rate of 50 kHz. The hydrophone used was located 20 cm off the floor of the tank at a distance of 4.96 meters from the wave paddle.

The duration of the breaking event is then found by differencing the start and stop times of breaking from the spectrogram of the hydrophone signal, as seen in fig III.5. This yields an estimate of the breaking duration but is limited to the active time of breaking, during which the wave impacts the water surface, air is entrained, and bubbles formed rise to the surface and break (Lamarre and Melville, 1991; Loewen and Melville, 1991; Deane and Stokes, 2002).

A megapixel video camera, Pulnix TM-1040, was used to record video imagery of the wave at the breaking location. The camera was run at a maximum frame rate of 30 Hz and the images were then saved as bitmaps to the hard drive. Analysis of the images allowed for measurement of the crest to trough distance, $2a$, the location of the breaking event relative to the wave paddle $x_b$, and the local height of the breaking wave $h$. The height at breaking for a plunging wave is well defined, but not so for a spilling wave. Since the wave tip falls under gravity we assign $h$ to be the vertical distance over which the spilling wave occurs as in figure III.2a. From these spatial measurements at breaking we define two slopes, the local slope, $hk_c$ where $k_c$ is the center wavenumber of the packet, and a slope based on the local amplitude, $ak_c$.

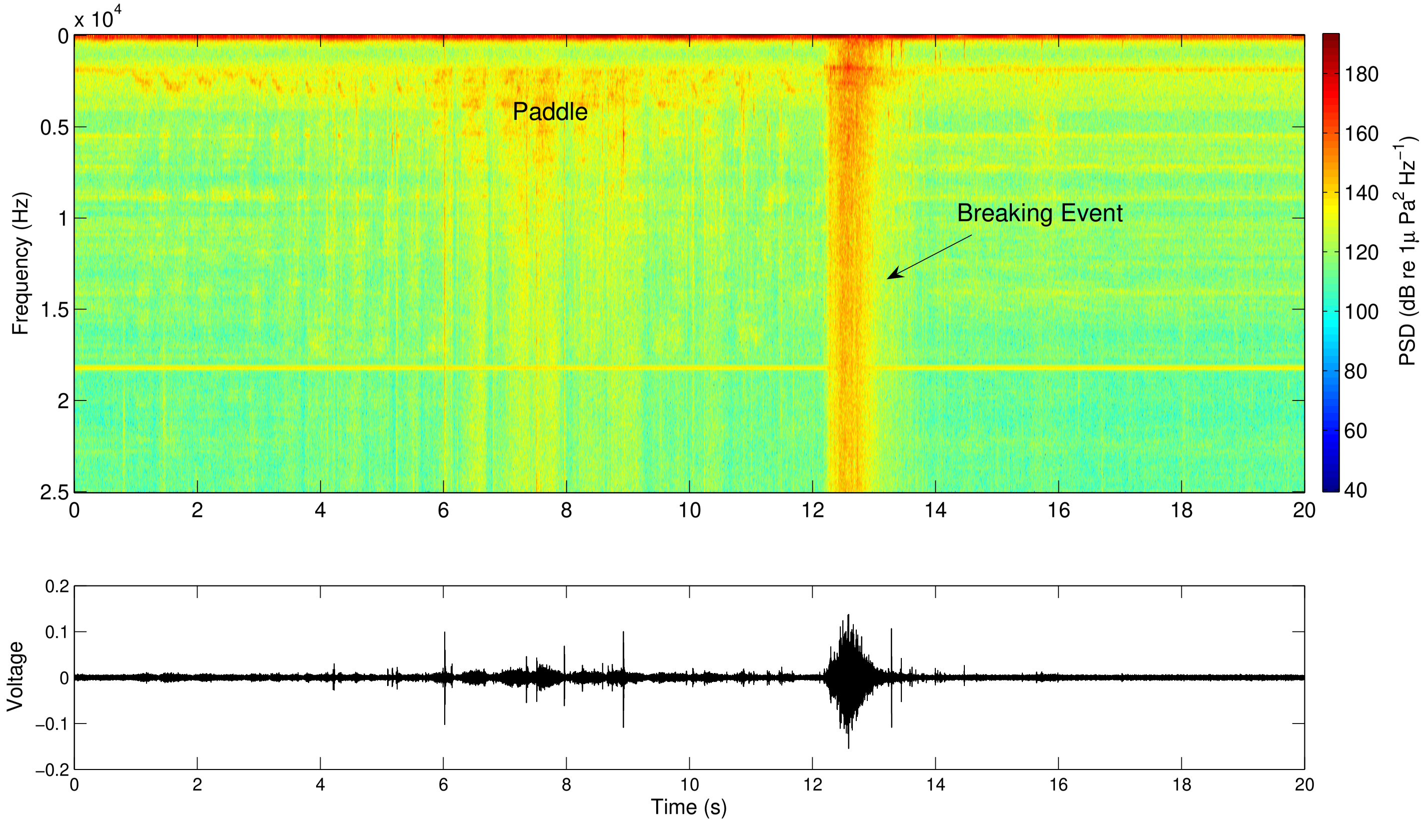

Figure III.5: a) Spectrogram and b) voltage time-history of a hydrophone signal. The breaking event is seen as a broad-banded signal in the spectrogram.

## III.4 Measurement of the dissipation rate

In order to measure the energy loss from breaking, the approach developed by Rapp and Melville (1990) is used. A packet of waves propagating down the tank is shown in figure III.6. As the wave approaches the theoretical breaking location it can be seen to steepen and then disperse as it moves downstream. At each gauge location the time-integrated potential energy per unit length can be calculated

$$E_p = \frac{1}{2}\int_0^t \rho g \eta^2 \,\mathrm{dt} \qquad \text{(III.20)}$$

Here $g$ is the acceleration due to gravity, $\rho$ the water density, and $\eta$ the surface elevation. As seen in figure III.7 the potential energy decreases rapidly as the wave approaches breaking and then levels out as the packet progresses downstream.

In figure III.7 we define two spatial regions for a breaking wave, the first is a region upstream and downstream of breaking where energy losses are due to friction at the sidewalls and tank bottom. Near the focal point of the packet a rapid decrease in the potential energy is seen as the wave undergoes breaking.

The normalized potential energy lost as a function of input slope can be seen by plotting $D = (E_{pf} - E_{pi})/E_{pi}$ (see figure III.8). Here $E_{pi}$ and $E_{pf}$ refer to the potential energy density at the initial and final wave gauges within the tank. It can be seen that as the input slope is increased the amount of energy lost increases quite rapidly once the wave begins breaking. The energy loss then begins to plateau at the onset of multiple breaking events. For the strongest case of single breaking up to approximately 35% of the input energy is dissipated. It is seen that variations in the distance to breaking do not seem to cause significant variation in the amount of energy lost, which agrees with previous work of Rapp and Melville (1990). However we do see variations in $D$ with changes in the packet bandwidth (figure III.9) in contrast to the findings of Rapp and Melville (1990). As stated previously the packets used in the experiments described are based upon a formulation in which each component has equal slope versus the constant amplitude method of Rapp and Melville (1990). As seen in figure III.10 for a given value

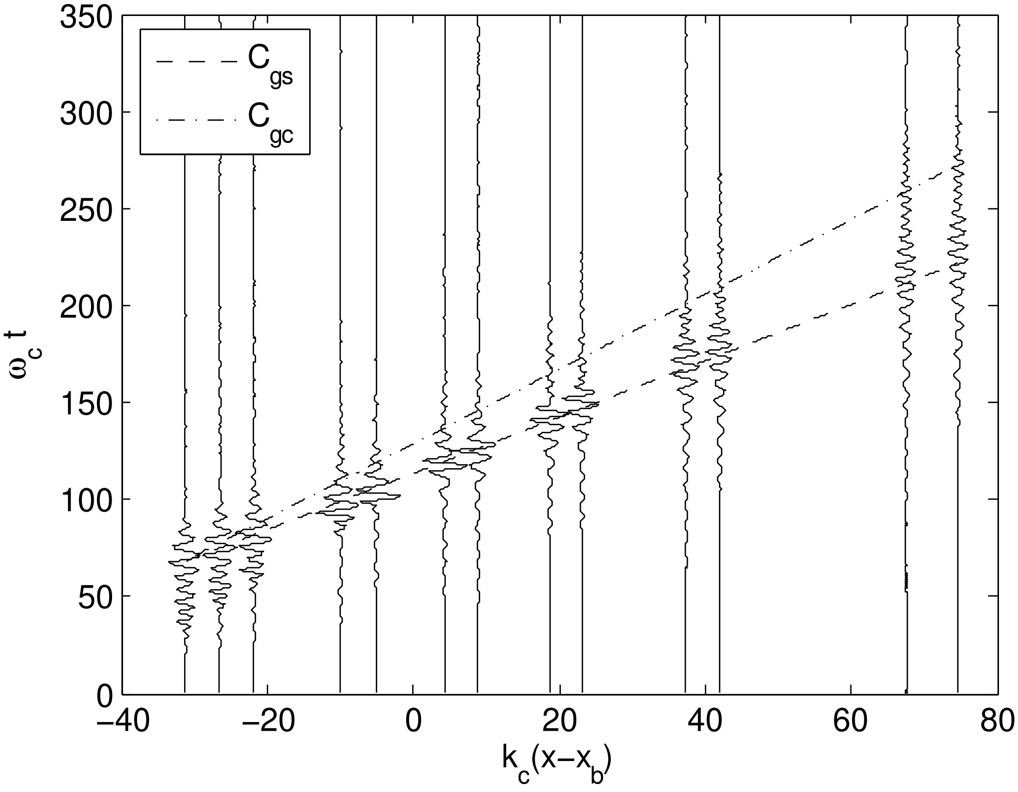

Figure III.6: A plot showing time series of surface elevation at a number of locations in the tank. Superimposed on top of the surface elevation are the group velocity lines corresponding to the center wave component $C_{gc}$ and the spectrally-weighted group velocity $C_{gs}$ as defined in the text. The packet parameters are $f_c = 1.08$Hz, $\Delta f/f_c = 0.75$, $x_b k_c = 41.50$, $S = 0.34$. Please note that the vertical scale of the time series are exaggerated relative to the horizontal scale on the graph.

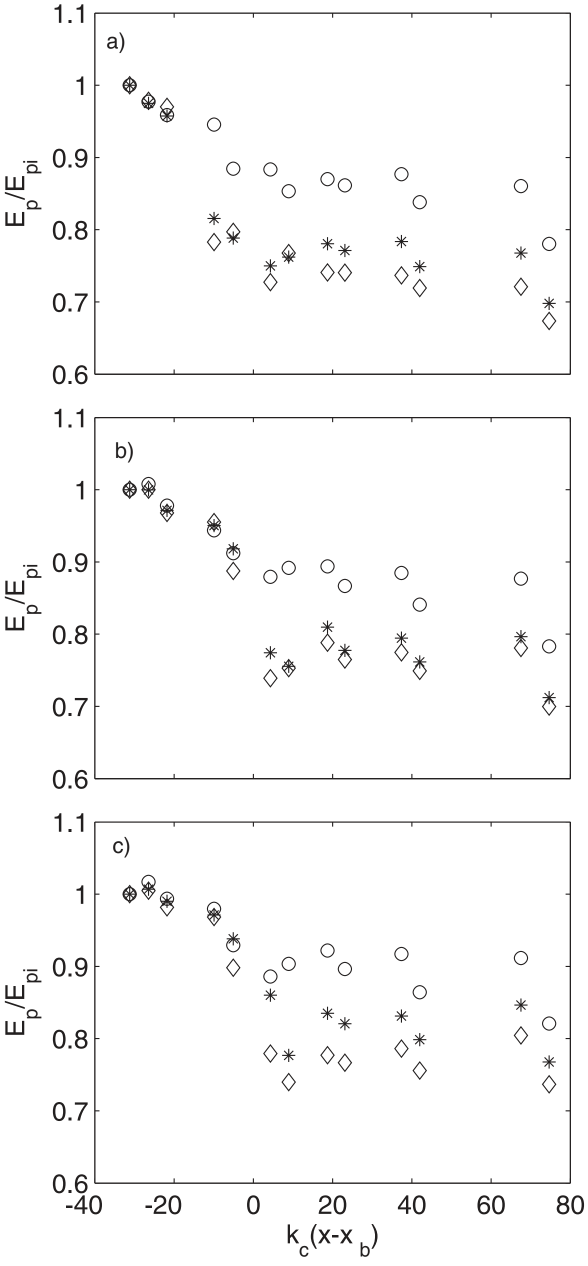

Figure III.7: Plot of the normalized potential energy, $E_p/E_{pi} = \eta^2/\eta_i^2$ as a function of $k_c(x-x_b)$ for three $\Delta f/f_c$, a) $\Delta f/f_c = 0.5$, b)$\Delta f/f_c = 0.75$, and c) $\Delta f/f_c = 1.00$. $E_{pi}$ is the potential energy at the furthest upstream gauge. The symbols denote different breaking events, non-breaking (S=0.28, $\circ$), spilling (S=0.36, $*$), and plunging (S=0.38, $\diamond$) for $f_c = 1.08$ Hz and $x_b k_c = 41.50$.

of the slope, bandwidth, and frequency the energy density is higher within the constant slope packet than for the constant amplitude case. Thus we expect that inception of breaking would occur at different slopes for these two formulations.

We now consider a control volume in which the edges of the volume are far upstream and downstream of breaking. We can then approximate the packet as being weakly nonlinear and apply equipartition of energy at these boundaries. Thus the local energy density at a given location is equal to twice the potential energy,

$$E = \rho g \eta^2. \tag{III.21}$$

The change in energy flux through this control volume over the time $t = t_1 \rightarrow t_2$ can be written as

$$\Delta F = \int_{t_1}^{t_2} C_{g_1} \rho g \eta_1^2 \mathrm{dt} - \int_{t_1}^{t_2} C_{g_2} \rho g \eta_2^2 \mathrm{dt} \tag{III.22}$$

where $(C_{g_1}, \eta_1)$ and $(C_{g_2}, \eta_2)$ are the group velocity and surface elevation at the edges of the control volume.

We now need to define a group velocity for the wave packet in order to apply (III.22). One could use the group velocity of the center component of the wave packet for $(C_{g_1}, C_{g_2})$,

$$C_{g_c} = \left.\frac{\partial \sigma}{\partial k}\right|_c = \frac{1}{2\sigma_c}\left[\frac{\sigma_c^2 + g k_c^2 (1 - \tanh^2(k_c h))}{k_c}\right] \tag{III.23}$$

However as seen in figure III.6 the wave packet is not seen to be traveling at the group velocity of the center component. The packet propagation more closely follows a weighted average of the group velocities as defined by

$$C_{g_s} = \frac{\int C_{g_n} a_n^2 d\sigma}{\int a_n^2 d\sigma} \tag{III.24}$$

where $C_{gs}$ is the spectrally-weighted group velocity and $a_n$ and $C_{g_n}$ are the amplitude and group velocity of the $n$th component of the wave packet. We now assume $C_{g_1} = C_{g_2} = C_{g_s}$ and equation (III.22) simplifies to

$$\Delta F = \int_{t_1}^{t_2} \rho g C_{g_s} \left(\eta_1^2 - \eta_2^2\right) \mathrm{dt} \tag{III.25}$$

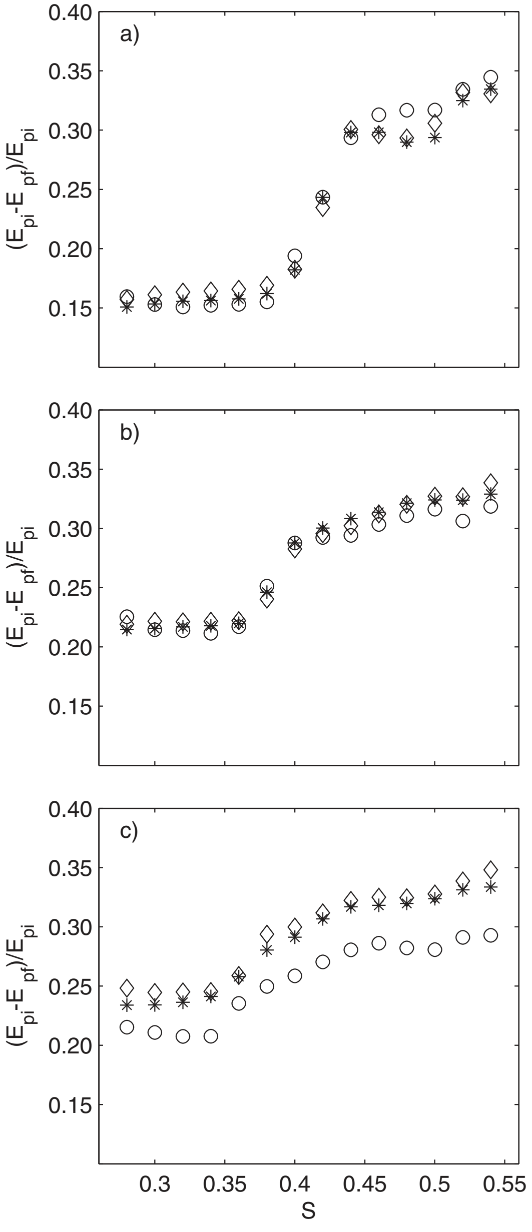

Figure III.8: Fractional loss of energy as a function of input slope for a) $f_c$ = 0.88 Hz, b) $f_c$ = 1.08 Hz, c) $f_c$ = 1.28 Hz. All packets have $\Delta f/f_c = 0.75$ with $x_b k_c = 28.5\,(\circ)$, $x_b k_c = 41.50\,(*)$, and $x_b k_c = 57.92\,(\diamond)$

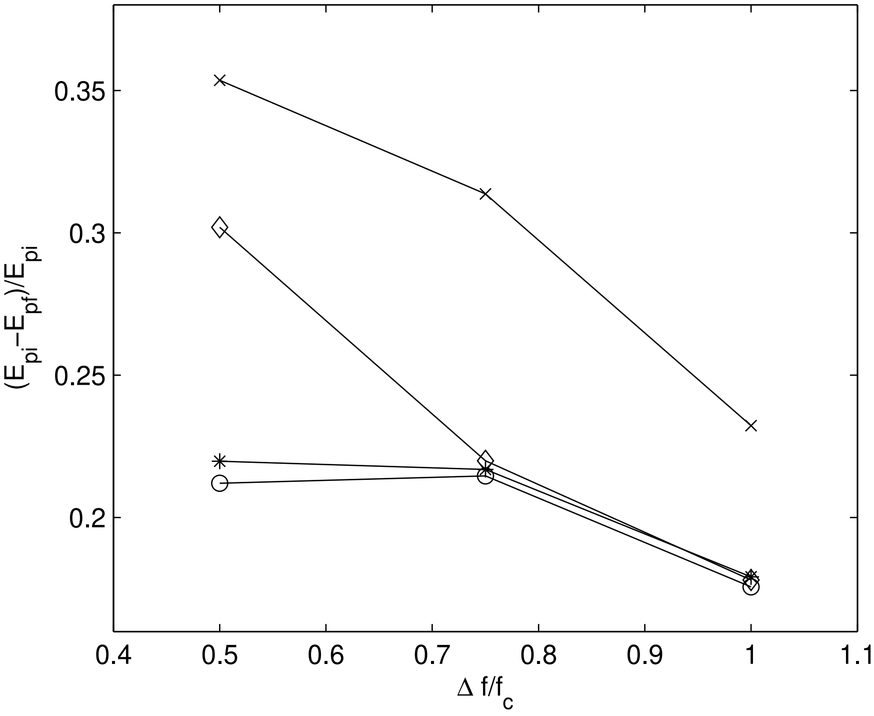

Figure III.9: Fractional loss of energy as a function of bandwidth. All packets have $f_c$ = 1.08 Hz, and $x_b k_c = 41.50$ with $S = 0.28$ (○), $S = 0.32$ (∗), $S = 0.36$ (◇), and $S = 0.46$ (x).

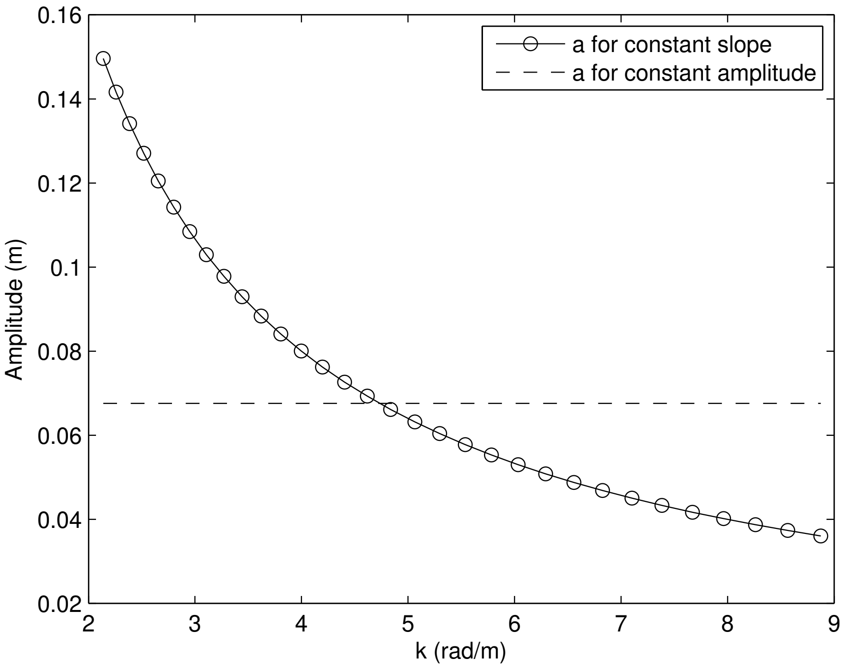

Figure III.10: Comparison of the theoretical amplitude for each wave component in the packet using the constant slope formulation and the constant amplitude method of Rapp and Melville (1990). For a given value of $S$, $\Delta f/f_c$, and $f_c$ the constant slope packet has more energy than the constant amplitude case.

We wish to evaluate the dissipation rate due to a single breaking event. The loss due to breaking needs to be isolated from from that due to non-breaking effects such as friction with the bottom and side walls of the tank. We will define the total change in energy flux within the control volume to be

$$\Delta F_{tot} = \Delta F_b + \Delta F_{nb} \tag{III.26}$$

where $\Delta F_b$ is the change due to breaking and $\Delta F_{nb}$ is the change due to non-breaking effects. The non-breaking effects are quantified using the change in energy flux from the non-breaking wave case.

As stated earlier, the time of active breaking has been defined as the time during which the breaking event is acoustically active. However measurements of the spatial duration of breaking, $\Delta x_b$, can be obtained from figure III.7. Through use of the spectrally averaged group velocity, one can then get a measure of the duration of breaking, $\tau_x = \Delta x_b / C_{g_s}$. A plot of the mean duration of breaking from the hydrophone measurement as well as the spatial measurement is shown in figure III.11 for the range of bandwidth used in this study. As the bandwidth is increased the onset of breaking shifts to higher values of $S$ and the range over which single breaking occurs is also extended.

The agreement between the two estimates of $\tau$ varies with the bandwidth and can be up to 20%. The measure of $\tau_x$ is subject to inaccuracies due to the operator error in defining $\Delta x_b$ for a given set of parameters. Despite this discrepancy in the mean values of $\tau$ at larger values of $S$, there is very little qualitative difference between the ensemble-averaged $\epsilon_l$ calculated from these two measures of $\tau$, where the ensemble is the entire parameter space considered for a single value of $S$. The remainder of the data shown will use the measure of $\tau_h$ from the hydrophone since these are less subjective measurements. It is seen that the duration of the breaking increases as the input slope is increased and approaches one wave period in duration. This is consistent with Rapp and Melville (1990) and Loewen and Melville (1991) who showed that the breaking duration is approximately one wave period and that the time of active breaking correlates well with the hydrophone signal.

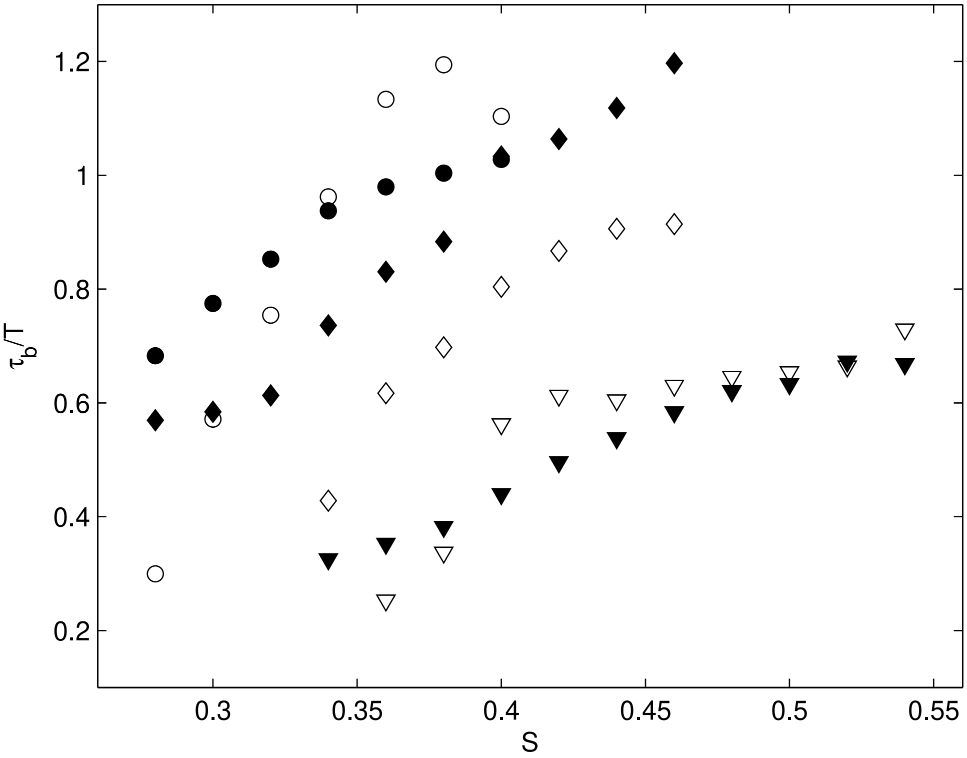

Figure III.11: Mean duration of breaking ($\tau/T$) versus input slope as measured from the hydrophone, $\tau_h$, and $\Delta x_b$, $\tau_x$. The mean is taken over $f_c$ and $x_b k_c$ for $\tau_x$ (Open Symbols) and $\tau_h$ (Filled Symbols). $\Delta f/f_c = 0.50\,(\circ)$, $\Delta f/f_c = 0.75\,(\diamond)$, and $\Delta f/f_c = 1.00\,(\triangledown)$.

The average dissipation rate per unit length of crest can now be defined as

$$\epsilon_l = \frac{\Delta F_b}{\tau_b} = \frac{\int_{t_1}^{t_2} \rho g C_{g_s} \left(\eta_1^2 - \eta_2^2\right) \mathrm{dt}}{\tau_b} \qquad \text{(III.27)}$$

## III.5 Results

The measured dissipation rate as a function of input slope, $S$, similar to the data presented by Melville (1994) is shown in figure III.12, along with the measurements of Melville (1994). The solid line shows the mean of $b$, $\langle b \rangle$, over all parameter space for a given value of $S$ not just the subset presented in figure III.12. The error bars denote the standard deviation of the data at each $S$. The measurements of $b$ from our data show a dependence of $b$ on the input slope, which agrees with the findings of Melville (1994). However for the range of slopes considered by Melville (1994), multiple breaking events begin at $S \approx 0.30$, where multiple breaking for our wave packets do not start until $S = 0.40$. The two experiments explored a similar range of parameter space, used wave tanks of nearly the same dimensions, and both used a constant slope formulation for generating wave packets. The main difference between the two experiment conditions is the fact that the water depth for Loewen and Melville (1991) was 0.38 m versus 0.6 m used here. For the range of wavelengths considered in each experiment, $kh$ varied from 1.35-2.54 for Loewen and Melville (1991) and from 1.95-3.96 for the experiments described here. A larger number of wave components experience shallow-water effects and will likely break at a lower value of $S$ than for our data. Despite the differences in the nature of the breaking between the measurements, the rate at which $b$ increases for single breaking events is qualitatively similar.

The effect of the other parameters on the dissipation rate is investigated by looking at the variation in the residual values of $b$, $b_r = b - \langle b \rangle$. The variation of $b_r$ with the packet bandwidth and breaking location is shown in figure III.13. The solid line is the mean value of $b_r$ for a given value of $\Delta f / f_c$ or $x_b k_c$. The error bars represent the standard deviation of $b_r$. The dependence of $b_r$ on the bandwidth and breaking location is smaller than that of the slope and is thus assumed to be negligible.

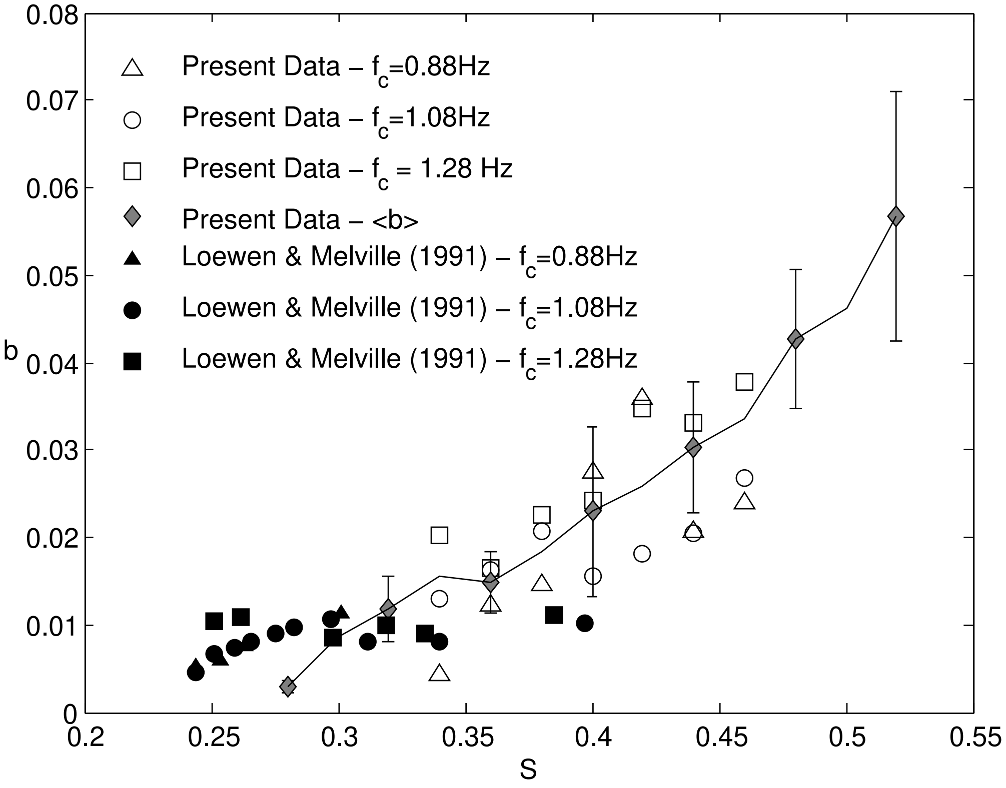

Figure III.12: Plot of $b$ versus S for similar experimental conditions as Loewen and Melville (1991). The grey diamonds represent $\langle b \rangle$, the mean of the data for all parameter space for a given slope, not just the subset considered here (see below). The error bars denote the standard deviation of $b$ over all parameter space for a given value of $S$. The data of Melville (1994) are shown with filled symbols and the measurements presented here are shown with open symbols. Frequencies plotted are $f_c = 0.88$Hz ($\triangle$), $f_c = 1.08$Hz ($\circ$), and $f_c = 1.28$Hz ($\square$). For the present data, $\Delta f/f_c = 0.75$ and $x_b k_c = 28.5$ for all $f_c$, while for Melville (1994), $\Delta f/f_c = 0.73$ and $x_b k_c = 28.3$ for all $f_c$.

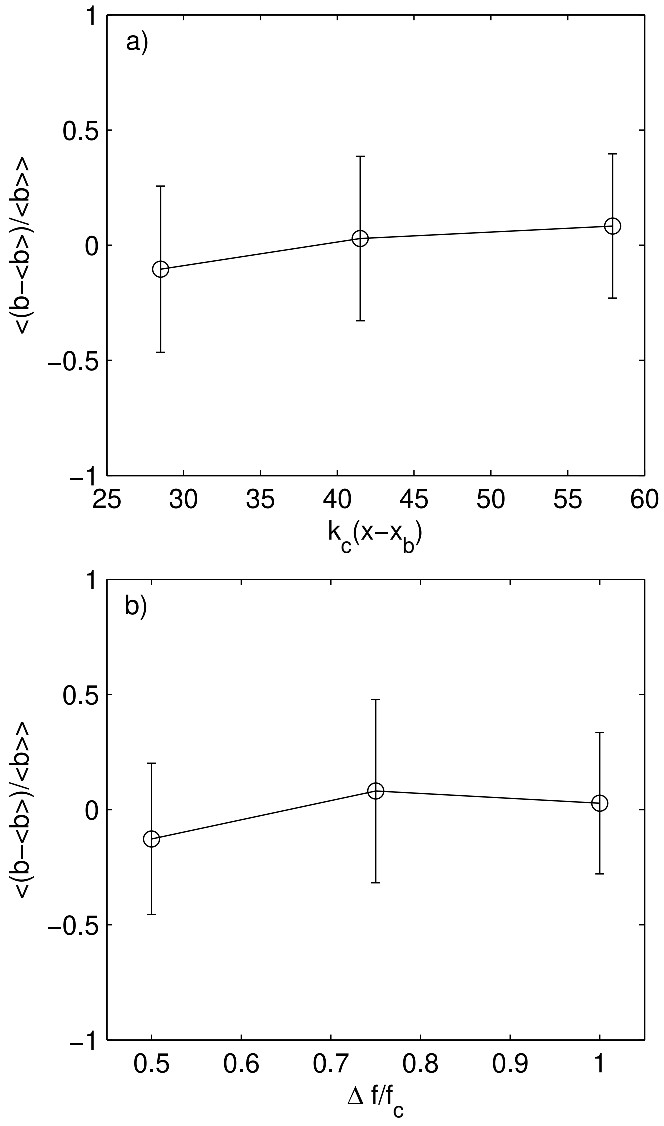

Figure III.13: Plot of the normalized residual value of $b$ versus a) distance to breaking, $x_b k_c$ and b) packet bandwidth, $\Delta f/f_c$. The solid line denotes the average of all three center frequency data for that bandwidth and the error bars represent the standard deviation of the data.

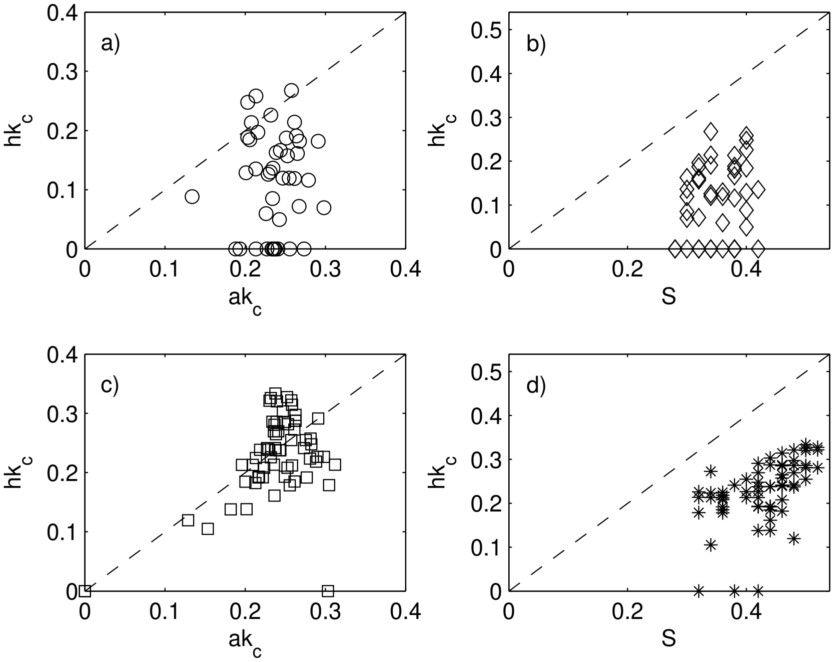

Figure III.14: The relationships for spilling waves are shown in a) for the local slope ($hk_c$) versus the slope based on the local amplitude ($ak_c$) and in b) for the local slope versus the input slope ($S$). The relationships for plunging waves are shown in c) for the local slope versus the slope based on the local amplitude and in d) for the local slope versus the input slope. The dashed line in each plot has a slope of one. See figure III.2 for the definition of $a$ and $h$.

The relationships between the various estimates of the slope are shown in figure III.14. Comparisons for spilling waves are shown in figures III.14a and III.14b and for plunging waves in figures III.14c and III.14d. We can see that $hk_c$ approaches $ak_c$ as the wave becomes steeper and that the value of $hk_c$ is lower than the input slope $S$ for both spilling and plunging waves.

The measured values of $\epsilon_l$ for three measures of the slope are shown in figure III.15. The estimates of $b$ for $hk_c$ and $ak_c$ are binned using a bin spacing of 0.02 $hk_c$ or $ak_c$ which corresponds to the spacing of the input slope, $S$. The mean of $b$ is then taken over all of the data within a given bin. For comparison the value of the model given by (III.17) for the range of slopes represented is also shown. It can be seen in figure III.15a that this simple model reproduces the dissipation rate within the plunging breaking regime quite well and is within an order of magnitude. Assuming the point at $hk_c \approx 0.04$ to be anomalous, the value of $\epsilon_l$ for the spilling cases is seen to increase across the range of slopes considered, but at a rate slower than $hk_c^{5/2}$. The anomalous value of $b$ near $hk_c \approx 0.04$ is assumed to be due to the difficult nature of assigning a value of $h$ to these weakly spilling waves. See the discussion in section III.3.

The dissipation rate as a function of the input slope, $S$ can be seen to increase across the entire range considered. As mentioned previously the qualitative nature of breaking varies with the bandwidth. This range is well correlated with the input slope and covers a larger range of $S$ as the bandwidth is increased. This could account for the steady increase in $b$ across the entire input range, and is consistent with the steady rise in both the amount of energy lost from breaking and the breaking duration (figures III.8 and III.11).

We also compare $b$ to $ak_c$ in figure III.15c, where $a$ is the amplitude of the wave before breaking. It is seen to increase with increasing values of $ak_c$, but then decreases after the packet begins to undergo plunging breaking. This decrease is unexpected and is thought to be due to the poor correlation between $hk_c$ and $ak_c$, see figure III.14. The location at which the decrease occurs changes as the bin width is increased or decreased. Examination of the non-binned data shows that for high values of $ak_c$ there are only a

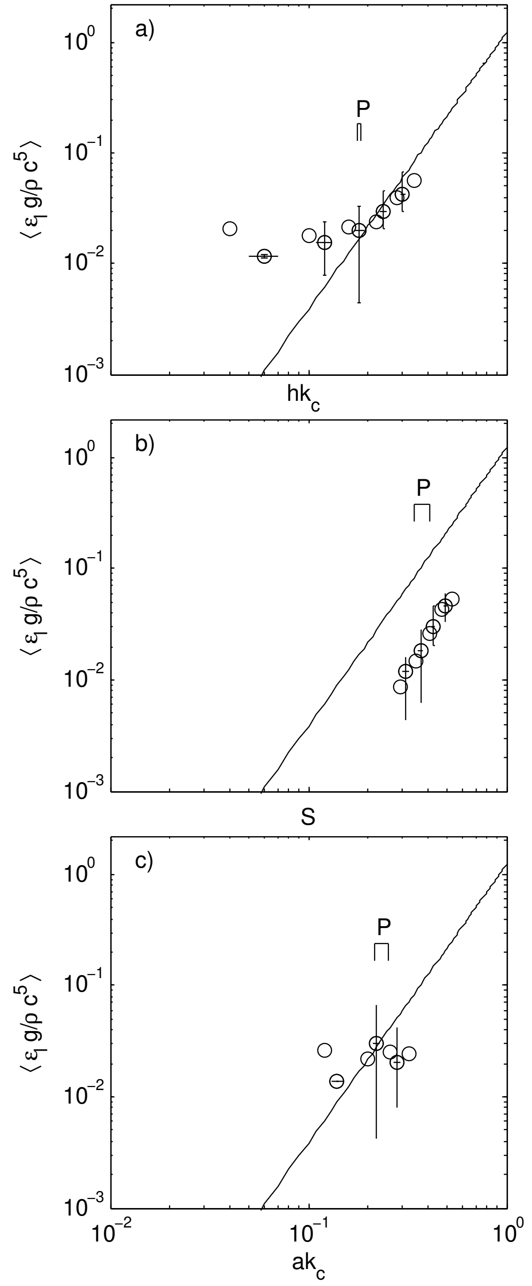

Figure III.15: Plot of the mean breaking parameter, $\langle b \rangle$, versus a) the local slope at breaking, $hk_c$, b) the input slope to the wavemaker, $S$, and c) the slope based on the amplitude at breaking, $ak_c$. The solid line is the predicted value of $b$ using (III.17). The vertical lines represent the range of the data over which the average is taken. P is the region over which plunging breaking begins.

few breaking waves with a lower $b$ and this skews the average value of $b$ for that bin to lower values.

The inertial estimate of the dissipation rate used in formulating the model is an order of magnitude estimate. Improvement upon this relies on measuring a scaling factor

$$\epsilon_m = \chi \frac{u^3}{l} \tag{III.28}$$

where $\chi$ is a constant. The range of $\chi$ needed for agreement with our model can be determined from the experimental data through

$$\chi = \frac{\epsilon_{measured}}{\epsilon_{model}} \tag{III.29}$$

If a $hk^{5/2}$ line is fit to the data of figure III.15a within the plunging wave regime and used to evaluate (III.29), then we find $\chi = 0.3$.

## III.6 Discussion

We have proposed a simple model of a plunging breaking event and related the subsequent dissipation rate to measurable wave parameters. Within the range of the data shown there is good agreement between the data and the proposed model. The range of $b$ found is on the high end of values seen in the literature, see table III.1. The measurements of Phillips et al. (2001) are still two orders of magnitude smaller than our estimates of $b$ but it is assumed this is partly due to the indirect method used to estimate $b$. We also find a larger value of $b$ for unsteady breaking in the laboratory as compared to the data of Loewen and Melville (1991) which Melville (1994) used in his estimates of $b$ (see figure III.12). This can be attributed to the shallower water depth used by Loewen and Melville (1991) which could induce breaking at smaller values of $S$ as compared to our experiments using a depth of 0.6 m. The measurements of Duncan (1981, 1983) are of the same order of magnitude as our unsteady plunging waves but are for quasi-steady spilling waves. Excluding the data point at $hk_c \approx 0.04$ in figure III.15a we see that $b$ increases with increasing slope for spilling waves. We will attempt to explain this through use of an argument similar to that employed in section III.2.C.

We can model the spilling event by defining the velocity and length scales using the friction velocity, $u_*$, and $h = L\sin\theta$, the vertical height of the breaking region (see figure III.2a).

$$u_* = \sqrt{\frac{\tau}{\rho}} = \sqrt{\frac{\rho' g A \sin\theta}{L\rho}} \tag{III.30}$$

$$h = L\sin\theta \tag{III.31}$$

where $\tau$ is the shear stress exerted by the breaking wave on the fluid underneath, $\rho$ is the fluid density, $\rho'$ the density of the fluid in the breaking region, $A$ the area of the breaking region, $L$ the length of the breaking region, and $\theta$ the angle of the breaking region relative to horizontal. See figures III.1a and III.2a. We will scale $A = \beta L^2$.

The inertial estimate of breaking is defined as

$$\begin{aligned} \epsilon_l &\approx \rho A \epsilon_m \propto \rho A \frac{u_*^3}{h} && \text{(III.32)} \\ \epsilon_l &\propto \rho\beta L^2 \frac{\left(\frac{\rho' g A \sin\theta}{L\rho}\right)^{\frac{3}{2}}}{L\sin\theta} && \text{(III.33)} \\ &\propto \beta^{\frac{5}{2}} L^{\frac{5}{2}} \left(\rho'/\rho\right)^{\frac{3}{2}} \rho g^{\frac{3}{2}} \sin^{\frac{1}{2}}\theta. && \text{(III.34)} \end{aligned}$$

If we multiply (III.34) by $c^5 k^{5/2} g^{-5/2}$ we arrive at an expression in the form $\epsilon_l = b\rho g^{-1} c^5$,

$$\epsilon_l = \beta^{\frac{5}{2}} L^{\frac{5}{2}} \left(\rho'/\rho\right)^{\frac{3}{2}} \sin^{\frac{1}{2}}\theta \rho g^{-1} c^5 \tag{III.35}$$

Now we scale $L = \alpha\lambda_b$ where $\lambda_b$ is the wavelength of the breaking wave as defined by Duncan (1981). Since $k = 2\pi/\lambda$, we get $Lk = 2\pi\alpha$. For this breaking event $\theta$ defines the steepness of the breaking region and we can relate this to the slope at breaking, $\sin\theta = h/L = hk/2\pi\alpha$. Inserting this into (III.35), $b$ becomes

$$b = \Upsilon\,(hk)^{\frac{1}{2}}\,. \tag{III.36}$$

where $\Upsilon = \beta^{\frac{5}{2}} (2\pi\alpha)^2 \left(\frac{\rho'}{\rho}\right)^{\frac{3}{2}}$.

We can see in figure III.16 that the inertial model for the plunging waves agrees well with the mean values of the breaking parameter shown in figure III.15. The prediction of an inertial model for the spilling breaking waves shows an approximate $hk^{1/2}$

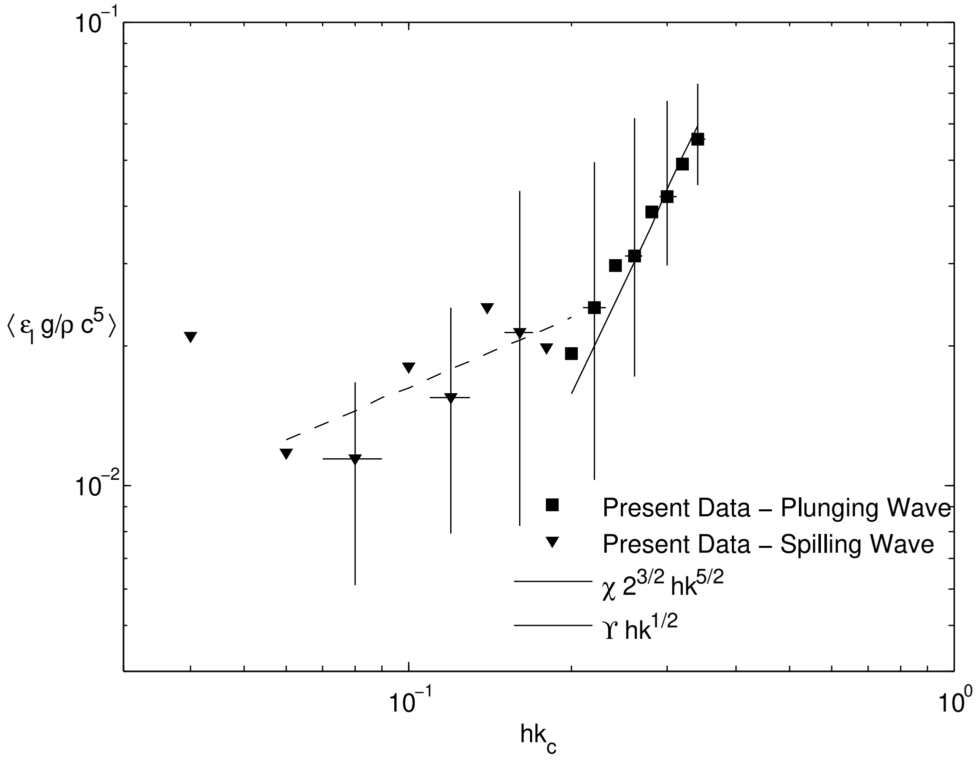

Figure III.16: The normalized dissipation rate, $b$, for spilling and plunging breaking measured here versus the local slope, $hk_c$. The least squares fit to $b$ using $hk^{5/2}$ for plunging waves and $hk^{1/2}$ are shown and give an estimate of how well the model performs, see (III.17) and (III.36). The error bars define the range of the data over which the averages were computed.

dependence, ignoring the anomalous point at $hk_c = 0.04$. The spread of the mean breaking parameter here is larger and could partially be attributed to errors in measuring $h$ for a spilling wave.

An estimate of $\beta$ and $\alpha$ for quasi-steady breaking can be made using the tabulated data presented in Duncan (1981). Neither experiment has a measure of $\rho'/\rho$, but Longuet-Higgins and Turner (1974) and Longuet-Higgins (1974) have suggested a probable range to be 0.8-1. For simplicity we will assume $\rho'/\rho = 1$. We have not measured $\beta$ or $\alpha$ for the current experiments, but we can fit the spilling wave data to a $hk^{1/2}$ line to get an estimate of

$$\Upsilon = \beta^{\frac{5}{2}}(2\pi\alpha)^2. \tag{III.37}$$

Values of $\Upsilon$ for the quasi-steady case of Duncan (1981) was computed using the tabulated data he presented and is found to be $\Upsilon = 0.007 - 0.019$. For our spilling wave data we find $\Upsilon = 0.05$. Part of this difference could be attributed to assumption that $\rho'/\rho = 1$, but the measured value of $\Upsilon$ still varies by an order of magnitude from Duncan (1981). The mean values of $b$ for the spilling and plunging wave cases are shown in figure III.17 for $hk_c$ along with the model value of $b$ for both types of breaking waves. Additionally we plot the measurements of $b$ from Duncan (1981, 1983) using $hk \approx kL\sin\theta$ as the local slope.

We see that there is good agreement between the unsteady and quasi-steady breaking with the model described by (III.36). This suggests that the unsteady breaking wave could simply be a limiting case of the quasi-steady wave. Melville (1994) noted that the dimensionless dissipation rate of Duncan (1983) varied significantly with changes in $\theta$ and thus this model would provide an explanation for that behavior, since $\theta$ is related to $hk$. The flow is seen to undergo a change at the onset of plunging breaking and the dissipation rate increases much more rapidly with slope. The forced nature of the breaking investigated by Duncan (1981, 1983) could also account for the larger value of the breaking parameter, $b$.

As mentioned previously the inertial estimate of the dissipation rate only gives us an order of magnitude estimate. We found that $\epsilon_l = \chi u^3/l$ for plunging waves yielded

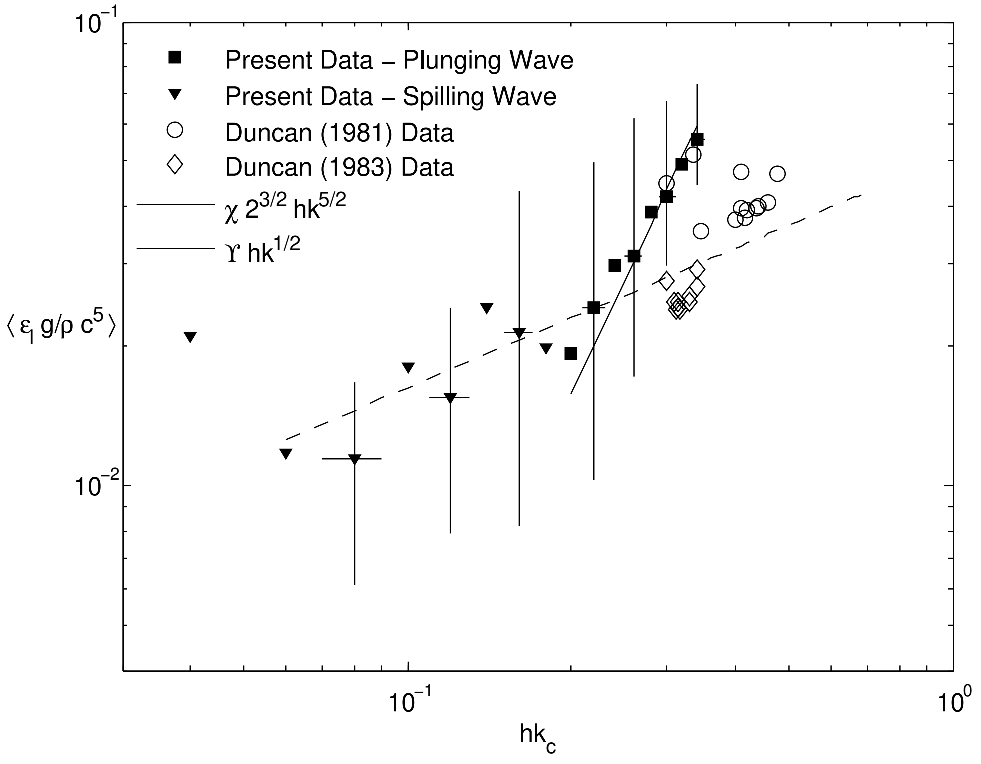

Figure III.17: The normalized dissipation rate, $b$, for spilling and plunging breaking measured here versus the local slope, $hk_c$ as in figure III.16. Also shown are values of $b$ from Duncan's data of 1981 and 1983, using $h \approx L \sin\theta$ as the local height at breaking (see figure III.1a). The error bars define the range of the data over which the averages were computed.

$\chi = 0.30$, but we wish to see how this compares with measurements of $\chi$ in the literature.

Sreenivasan (1984) provides measurements of $\chi$ in grid-generated turbulence and finds that $\chi$ tends to 0.43 for $R_\lambda > 50$, where $R_\lambda$ is the Taylor microscale Reynolds number. The Taylor microscale Reynolds number is defined as $\langle u^2 \rangle^{1/2} \lambda / \nu$ where $\langle u^2 \rangle^{1/2}$ is an rms velocity and $\lambda$ the Taylor microscale, see section IV.4. Pearson, Krogstad, and van de Water (2002) extended this work to include results of typical wake flows and found that $\chi \approx 0.5$ for high $R_\lambda$. As will be shown in section IV.4 the values of $R_\lambda \approx 450$ approximately 3.5 wave periods after breaking.

Melville et al. (2002) has used video imagery to directly measure $\Lambda(\mathbf{c})\,\mathrm{d}c$. Melville, Romero, and Kleiss (2005) obtained concurrent video imagery and surface elevation profiles from the use of scanning Lidar. Through identification of individual breaking events in the video images, spatial wave profiles can be obtained. The extent of the whitecap from the images will define the region of active breaking and the spatial profiles will allow for determination of the height of the breaking wave, and subsequently an estimate of $b$. Since measurement of the statistics of breaking can only occur in the field, the ability to measure $b$ will allow for accurate estimates of dynamical quantities such as dissipation and momentum flux.

# Chapter IV

# Analysis of the turbulence generated by a plunging breaking wave

## IV.1 Introduction

Breaking waves are a common feature on the ocean surface and play a important role in mediating air-sea transfers of gas, momentum, and energy. The breaking process entrains air mixing it down to a depth on the order of the wave height. The breaking process generates currents, limits the height of breaking waves, and dissipates surface-wave energy. The wave environment is complex, with waves generated by local winds interacting with swell from distant storms as well as surface currents. In addition breaking occurs on a wide variety of scales and the energy lost by breaking generates turbulence in the ocean boundary layer. In order to fully understand the roles of many of these processes, detailed measurements need to be conducted. This is difficult in the field due to the intermittent nature of breaking which makes measurements with high spatial and temporal resolution difficult. In comparison the laboratory provides us with a highly-controlled environment in which high-precision, high-resolution measurements can be conducted in order to better understand the dynamics of breaking waves.

Rapp and Melville (1990, RM) measured turbulence generated by unsteady breaking waves in the laboratory. Simple flow visualization with the use of dye permitted estimates of the extent of mixing by breaking as well as the rate of growth of the turbulent patch. They employed laser Doppler anemometry (LDA) on a regular grid in a number of realizations of the flow. While the grid spacing was coarse compared to modern DPIV standards, a vortex structure was seen in the mean velocity field. Computing the energy balance across the breaking region showed that approximately 90% of the energy from the breaking event was dissipated within four wave periods. The turbulent kinetic energy was found to subsequently decay like $t^{-1}$, where $t$ is the time after breaking. It was shown later by Lamarre and Melville (1991) that about 50% of that energy was lost through work done by the flow in entraining air against buoyancy forces.

Duncan, Philomin, Behres, and Kimmel (1994); Duncan, Qiao, Philomin, and Wenz (1999) looked at detailed measurements of the crest evolution in weakly spilling breaking waves. The wave forms a bulge at the top of the face of the waves and capillary waves radiate away from the toe at the base of the bulge. The toe then accelerates down the face of the wave and continues down the face of the wave as the resulting turbulent disturbances are swept back across the crest.

Lin and Rockwell (1995) used PIV techniques to study the instantaneous structure of a quasi-steady breaking wave. Spilling breaking waves were generated using a hydrofoil and the flow velocity was varied over a range of Froude numbers based on the hydrofoil chord. The transition from small-scale capillary structure to a large-scale separated flow occurs over a small range of Froude numbers. Regions of concentrated vorticity of opposing signs were shown to exist beneath the crests and troughs of the small-scale structures. In the large-scale case the jump in radius of curvature in the free surface is a source of vorticity. It has been shown that the curvature of the free surface in any steady flow can generate vorticity, and that capillary waves can be the dominant vorticity generation mechanism (Longuet-Higgins, 1992; Batchelor, 1967). In both the large and small-scale case the maximum value of the circulation was found to be the same order of magnitude. A study performed by Dabiri and Gharib (1997) showed that vorticity in a spilling breaker can also be generated by a deceleration of the surface layer.

Bonmarin (1989) used cine images of breaking waves to describe the various stages of breaking. A number of geometrical parameters were used to describe the asymmetry and steepness of the waves as they approach breaking. The shape of the plunging jet and the subsequent splash-up were also investigated.

Perlin, He, and Bernal (1996) used PIV and high speed imagery techniques to image plunging breaking waves as the jet approaches the free surface. The ambient flow in the tank without breaking was used to calculate a background noise level and its subsequent vorticity. The vorticity in the pre-breaking wave field was shown to be the same order of magnitude as the quiescent tank and thus can be considered irrotational up to the point of breaking. Parasitic capillaries are seen to appear when the face of the wave becomes approximately vertical and the jet begins to form, presumably caused by the discontinuity in the slope near the toe. As the jet lengthens the discontinuity diminished and the capillary waves vanish. Along the upper surface of the breaking wave jet, transverse irregularities are seen but are do not exist on the rear side of the wave crest. It is thought that these could be caused by turbulent-wave interactions or by transverse waves on the surface of the jet as described by Longuet-Higgins (1995). The maximum jet velocity was found to be approximately 30% larger than the corresponding wave phase speed.

Chang and Liu (1998) used DPIV to measure the velocity field within and below a quasi-periodic plunging waves in shallow water. They found that the acceleration within the tip of the plunging wave was approximately 1.1 times the gravitational acceleration. Velocity measurements in the $x-y$ plane near the surface revealed the presence of vorticity in this plane along with a non-zero component of the mean velocity in the $y$ direction. This suggests that the motion is not entirely two-dimensional in the mean.

Chang and Liu (1999) used DPIV to measure the turbulent flow beneath quasi-periodic breaking waves in shallow water. A train of ten monochromatic waves were generated and data was collected from the first five breakers in a streamwise plane. The water depth was 20 cm, the wave height was 14.5 cm, and the wavelength was 1.21 m. Ensemble averaged statistics were employed to characterize the velocity fields, using at an ensemble of least 16 events to define the turbulent velocity. In order to account for the missing turbulent velocity component in the cross-stream $y$-direction, $v$, they assumed that the flow was similar to a plane wake. This assumption was based on an analysis by Svendsen (1987) of breaking waves in the surf zone. Terms in the turbulent kinetic energy, TKE, budget were averaged over one wave period and a balance between production, advection by the mean flow, and dissipation was found after the first few wave periods. Here production is an exchange of energy between the mean and turbulent flows. The estimated time scale of decay of the turbulence is given by $k/\epsilon$, where $k$ is the TKE density per unit mass and $\epsilon$ the dissipation rate per unit mass. This time scale was found to approach one wave period within four wave periods, suggesting the existence of a quasi-steady state.

Veron and Melville (1999) used a coherent acoustic Doppler profiler to measure turbulence generated by breaking waves in both the laboratory and the field. Measurements of $u(x, t)$ were obtained at a depth of 10 cm below the mean water level. The turbulence was defined to be the residual velocity after the surface-wave-induced motions were filtered out. Evaluation of the wavenumber spectra showed the existence of an inertial subrange. The temporal evolution of the dissipation rate was found to behave as $\epsilon \propto t^{-n}$, with $n$ varying between -1 and -1.5.

Melville et al. (2002, MVW) used DPIV to investigate the post-breaking velocity field under unsteady breaking waves in the laboratory. In order to describe the large-scale flow with sufficient resolution a mosaic of images was used to reconstruct the velocity field. Analysis of the ensemble-averaged velocity field showed the existence of a large coherent vortex which propagated downstream under the influence of its image vortex above the water. The turbulent kinetic energy was found to decay with a $t^{-1}$ dependence. These findings are consistent with the earlier LDA measurements of RM. The experiments of MVW were not specifically designed to measure the TKE budget, but an estimate of the balance of the terms was possible. An assumption of isotropy was used in order to compute the dissipation rate. Comparison of horizontally integrated terms implied that a simple relationship between production and dissipation in the turbulent cloud did not apply, and that there was a likely balance between advection and turbulent transport. Hinze (1975) shows that assuming isotropy the dissipation rate becomes

$$\epsilon = 15\nu\left\langle\left(\frac{\partial u}{\partial x}\right)^2\right\rangle \tag{IV.1}$$

where $\nu$ is the kinematic viscosity and $u$ the turbulent velocity component in the $x$ direction. Equation (IV.1) evaluated for the DPIV data was shown to agree with estimates computed by Veron and Melville (1999) using (IV.1) along with a fit to the inertial subrange of wavenumber spectra.

The numerical simulation of breaking surface waves depend on results generated in the laboratory to help drive and validate models. Chen, Kharif, Zaleski, and Li (1999) conducted detailed two-dimensional simulations of plunging breaking waves past the point of impact. It was found that approximately 80% of the wave energy was dissipated within three wave periods and the temporal evolution of the energy was found to have a $t^{-1}$ dependence consistent with RM and MVW. The authors note that their simulations are strictly two-dimensional and that laboratory experiments are inherently three-dimensional which could account for the lower amount of energy lost ($\approx$ 80%) as compared to RM ($\approx$ 90%).

Sullivan et al. (2004) created a stochastic model of oceanic breaking waves which was evaluated through the use of direct numerical simulations (DNS). The Navier-Stokes equations were modified with an additional body force that represents the local acceleration of the fluid due to breaking. The forcing was empirically defined and based on the laboratory results of RM and MVW. The simulations were run with breaking accounting for varying fractions of the total momentum flux across the surface. The remaining fraction was due to viscous stresses. It was found that a small fraction of active breaking caused significant turbulent mixing and vertical transport of horizontal momentum. Additionally, the evolution timescale of the turbulence from a single breaking event was found to be large compared to the duration of active breaking.

An improved knowledge of the breaking at the ocean surface requires a detailed understanding of the kinematics and dynamics of individual breakers as well as measurements of the statistics of breaking. While the statistics can only be measured in the field, detailed studies of the kinematics and dynamics can be carried out in the laboratory.

The laboratory presents a controlled environment in which highly repeatable breaking events can be generated. The ability to measure the turbulence at a number of scales simultaneously is of importance both in the validation of numerical simulations but more importantly in understanding the role turbulence plays in breaking-wave dynamics. Advances in camera and computer technology even since the recent work of MVW, now permit DPIV measurements with improved dynamic range in the wavenumber domain and with much larger data sets.

We have revisited the experiments of RM and MVW using a high-resolution digital camera to permit a wide range of scales to be measured simultaneously and a large number of events in each ensemble to provide improved separation between the mean and turbulent fields while minimizing errors in higher-order turbulent statistics. The resultant data set will permit the measurement of ensemble averaged quantities, wavenumber spectra, the structure of the turbulence, and the ability to compute most terms in the turbulent kinetic energy budget.

In section IV.2 we describe the experimental setup. We present ensemble-averaged flow variables in section IV.3, measurements of turbulent lengthscales in section IV.4, wavenumber spectra in section IV.5, and terms in the turbulent kinetic energy budget in section IV.6. In section IV.7 we discuss some of the implications of these results.

## IV.2 Experimental setup

### IV.2.A Breaking-wave generation

The experiments were carried out in the glass wave channel in the Hydraulics Laboratory at the Scripps Institution of Oceanography. The tank is shown in figure IV.1 and is 0.5 m wide, 1 m deep, and 30 m long. The tank was filled to a working depth of

0.6 m with fresh water. A beach of 6° slope at the far end of the tank is coated with a thick fibrous mat to help dissipate wave energy.

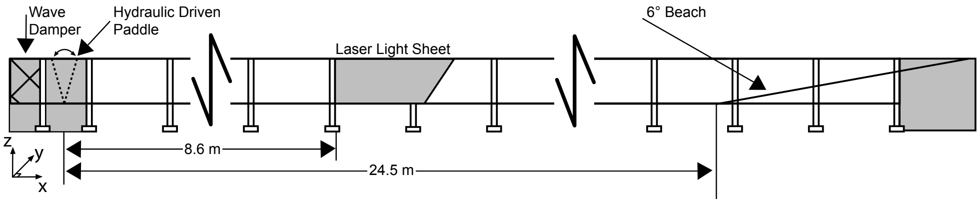

Figure IV.1: The glass channel used for the experiments. DPIV was performed in a window approximately 8.6 m from the wave paddle.

Breaking waves were generated using the dispersive focusing method first proposed by Longuet-Higgins (1974) and exploited by RM. A given wave packet has 32 separate frequency components spread across a normalized bandwidth of $\Delta f/f_c$ centered at a frequency of $f_c$. The theoretical surface elevation at $(x,t)$ is given by

$$\eta(x,t) = \sum_{n=1}^{N} a_n \cos[k_n(x-x_b) - 2\pi f_n(t-t_b)] \tag{IV.2}$$

where $a_n$, $k_n$, and $f_n$ are the amplitude, wavenumber, and frequency of the $n$th component and $(x_b, t_b)$ the theoretical location and time of breaking. The phase of each component is determined by $(x_b, t_b)$ using

$$\cos(k_n x_b - 2\pi f_n t_b - \phi_n) = 1. \tag{IV.3}$$

Following Loewen and Melville (1991) we assigned a constant slope to each component of the wave packet rather than the constant amplitude formulation of RM.

The center frequency of the wave packet was $f_c = 1.08\,\mathrm{Hz}$, the non-dimensional bandwidth was $\Delta f/f_c = 0.75$, and the non-dimensional distance to breaking was $x_b k_c = 40.50$. The non-dimensional time of breaking was $\sigma_c t_b = 118.9$, where $\sigma_c = 2\pi f_c$. The wave generated was a plunging wave with an input slope of $S = 0.36$ given by $S = \sum a_n k_n$. The input slope, $S$, is a measure of the maximum slope predicted by linear theory. The need to generate a turbulent cloud that stayed within the measurement region for approximately 60 wave periods motivated this choice of parameters. In

Chapter III a series of experiments designed to measure the dissipation rate of breaking surface waves over a large range of parameter space is described. Details of the measurement of quantities related to the bulk properties of the flow, potential energy, energy fluxes, and dissipation rates are provided there.

The packet generation is synchronized to the start of the DPIV recording system and upon start the entire system is quiescent for 10 s. This allows for calculation and removal of any DC offsets in the analog instrumentation. A series of wave gauges were used to measure the surface elevation both up- and down-stream of the breaking location. The variation in amplitude and phase of the signal at the farthest upstream and downstream gauges was less than 1.5 mm and 1 ms over the course of the experimental runs. Description of the wave gauges used are provided in III.3.

## IV.2.B Digital Particle Image Velocimetry (DPIV)

The experiments described here were conducted within a window starting 8.6 m from the wave paddle. We have conducted two sets of experiments in the longitudinal plane ($x-z$), the first of these was designed to directly image the largest scales of the flow. A second set of experiments investigated the effects of increasing resolution on measurement of the turbulent fields, through the use of four overlapping windows. Measurements of the velocity field in the transverse ($y-z$) plane were conducted at four locations in order to quantify the cross-stream structure of the flow as well as provide measurements of $(u, v, w)$ at the intersection of the longitudinal and transverse planes.

### The Longitudinal Plane

Measurements were first performed in the longitudinal plane within a window 3.11 m wide. A 200mJ Nd:YAG laser (New-Wave Gemini) was used to illuminate a region of the tank approximately 2 m along the top and 0.6 m deep along the centerline of the tank. The light sheet, introduced from below the tank, was redirected to the vertical plane via a front-surface mirror. The beam optics used have a 60° spreading angle and the mirror was inclined at 30° from the horizontal to create a trapezoidal slice (see figure IV.2). The thickness of the sheet varied from 3 mm at the bottom of the tank to 6 mm at the surface. This thickness was necessary to ensure that particles stayed within the sheet between given laser pulse pairs. The inside of the far wall of the channel was painted flat black within the DPIV test section to prevent any reflections back to the camera.

We used a 3 fps 4024 x 2560 CCD camera (VDS Vosskühler CCD-11000) with a 50mm f1.4 lens. The long axis of the CCD was aligned in the $x$ direction and the aspect ratio of the sensor required cropping of the image prior to processing. The camera was placed slightly below the mean water level and was angled upwards slightly to ensure that the intersection between the light sheet and the free surface was recorded. The final measurement area was 1.88 m x 0.69 m with a resolution of 0.50 mm/pixel. Laser timing/triggering, image recording, and image processing was performed through a commercially available DPIV software package, PixelFlow from VioSense corporation.

There was a delay of approximately 10 minutes between experiments during which time the images were written to disk and the residual turbulence decayed. It was found this interval provided sufficient time to allow surface motions to die out. See appendix A.

Optical calibration of the images was performed using a large plexiglass sheet which was placed in the laser light sheet. Two rows of 2 mm diameter holes spaced 10 cm horizontally across the field of view permitted the conversion from pixels to meters. The spacing also allowed for rectification of the images to account for any distortion caused by perspective or refraction at either the air-glass or glass-water interface. The laser beam has a Gaussian intensity profile and when spread across such a large region there were observable variations in the light sheet intensity. In order to remove this non-constant background intensity the images were first low-pass filtered using a 7x7 averaging window. This filtered image was then subtracted from the original image to create a high-passed image with the low-frequency variability removed. This method is similar to the image pre-processing technique used by Willert (1997) without the subsequent binarization of the image.

The large-scale longitudinal measurements were initially conducted using 41 repeats with a $\Delta t = 20ms$. Upon analysis of the data evidence of peak-locking in the velocity data was seen for $(t - t_b)/T \geq 3.42$. Peak-locking refers to the tendency of integer displacements of particle and can be a source of bias error (Raffel, Willert, and Kompenhans, 1998; Chang and Liu, 2000; Christensen, 2004). A second set of runs with 32 repeats with $\Delta t$ = 30ms and a larger particle image (achieved by slightly defocusing the camera) was conducted in an attempt to reduce the peak-locking. The peak-locking was still present after the second set of experiments, but was eventually found to be not significant within the turbulent cloud. Further details will be provided in section IV.2.B. The two datasets were combined to nearly double the size of the ensemble in the longitudinal plane to 73 repeats. The change in $\Delta t$ had no significant effect on the measured velocity fields over the two days. The large number of repeats helps to reduce random error in the turbulent statistics, but additionally provides guidance for the number of ensembles necessary to achieve convergence of the statistics. Silver-coated hollow ceramic spheres with a mean diameter of 100$\mu$m and a mean density of $\rho = 1.01\text{g cm}^{-3}$ were used as seeding material (Potter Industries, AG-SL150-30-TRD). Prior to seeding the fluid, the particles were first washed with a common household dishwasher rinse-aid (Jet-Dry) and then flushed with water for 10 minutes to remove any trace of the rinsing agent. Between runs the measurement region was mixed in order to maintain a uniform particle distribution within the fluid from run to run.

Melville et al. (2002) showed that within the most energetic region of the breaking 15 repeats of the velocity and turbulent kinetic energy density fields were needed to be within 2% and 16% of the full-ensemble field (as calculated from 24 repeats). While the mean velocity field is well resolved with 15 repeats more data is needed to investigate higher order statistics. Increasing the number of repeats can be quite costly due to the length of time for each individual run. This fact is compounded when multiple windows are used as was the case in MVW. In the experiments described here the full field is captured in one image pair so we can extend the number of repeats with only a small increase in experimental time. The normalized error in the squared magnitude of the velocity at the $N$th repeat relative to the $N = 73$ ensemble is given by

$$\delta u_N^2 = \sum_{ij} \frac{|u_N - u_{73}|^2}{|u_{73}|^2}. \tag{IV.4}$$

The normalized error of second order and third order quantities at the $N$th repeat relative to the $N = 73$ ensemble are given by

$$\delta Q_N = \sum_{ij} \frac{|Q_N - Q_{73}|}{|Q_{73}|} \tag{IV.5}$$

where $Q$ is either $\langle u_i u_i \rangle$ or $\left\langle u_i u_i u_j \right\rangle$.

The magnitude of the error for small $N$ is dependent on the order in which the repeats are arranged, since for example the normalized error using repeats 1-4 is not equal to the normalized error using repeats 5-8. To overcome this, a random permutation of the ensembles was used to compute $\delta u_N^2, \delta q_N$, and $\delta u q_N$. The same permutation of ensembles was used for each estimate. This was repeated ten times and the mean along with the maximum and minimum over those ten permutations for a given $N$ is shown in figure IV.3.

The rate at which these terms converge is found by taking $d/dN$ and the derivative of the mean normalized error over the ten permutations can be seen in figure IV.4. The normalized mean velocity magnitude and the normalized turbulent kinetic energy density converge quite rapidly for $N < 10$ and then slowly approach the value at $N = 73$. The rate of convergence for the normalized third-order correlation term is initially large but begins to level out after $N = 20$, the rate of convergence is then nearly constant.

### Mosaic DPIV in the longitudinal plane

While these full-field measurements provide a large dynamic range in terms of the scales that can be measured, we are still limited in the resolution. We extended the resolution of the measurements using a technique similar to that used by MVW. A mosaic of measurements were taken with four overlapping images in the $x$-direction, with an increase in resolution by a factor of 2.5 to 0.19 mm/pixel. The resultant size of the each image was approximately 0.49 m x 0.76 m. The camera was mounted on a linear track which was placed parallel to the tank, with the long axis of the camera sensor orientated in the $z$ direction. The camera was placed below the mean water level and was angled slightly to ensure that the intersection of the free surface with the light sheet was captured. A new calibration grid with lines etched at 5 cm interval was used to ensure proper rectification of the images from any induced perspective error.

During data collection, the laser sheet was used to illuminate the entire 2 m x 0.6 m region described previously. This was to ensure that all measurements would be taken along the same longitudinal section in the transverse plane. Upon analyzing the results it was found that the measurements taken within the fourth window exhibited more noise than the previous windows for a given run. However it is found that the turbulent cloud does not enter the fourth window for $(t - t_b)/T < 12.78$. We will thus restrict our analysis of the mosaic DPIV to the first three windows.

The $\Delta t$ was kept fixed at 30ms, but 14$\mu$m silver coated hollow glass spheres were used as seeding material as the increased resolution required smaller seeding particles (Potters Industries, SH400S33). The original intent was to conduct 40 repeats of the experiment. The fact that 73 repeats were conducted allows for an estimate of the normalized errors in the mosaic DPIV. A total of 38 repeats was collected for each window, which has 0.6% of the velocity, 11% of the TKE density, and 65% of the third-order correlations when referred to the ensemble average using all 73 repeats, see figure IV.3 and (IV.4, IV.5). Upon analysis of the image data it was found that a small phase delay was present between the full-field measurement and these windowed measurements. The mosaic measurements were found to be ahead of the full-field measurements by approximately 0.5 s. The measured surface elevations exhibited no significant variation, and it is thought that the delay is brought about by a delay in the laser/camera synchronization. This variation is only seen between the full-field measurements and the mosaic measurements and does not arise from run to run for a given set of experiments. The measured TKE field does not change very rapidly for the values of $(t-t_b)/T$ considered, and there is good agreement between the temporal rates of decay, so the difference in energy values will be slight.

### Transverse plane

Turbulence is inherently three-dimensional but the velocity fields recorded by DPIV are typically two-dimensional. So a series of measurements in the transverse plane was conducted at four locations, $x$ = [8.98, 9.22, 9.42, 9.91]m, which correspond to $(x - x_b)/\lambda$ = [0.39, 0.57, 0.73, 1.09].

To create the cross-stream light sheet the head of the laser was orientated in a vertical plane (see figure IV.5). The light sheet thickness was 4 mm and $\Delta t = 30$ms which was short enough to ensure that particles are not advected out of the plane during the measurement by the mean flow not associated with surface waves. Difficulties arise due to the out-of-plane velocity component being larger than both in-plane components, thus the size of $\Delta t$ is ultimately determined by $u$. The surface-wave-induced velocities can be large enough to cause large out of plane motions. For the times after breaking considered here, this was only an issue for location 4 at $(t-t_b)/T) = 3.42, 5.58$. Calibration of the system was accomplished using the same grid as in the mosaic DPIV.

A megapixel camera (Uniq UP1830) was enclosed in a watertight housing and placed 1.27 m downstream of the light sheet. Due to hardware restrictions the camera was run at a frame rate of 24 Hz. A 12.5 mm f1.8 lens was used and the camera was angled up slightly to ensure that the surface was within the field of view. Image capture was synchronized to the start of the paddle and data was collected for 90 s, yielding 1080 image pairs. In order to obtain as high a resolution as possible while imaging the entire width of the tank, the entire depth of the tank could not be imaged at once. With the aspect ratio of the image sensor being square the maximum depth covered was approximately 0.45 m below the mean water level, which is deeper than the depth to which particles are mixed down by breaking, see figure IV.6. The final size of the images was approximately 0.51 m square with a resolution of 0.5 mm/pixel. A minimum of 37 repeats were collected with normalized errors of 0.7% for the mean velocity field, 11% for the turbulent kinetic energy, and 67% for the turbulent energy flux.

### DPIV Processing

Before any processing of the windows was performed, each image was corrected for any distortion induced by perspective or refraction. A projective transformation was found to be sufficient for both the full-field and cross-stream measurements. Due to the camera angle used in the mosaic DPIV, a 3rd order polynomial transformation was applied.

Processing of the rectified image pairs was done using a multi-window method similar to the DPIV Extended (DPIVE) described by MVW. The method starts with a window of 32x32 pixels to obtain a low resolution measurement of the flow. Subsequent passes are made with smaller windows (16x16, 50% overlap) which are pre-shifted by the coarse vector field found in the preceeding step. Between each step the velocity field is corrected for outliers and the final velocity field is smoothed with a 3x3 median filter before converting to laboratory coordinates. All sub-pixel interpolation is done using 3 point Gaussian interpolation.

Determination of the surface profile is a simple matter when applied to an ensemble-averaged image. The interface between the laser sheet and the water surface has the brightest average return, and the free surface is simply the brightest point in each column, see figure IV.6. The subsequent profile is then smoothed using a 32 pixel running mean filter. After processing has been performed, the values above the free surface are set to zero. Due to the configuration of the light sheet, non-illuminated regions in both the longitudinal and transverse planes exist. The vectors within these regions are also set to zero.

When dealing with a large field of view, difficulties arise in finding particles with an optimum size distribution and density. If the particles are too small for the sub-pixel estimator, then peak locking can result (Raffel et al., 1998), in which the particle displacement is biased towards an integer value. The amount of peak-locking is dependent on the sub-pixel estimator and the particle image diameter, that is the size of the particle in the image. The cause of this peak-locking is the inability of the chosen sub-pixel estimator to accurately resolve the peak of the cross-correlation.

Chang and Liu (2000) found bias errors which were as large as the turbulent intensities, and thus called it “psuedo-turbulence”. They attributed the cause of this “psuedo-turbulence” in their data to a bias error similar to this peak-locking effect. The resolution of our large scale measurements in the longitudinal plane is lower than that of Chang and Liu (2000) however we have larger seeding particles and a longer $\Delta t$, which would help to reduce this error.

As mentioned previously existence of pseudo-turbulence or peak-locking in our measurements of the TKE field can be seen. Inspection of the velocity field showed that the peak-locking only occurred outside of the turbulent cloud and did not affect our measurements of the turbulence. This is due to small particle displacements caused by noise. Additionally the intensity of the pseudo-turbulence outside of the cloud is an order of magnitude smaller than the TKE intensity within the cloud, which contrasts with the findings of Chang and Liu (2000). Thus the bias error introduced by the peak-locking does not affect our measurements. When presenting any averaged quantities, the data will be windowed to only include the the spatial extent of the turbulent cloud. The locations of these extremes can be seen in figure IV.16 as solid vertical white lines.

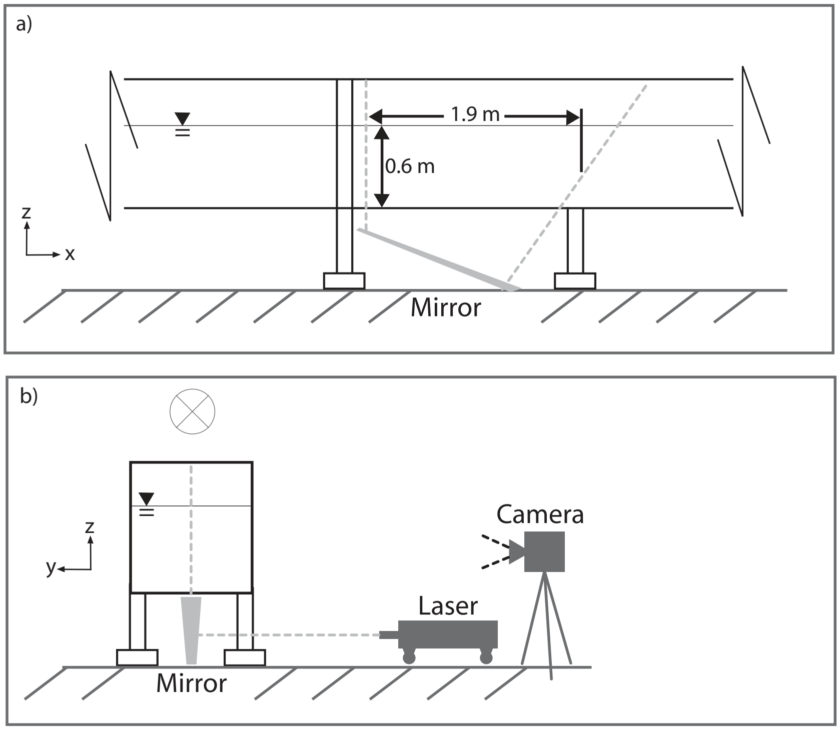

Figure IV.2: Schematic showing the setup of the longitudinal DPIV measurements in a window 8.6 m from the wave paddle. In a) the extent of the laser sheet imaged is shown and is 0.6 m x 1.9 m. b) shows the location of the laser head and the camera relative to the wave tank. The wave is propagating into the plane of the paper in this view. The laser sheet enters from the bottom of the tank and creates a sheet 6 mm thick along the centerline of the tank.

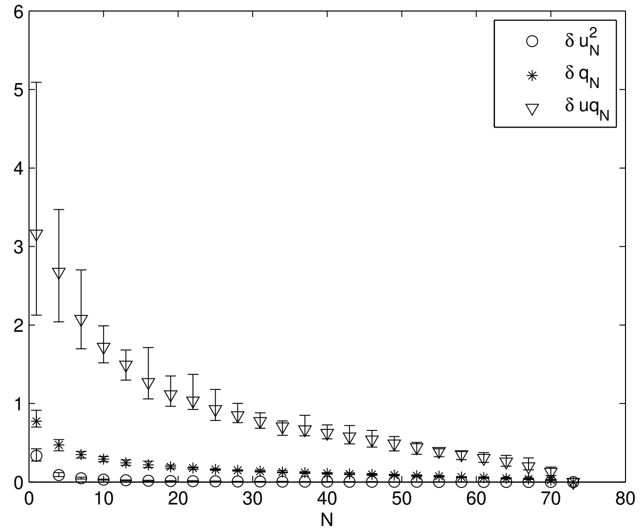

Figure IV.3: Convergence of the normalized mean velocity magnitude (∘), normalized turbulent kinetic energy density (∗), and the normalized third-order correlation $\langle u_j u_i u_i \rangle$ (▽). The error bars denote the maximum and minimum values of the normalized error for ten permutations of the ensembles and the symbols represent the mean of those ten permutations.

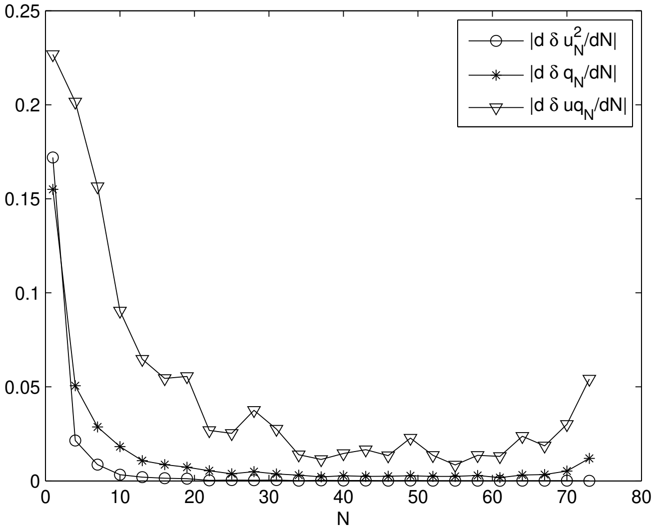

Figure IV.4: The magnitude of the rate of convergence of the mean normalized error, $\left|d/dN\left(\delta u_N^2\right)\right|$ ($\circ$), $|d/dN\,(\delta q_N)|$ ($*$), and $|d/dN\,(\delta q u_N)|$ ($\triangledown$). The normalized mean velocity and turbulent kinetic energy converge quite rapidly, while the convergence rate evolves more slowly for the normalized third-order correlation, $\langle u_j u_i u_i\rangle$.

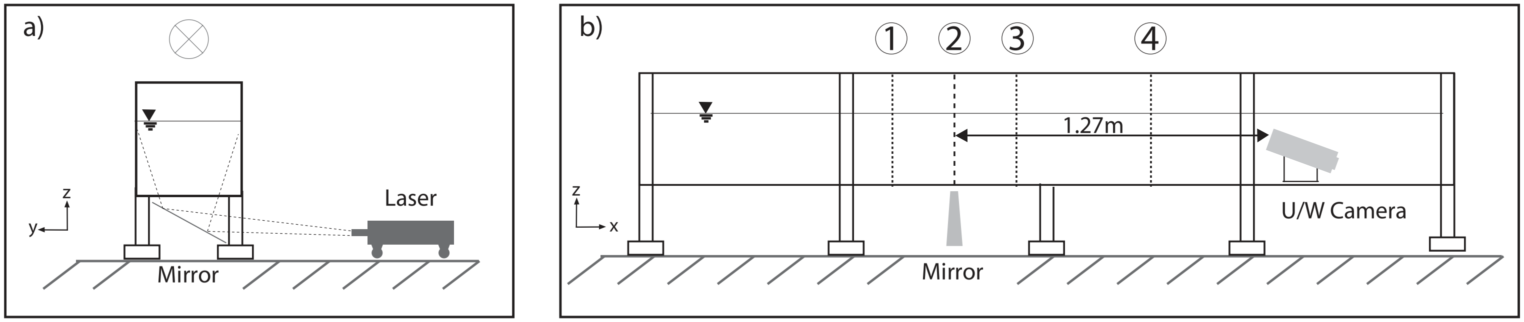

Figure IV.5: Schematic showing the setup of the laser light sheet and camera system for measurements in the transverse plane. The numbers refer to the various locations at which measurements were taken. The distance between the camera and the light sheet remained fixed however.

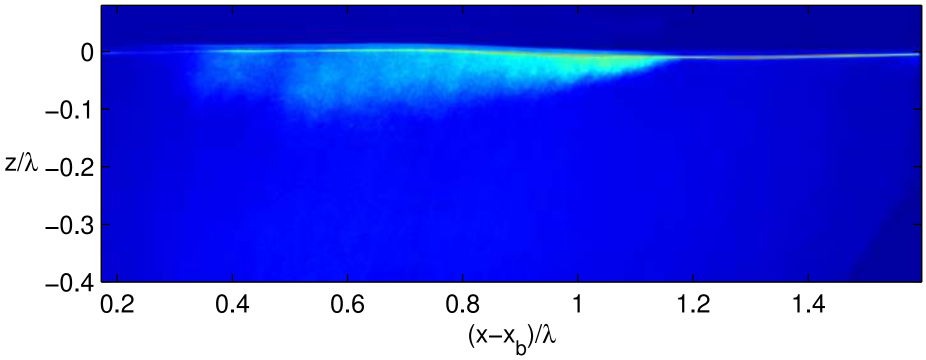

Figure IV.6: False color ensemble averaged image (N=41) at $(t - t_b)/T = 5.58$. The bright region near the surface is due to particles which have been mixed down by the breaking. The faint line above the water surface is the intersection of the free surface with the near wall of the tank.

### IV.2.C Ensemble-averaged momentum and energy equations

For an incompressible Newtonian fluid, the equations of motion are the Navier-Stokes equations defined as

$$\frac{\partial \tilde{u}_i}{\partial t} + \tilde{u}_j \frac{\partial \tilde{u}_i}{\partial x_j} = -\frac{1}{\rho}\frac{\partial \tilde{p}}{\partial x_i} + \nu \frac{\partial^2 \tilde{u}_i}{\partial x_j \partial x_j} \tag{IV.6}$$

where $\rho$ is the density, $\nu$ the kinematic viscosity, and $\tilde{p}$ is the instantaneous modified pressure, $\tilde{p} = p - \rho g_i$. The ensemble average will be denoted by angle brackets. In order to separate the mean quantities from the turbulence a Reynolds decomposition will be applied where $\tilde{u} = \langle u \rangle + u$, with $\langle u \rangle$ denoting the mean and $u$ the turbulence. The mean momentum equation is found by ensemble averaging (IV.6) which yields,

$$\frac{\partial U_i}{\partial t} + U_j \frac{\partial U_i}{\partial x_j} = -\frac{1}{\rho}\frac{\partial \langle p \rangle}{\partial x_i} + \nu \frac{\partial^2 U_i}{\partial x_j \partial x_j} - \frac{\partial}{\partial x_j}\langle u_i u_j \rangle \tag{IV.7}$$

where $U_i = \langle u_i \rangle$. The term $\langle u_i u_j \rangle$ is known as the Reynolds stress and describes the transfer of mean momentum by the turbulence. If we define a stress

$$\langle \tau_{ij} \rangle = -\langle P \rangle \delta_{ij} + 2\mu S_{ij} - \rho \langle u_i u_j \rangle \tag{IV.8}$$

where $\delta_{ij}$ is the Kronecker delta and $S_{ij}$ is the mean strain rate,

$$S_{ij} = \frac{1}{2}\left(\frac{\partial U_i}{\partial x_j} + \frac{\partial U_j}{\partial, x_i}\right) \tag{IV.9}$$

then (IV.7) becomes

$$\frac{\partial U_i}{\partial t} + U_j \frac{\partial U_i}{\partial x_j} = \frac{1}{\rho}\frac{\partial \langle \tau_{ij} \rangle}{\partial x_j}. \tag{IV.10}$$

The kinetic energy of the mean flow is found by multiplying (IV.10) by $U_i$ (Tennekes and Lumley, 1972),

$$\begin{aligned} \frac{\partial}{\partial t}\left(\frac{1}{2}U_i U_i\right) + U_j \frac{\partial}{\partial_x}\left(\frac{1}{2}U_i U_i\right) &= \frac{\partial}{\partial x_j}\left(-\frac{\langle P \rangle U_j}{\rho} - 2\nu U_i S_{ij} + \langle u_i u_j \rangle U_i\right) \\ &- 2\nu S_{ij} S_{ij} + \langle u_i u_j \rangle S_{ij} \end{aligned} \tag{IV.11}$$

The first three terms on the right-hand side are transport terms which only serve to redistribute the mean kinetic energy within a given volume. The fourth term is viscous dissipation due to the mean strain rate, which is negligible for large Reynolds numbers along with $2\nu U_i S_{ij}$. The last term on the right-hand side represents the exchange of energy between the mean flow and the turbulence. An analogous term arises in the TKE budget but with opposite sign, so a loss from the mean field is a gain to the turbulence and vice-versa. Thus this term is known as the production.

The kinetic energy of the turbulence can be computed by multiplying (IV.6) by $\tilde{u}$ and ensemble-averaging and then subtracting (IV.11). The end result is the turbulent kinetic energy equation,

$$\begin{aligned}\frac{\partial}{\partial t}\left(\frac{1}{2}\langle u_i u_i\rangle\right) + \langle u_j\rangle\frac{\partial}{\partial x_j}\left(\frac{1}{2}\langle u_i u_i\rangle\right) &= -\frac{\partial}{\partial x_j}\left(\frac{1}{\rho}\left\langle u_j p\right\rangle + \frac{1}{2}\left\langle u_i u_i u_j\right\rangle - 2\nu\left\langle u_i s_{ij}\right\rangle\right) \\ -\left\langle u_i u_j\right\rangle S_{ij} \quad & -2\nu\left\langle s_{ij} s_{ij}\right\rangle . \end{aligned} \tag{IV.12}$$

Here $s_{ij}$ is the fluctuating rate of strain,

$$s_{ij} = \frac{1}{2}\left(\frac{\partial u_i}{\partial x_j} + \frac{\partial u_i}{\partial x_j}\right). \tag{IV.13}$$

As mentioned earlier the fourth term on the right-hand side of (IV.12) is the production and plays the opposite role of the same term in (IV.11), i.e. when one is a sink the other is a source. It is this term which links the mean and the turbulent fields to one another. The dissipation term here, $2\nu s_{ij} s_{ij}$ is not negligible and accounts for the ultimate dissipation of energy into heat through the action of viscosity.

## IV.3 Ensemble-averaged flow quantities

Unless otherwise stated all quantities will be normalized using the characteristic center wavelength, $\lambda_c$, period, $T_c$, and phase speed, $C_c$ of the wave packet. The center component refers to the quantity associated with the center frequency of the wave packet, $f_c$. The non-dimensional distance downstream of the break point and elapsed time since breaking are defined as

$$x^* = (x - x_b)/\lambda \tag{IV.14}$$

$$t^* = (t - t_b)/T \tag{IV.15}$$

For the measurements that follow, the turbulence will be computed using a Reynolds decomposition of the velocity field with mean quantities determined by an ensemble average, denoted by angle brackets. The instantaneous field will be denoted by $\tilde{u} = \langle u \rangle + u$. In the longitudinal plane the origin in the vertical direction is at the quiescent free surface while the origin of $y$ in the transverse plane is the slice in which the streamwise measurements were taken.

## IV.3.A Mean Velocity and Vorticity

### Longitudinal plane

Figure IV.7 shows the mean velocity field from 5 to 58 wave periods after breaking in the longitudinal plane. All subsequent ensemble averaged quantities are shown for the same values of $t^*$. At a time of 3.42 wave periods after breaking the surface waves passing through the measurement region clearly dominate the wave field. At $t^* = 12.78$ there is still evidence of surface waves but a clearly defined vortex has formed at approximately $x^* = 0.6$. As noted by MVW this feature grows in time and slowly propagates downstream under the influence of its image vortex above the surface. We can also see residual surface waves in the tank at 50.22 and 58.9 wave periods after breaking with a frequency of $f \simeq 1.8 - 2$ Hz $> f_{32}$, where $f_{32}$ is the highest frequency component in the packet. These are consistent with a series of high-frequency waves generated by the breaking event that have propagated down the tank and are currently propagating downstream through the measurement window. Figure IV.8 shows the magnitude of the mean velocity field superimposed with the flow streamlines. Assuming the flow to be incompressible and two-dimensional the streamlines can be computed using

$$\Psi = \int (u\,\mathrm{d}y - v\,\mathrm{d}x)\,. \tag{IV.16}$$

The contours of $\Psi$ clearly show a well defined coherent vortex at $t^* = 12.78$. The mean vorticity of the flow is shown in figure IV.9. The vorticity is computed by calculating the circulation around a 3x3 grid divided by the area enclosed. Positive vorticity here corresponds to a counter-clockwise rotation and the large region of negative vorticity seen is consistent with the coherent structure formed. A thin layer of positive vorticity is found at the surface and is possibly an artifact of processing due to the proximity of the free surface.

### Transverse plane

Figure IV.10 shows the mean velocity field in the transverse plane. Distance from the paddle increases to the right and time increases down the figure with the locations of the cross-stream windows at $x^* = [0.39, 0.57, 0.73, 1.09]$. At times while surface waves are still in the tank, the vertical flow induced by the passing waves dominates the flow field. After the waves have propagated out of the region the mean flow exhibits some transverse oscillations at $t^* = 43.02$ for the transverse planes numbered one to four. These near-surface fluctuations are also seen for $t^* = 58.86$ and could be caused by the residual surface waves seen to be propagating within the tank. As the core of the vortex nears the furthest downstream location a downward flow is seen which is consistent with the clockwise rotation of the vortex. The magnitude of the velocity field and the corresponding streamlines are shown in figure IV.11, and do not seem to exhibit any strong gradients in the $y$ direction. This is consistent with a flow which is two-dimensional in the mean.

The vorticity of the flow is shown in figure IV.12. With the exception of some isolated regions near the surface at times close to breaking, the structure can be seen to be predominately noise.

### Removal of surface wave velocities

It is evident that the velocities induced by the surface waves following the breaking event dominate the ensemble averaged post-breaking velocity field at short times. In order to attempt to remove the surface waves we first assume that the ensemble-averaged velocity field can be separated into velocities due to irrotational surface waves and rotational motions generated by the breaking process. Thus we define

$$\langle u \rangle = \langle u_S \rangle + \langle u_B \rangle \tag{IV.17}$$

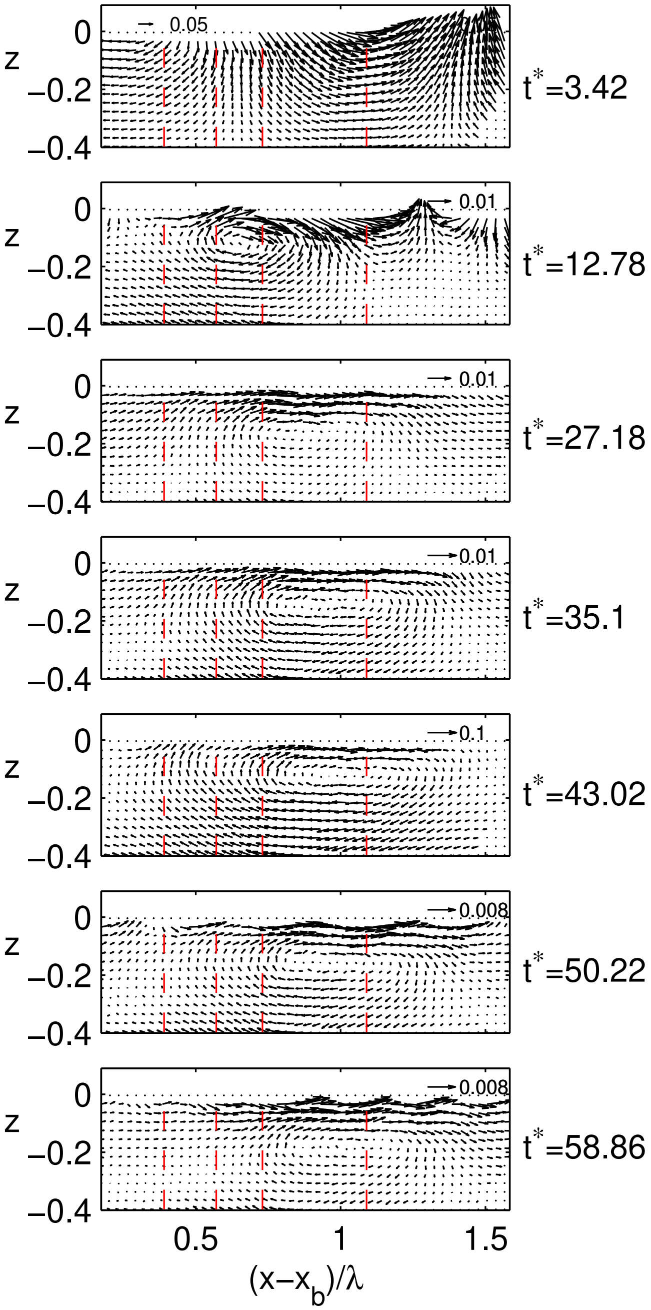

Figure IV.7: The normalized mean velocity field at $t^{*}$=[3.42, 12.78, 27.18, 35.1, 43.02, 50.22, 58.86]. The velocity fields are decimated by a factor of ten in the horizontal direction and by a factor of five in the vertical. The modification of the velocity field by the surface waves is evident up to approximately 12 wave periods after breaking. The vertical lines correspond to the locations of the transverse plane measurements in figure IV.10

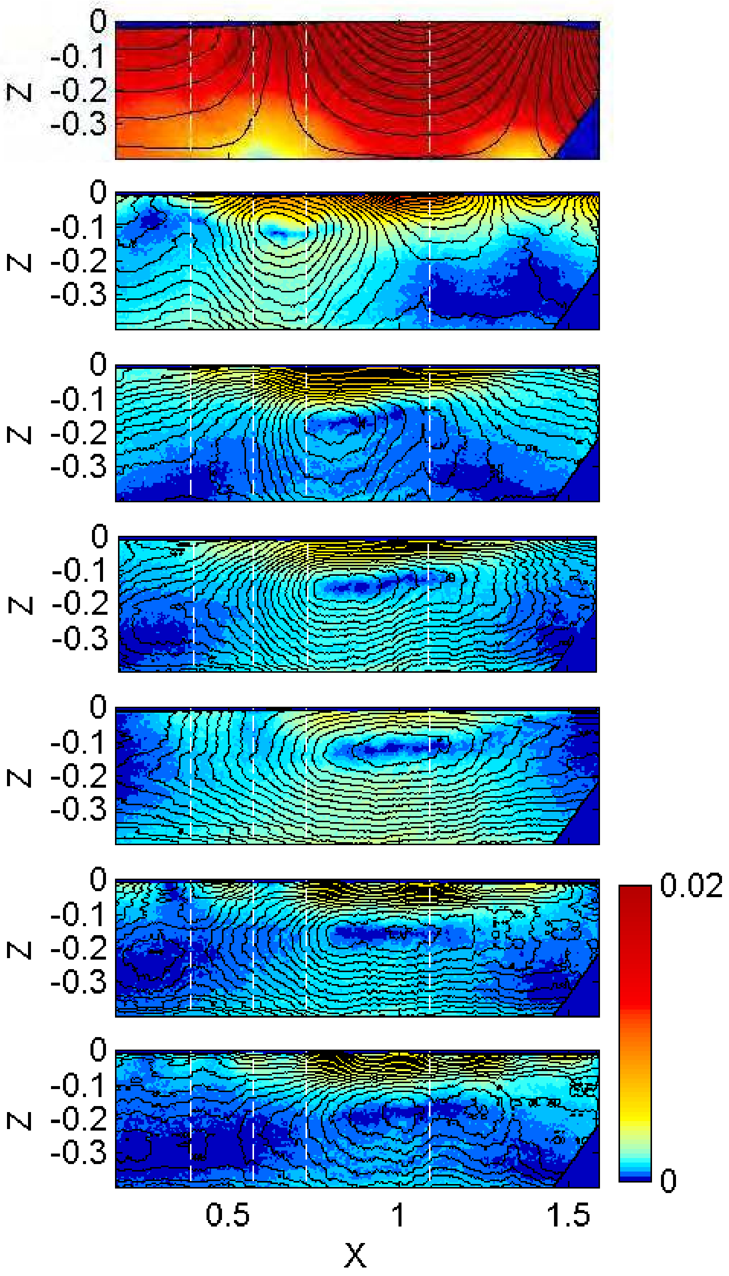

Figure IV.8: The normalized magnitude of the mean velocity field superimposed with the flow streamlines. The coherent vortex generated by the breaking process is clearly seen here after approximately 12 wave periods.

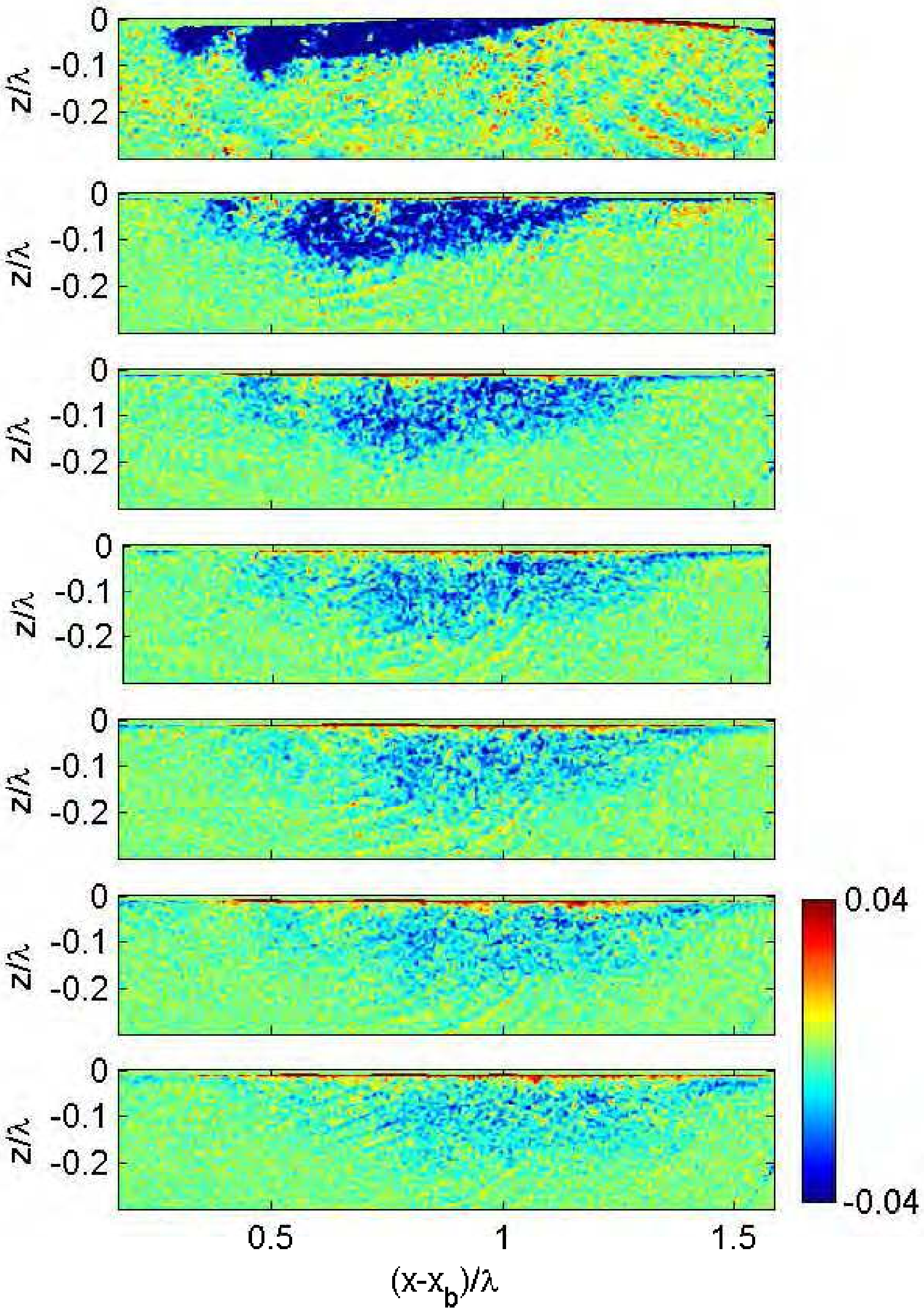

Figure IV.9: The normalized vorticity of the mean flow. The vorticity is mainly negative (corresponding to clockwise rotation) and deepens slowly as the turbulent cloud propagates downstream. The pattern in the background which dominates at $t^* = 3.42$ and less so for later $t^*$ is thought to be related to the streamlines of the flow. See section IV.3.F for further discussion.

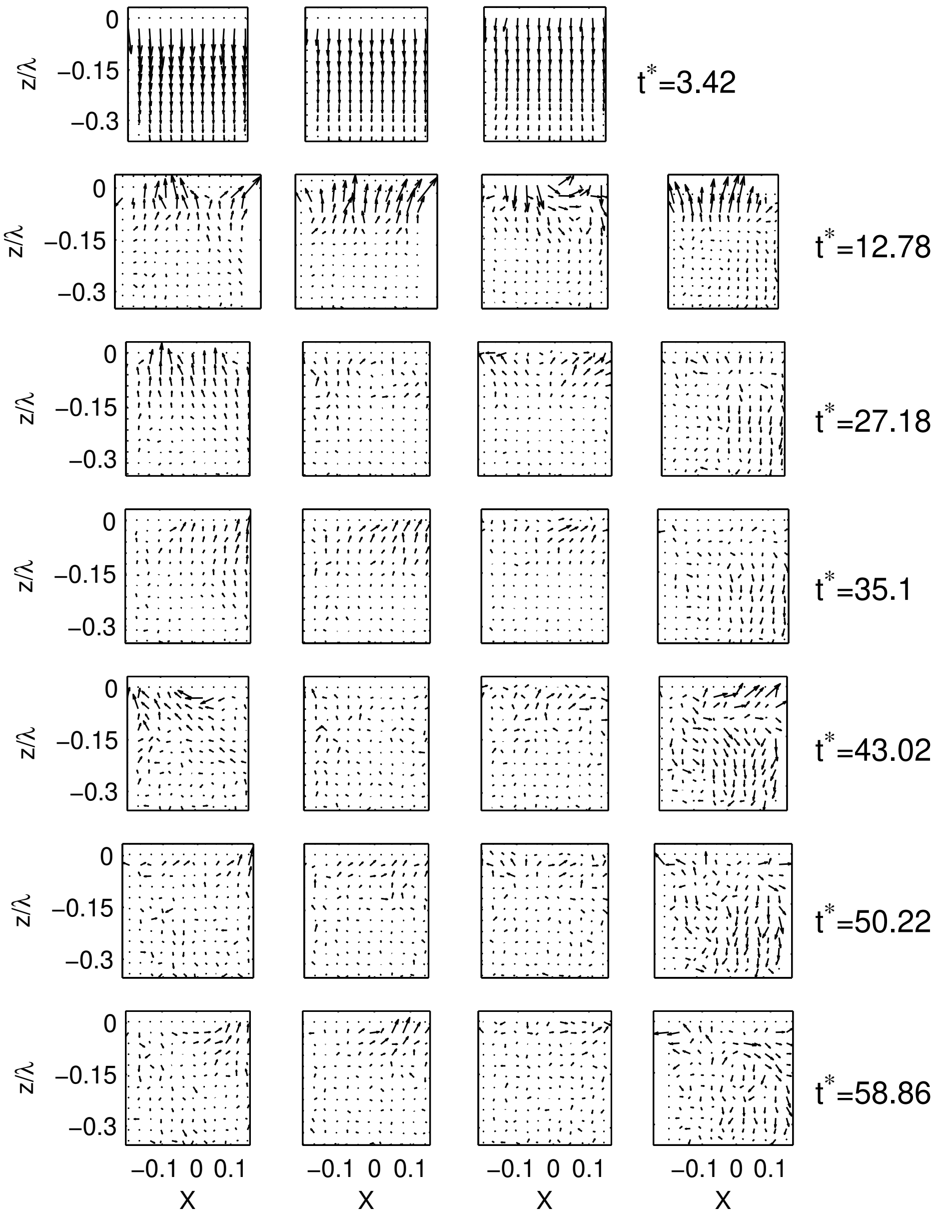

Figure IV.10: The normalized mean velocity field in the transverse plane. The x-location of the window increases from left to right from $x^* = 0.39$ to $x^* = 1.09$. The times after breaking for each horizontal row are the same as in IV.7

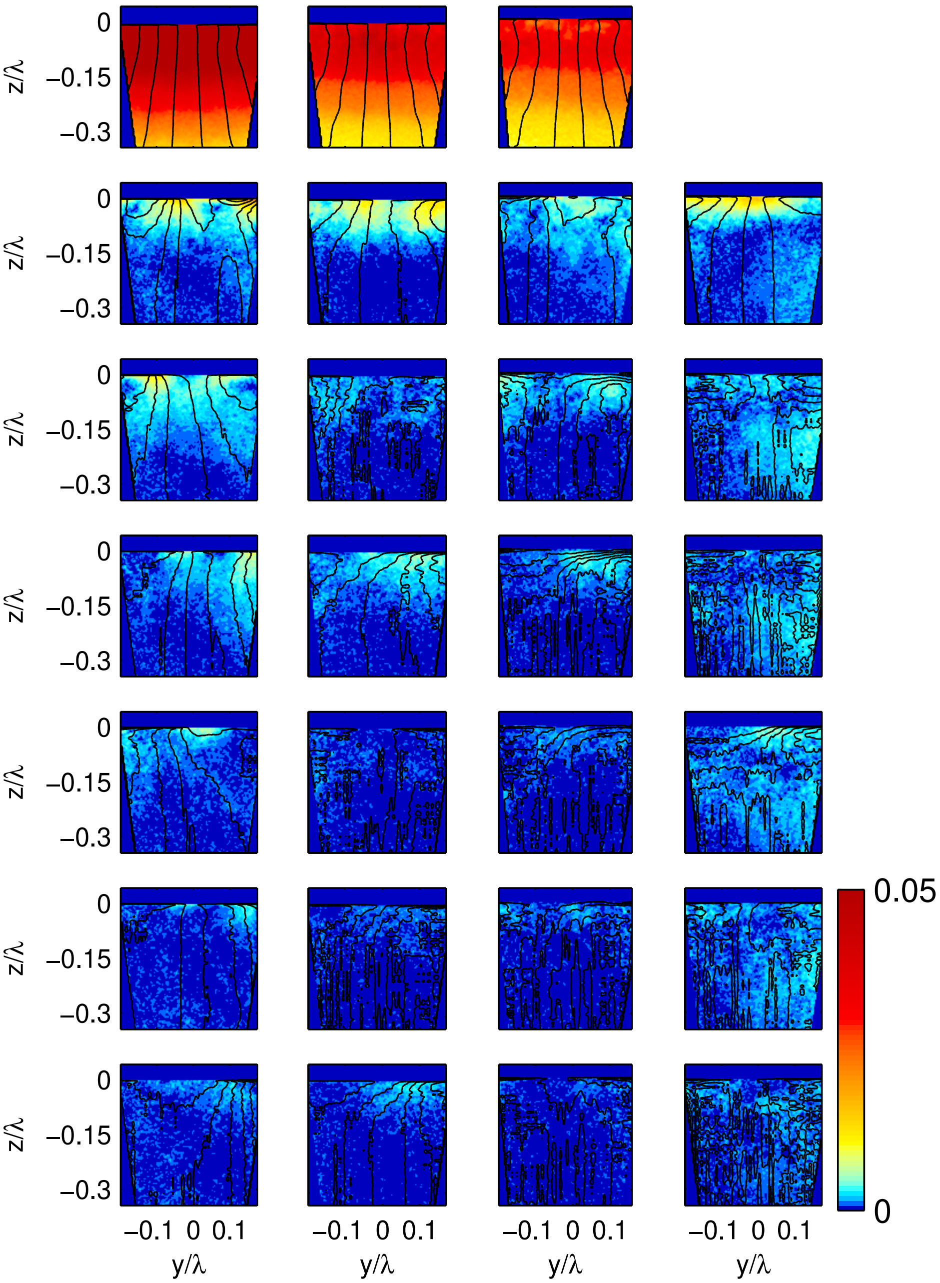

Figure IV.11: The normalized magnitude of the mean velocity field in the transverse plane superimposed with the flow streamlines.

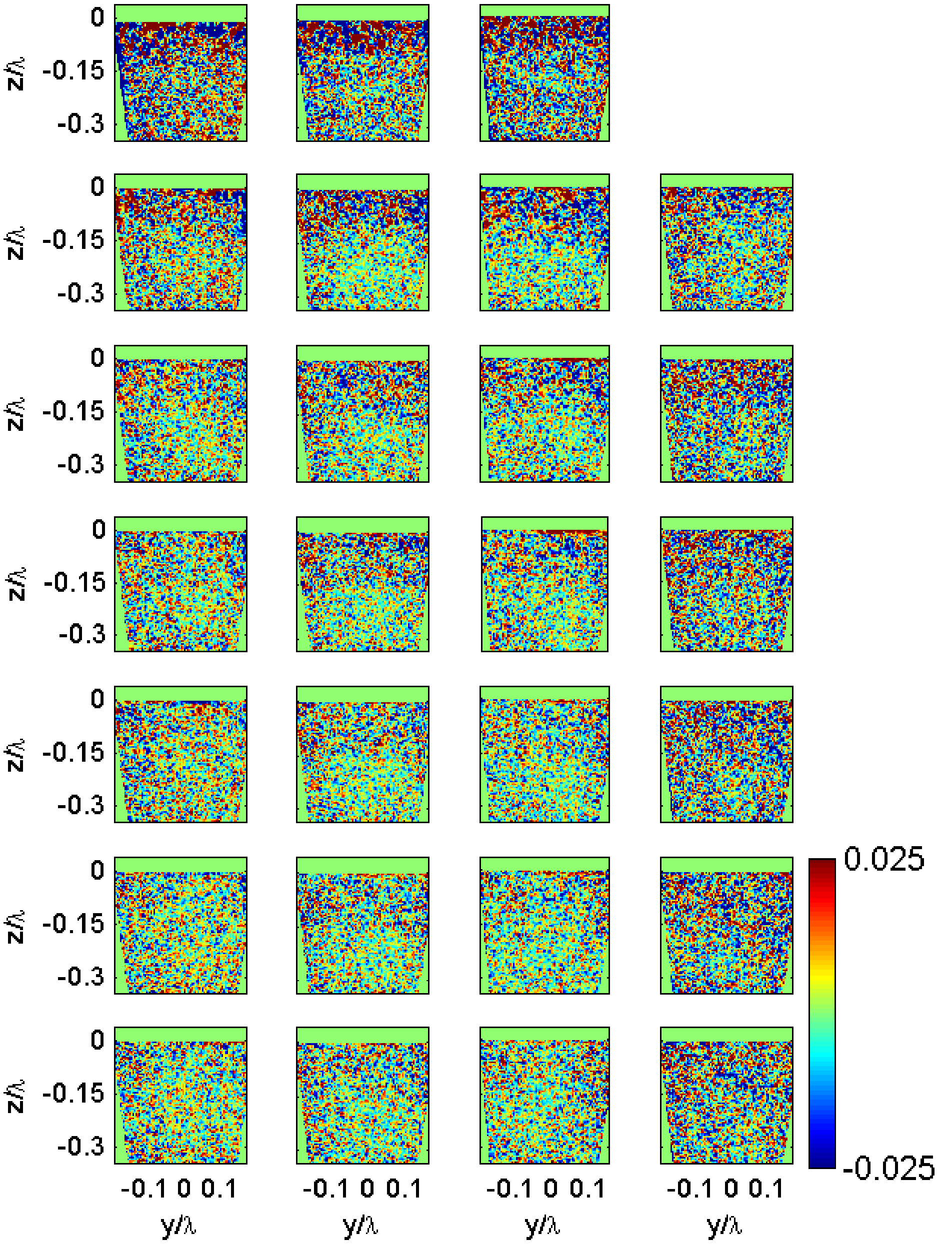

Figure IV.12: The normalized vorticity of the mean flow in the transverse plane. The vorticity is predominately noise.

$$= \quad U_S + U_B \tag{IV.18}$$

where the subscripts $S$ and $B$ refer to velocities from the surface waves and velocities from the breaking event. The surface elevation, $\eta(x,t)$, can be measured from the video imagery for a specific time after breaking. Taking the spatial FFT of the free surface and assuming the waves are propagating in the positive $x$ direction allows us to compute the theoretical $(u,w)$ velocities as predicted by a second order Stoke's wave expansion (Dean and Dalrymple, 1991),

$$\begin{aligned}
u(x,z) &= \sum_n^N a_n\sigma_n \frac{\cosh(k_n(z+H))}{\cosh(k_nH)}\cos(k_nx+\phi_n) \\
&\quad +\frac{3}{4}a_n^2\sigma_nk_n\frac{\cosh(2k_n(z+H))}{\sinh^4(k_nH)}\cos(2(k_nx+\phi_n)) && \text{(IV.19)} \\
w(x,z) &= \sum_n^N a_n\sigma_n \frac{\sinh(k_n(z+H))}{\cosh(k_nH)}\sin(k_nx+\phi_n) \\
&\quad +\frac{3}{4}a_n^2\sigma_nk_n\frac{\sinh(2k_n(z+H))}{\sinh^4(k_nH)}\sin(2(k_nx+\phi_n)) && \text{(IV.20)} \\
& && \text{(IV.21)}
\end{aligned}$$

Here $(a_n, \sigma_n, \phi_n)$ are the amplitude, radial frequency, and phase for a given Fourier component, $k_n$ and $H$ is the water depth. The expressions for $u(x,z)$ and $w(x,z)$ are then subtracted from the ensemble-averaged velocity to produce the residual velocity associated with the breaking event. The magnitude of the residual rotational velocity field is presented along with the corresponding streamlines of the flow in figure IV.13 for both $U_S + U_B$ (IV.13a-IV.13d) and $U_B$ (IV.13e-IV.13h). After the surface-wave induced velocity has been removed the coherent structure can be seen to form within five wave periods of breaking.

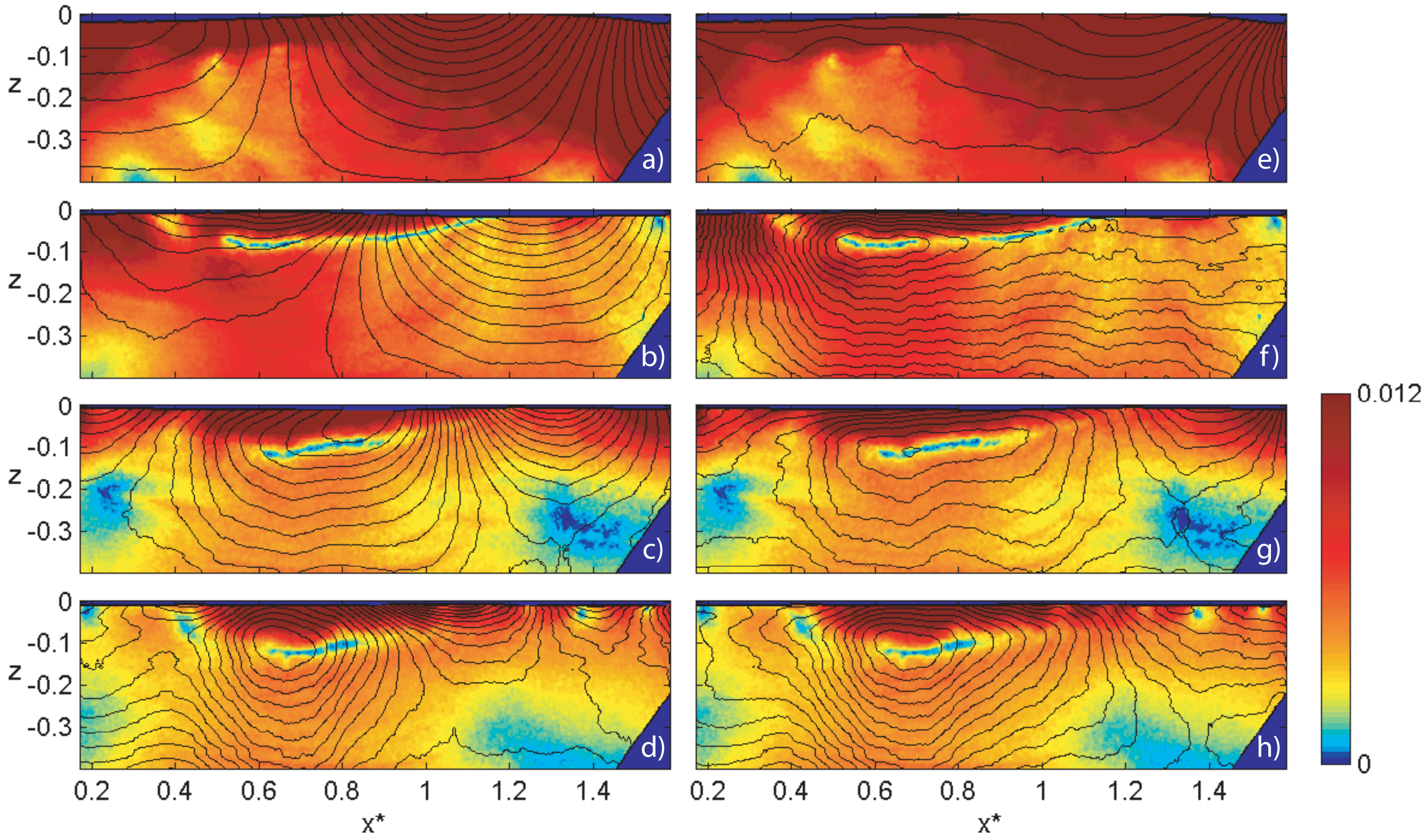

Figure IV.13: The normalized magnitude of the mean velocity field superimposed with the flow streamlines. The images on the left hand side are for the mean velocity field due to the surface waves and breaking, while the images on the right hand side correspond to the mean velocity field caused by breaking only, see (IV.18). Times shown are $t^* = 3.42$ (a) and e)), $t^* = 5.58$ (b) and f)), $t^* = 8.46$ (c) and g)), and $t^* = 12.78$ (d) and h)).

## IV.3.B Kinetic Energy

The mean kinetic energy of the flow is given by

$$\begin{aligned} E &= \frac{1}{2}\left(\left\langle (U_i + u_i)^2 \right\rangle\right) && \text{(IV.22)} \\ &= \frac{1}{2}U_i^2 + \frac{1}{2}\left\langle u_i^2 \right\rangle && \text{(IV.23)} \\ &= E_m + E_t && \text{(IV.24)} \end{aligned}$$

Where $E_m$ and $E_t$ are the kinetic energy densities of the mean flow and the turbulence, respectively.

### Longitudinal plane

The kinetic energy of the mean flow in the longitudinal plane, $\frac{1}{2}\left(\langle u\rangle^2 + \langle w\rangle^2\right)$, is presented in figure IV.14. The initial levels of the kinetic energy are quite large due to the presence of surface waves. A logarithmic color scale is employed in order to try to encompass the entire dynamic range of the kinetic energy. The cloud of kinetic energy is seen to propagate downstream at a rate consistent with the large coherent vortex generated by breaking. The effect of the surface waves on $E_m$ are also seen in figure IV.15, where the technique described in section IV.3.A was used to compute the kinetic energy of the velocity due to breaking only.

The turbulent kinetic energy density in the longitudinal plane,$\frac{1}{2}\left(\left\langle u^2\right\rangle + \left\langle w^2\right\rangle\right)$, is shown in figure IV.16. The averaging procedure removes the coherent surface waves from the velocity field and leaves the incoherent component of the flow. A logarithmic color scale is used again to encompass the large dynamic range of TKE. The cloud reaches a depth of $z \approx -0.12$ at five wave periods after breaking and has a horizontal extent of $\approx 0.83\lambda$. The initial levels of TKE decrease quite rapidly as time progresses. The vertical white lines denote the extent of the limits taken when windowing the data as described in section IV.2.B.

Figure IV.17 shows a comparison between the turbulent kinetic energy density at $t^* = 5.58$ and the corresponding ensemble-averaged image used to compute the velocity field. The outline of the turbulent cloud is delineated by the $TKE = 8.22 \cdot 10^{-5}$

contour, shown in white. This outline of the turbulent cloud is overlaid on the image of the particles mixed down by the breaking event. Two distinct regions can be seen just upstream and downstream of $x^* = 0.4$. The shallower upstream bump corresponds to the initial plunge point of the breaking wave while the downstream region is due to the subsequent splash up (Bonmarin, 1989; Chen et al., 1999).

### Transverse plane

We show measurements of the kinetic energy of the mean flow in the transverse plane, $\frac{1}{2}\left(\langle v\rangle^2 + \langle w\rangle^2\right)$ in figure IV.18. Figure IV.19 is the kinetic energy of the turbulence in the transverse plane, $\frac{1}{2}\left(\left\langle v^2\right\rangle + \left\langle w^2\right\rangle\right)$. The uniformity across the tank in figure IV.18 suggests that within a few periods after breaking the mean flow in the transverse plane has become fairly homogeneous. There is some horizontal variability in the TKE field, but it is significantly less than the inhomogeneity seen in the longitudinal plane. It was thought that perhaps cross-stream structures may be formed due to a transverse variability similar to that seen by Perlin et al. (1996). It is possible that cross-stream structure is generated from breaking but that it dissipates quite rapidly and is not seen for these times.

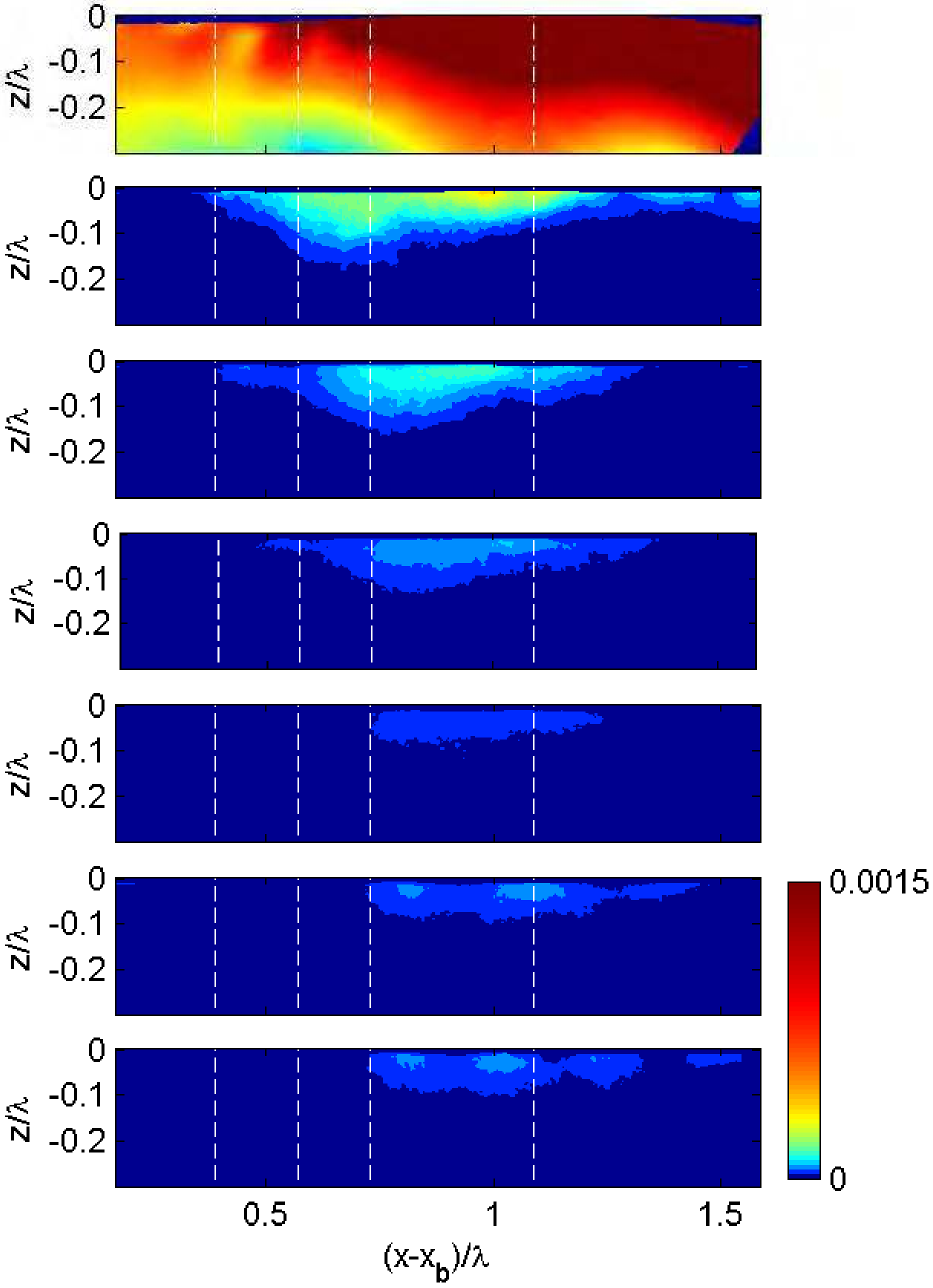

Figure IV.14: The normalized kinetic energy of the mean flow.

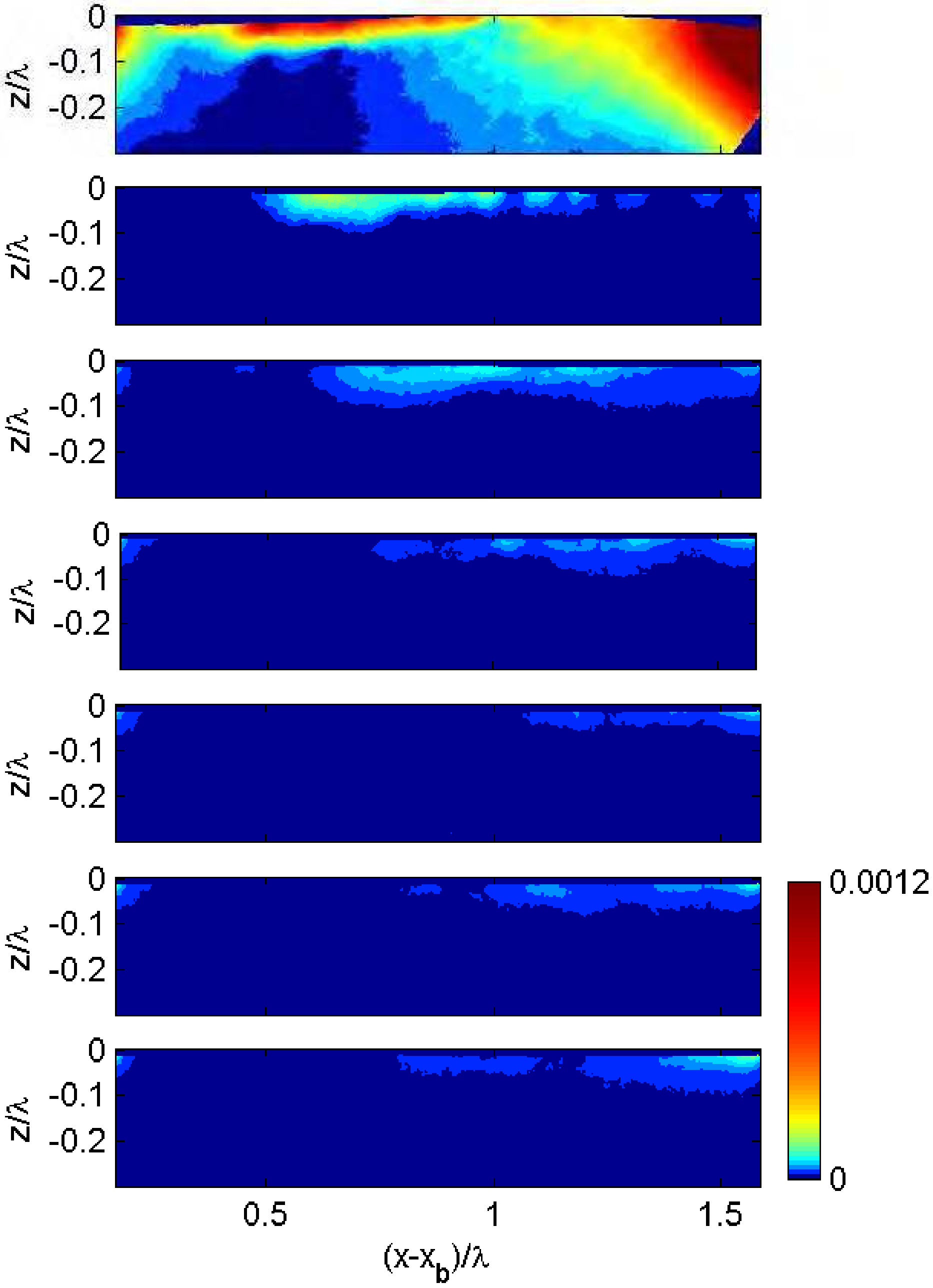

Figure IV.15: The normalized kinetic energy of the mean flow with the surface waves removed as in section IV.3.A.

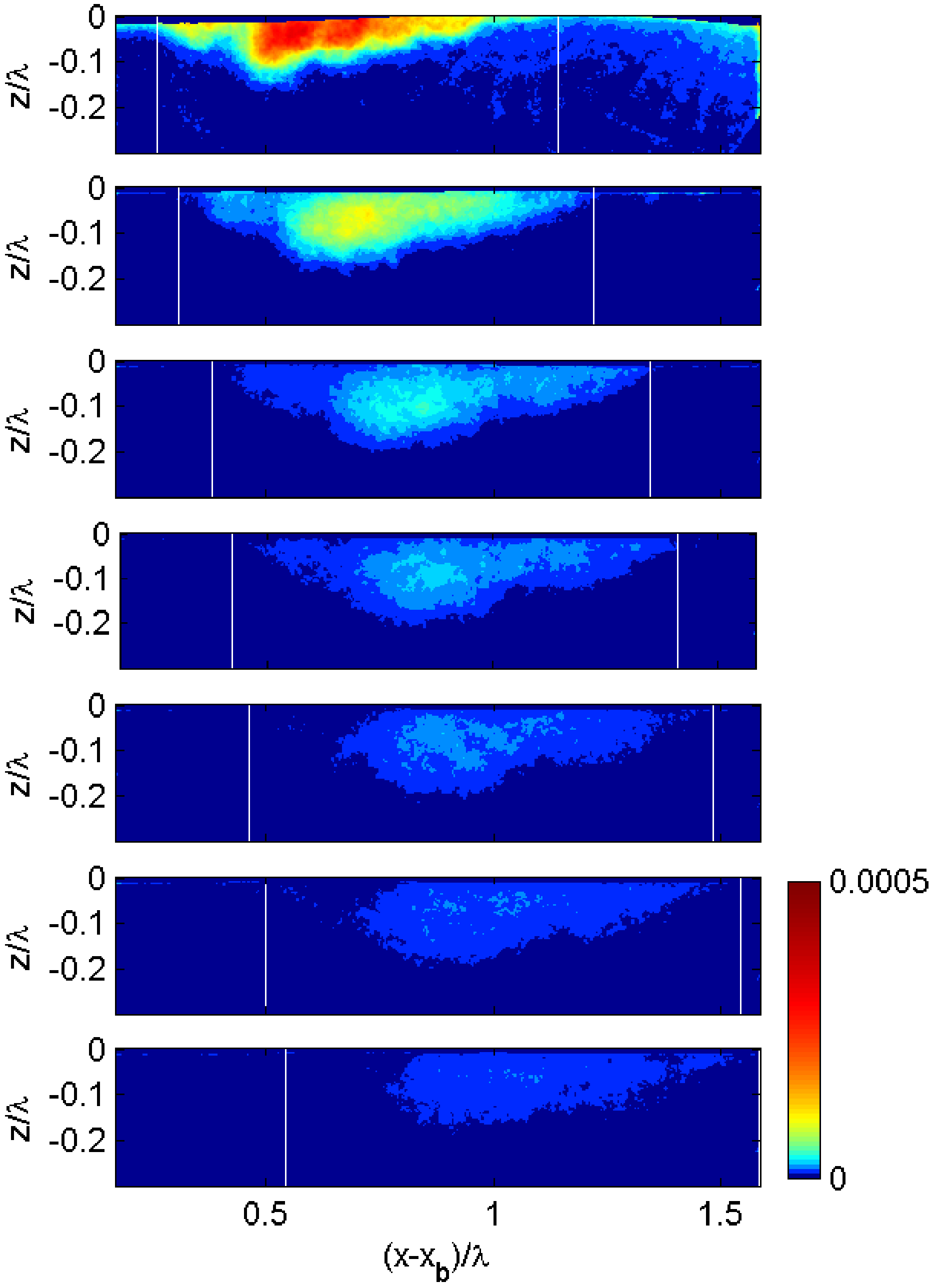

Figure IV.16: The normalized turbulent kinetic energy field for the same times as figure IV.7. The turbulent cloud can be seen to slowly deepen and move downstream. The vertical white lines denote the horizontal limits used when computing various turbulent statistics.

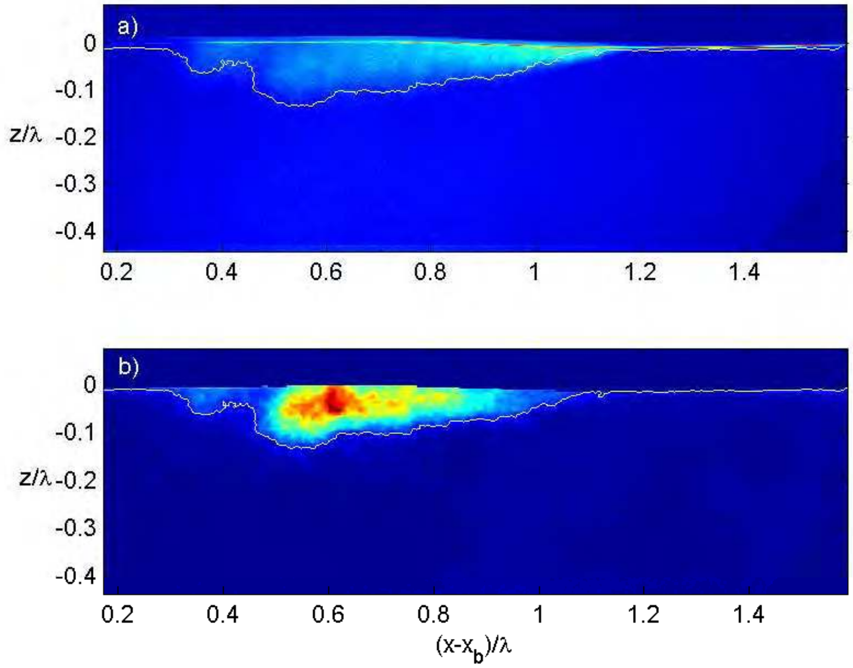

Figure IV.17: The a) ensemble-averaged image for $t^* = 5.58$. The $TKE = 8.22 \cdot 10^{-5}$ contour from b) is overlaid on the mean image in white. The vertical extent of particles mixed down from the surface correlates well with the subsequent turbulent cloud. b) Normalized TKE at 5.58 wave periods after breaking along with the outline of the cloud.

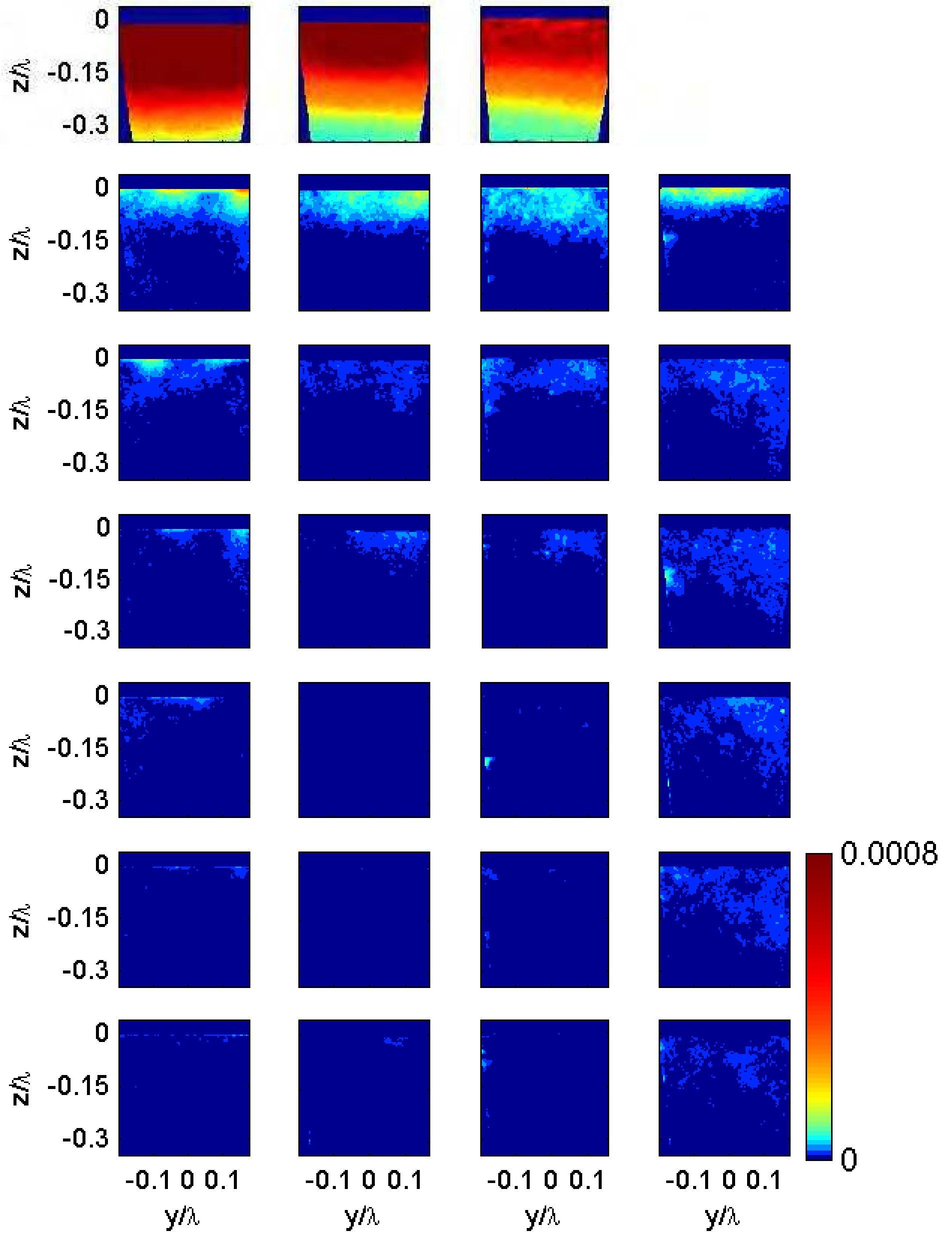

Figure IV.18: The normalized kinetic energy of the mean flow in the transverse plane.

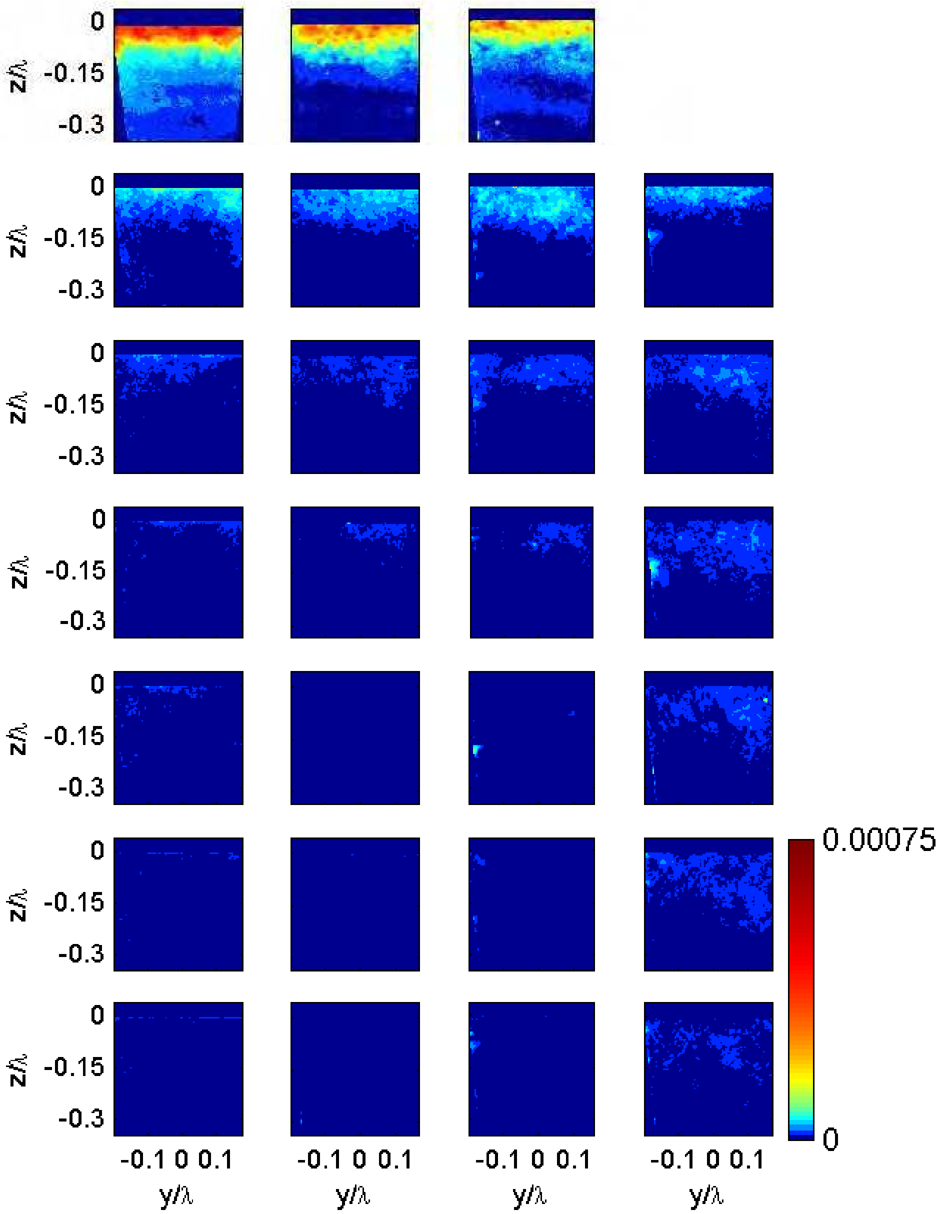

Figure IV.19: The normalized kinetic energy of the turbulent flow in the transverse plane.

## IV.3.C Reynolds Stress

The Reynolds stresses play in important role in the transfer of momentum from the surface wave field into the bulk of the fluid.

### Longitudinal plane

The Reynolds stress, $\langle uw \rangle$, is shown in figure IV.20. We see that the stress is overwhelmingly negative and is consistent with the findings of RM and MVW. It is this mechanism through which currents are generated and corresponds to the vertical transport of horizontal momentum. MVW additionally used these measurements of the Reynolds stress to infer a value of the breaking parameter, $b$. Estimates of $b$ based on the measured Reynolds stress here is examined in section IV.7.

### Transverse plane

The Reynolds stress in the cross-stream direction, $\langle vw \rangle$ is shown in figure IV.21. In contrast to $\langle uw \rangle$ there is no preferred direction of the stress. The symmetry of the flow in the transverse plane is maintained during the breaking event and thus we would expect there to be no net momentum transfer. Figure IV.22 shows that the integrated Reynolds stress is essentially zero in the transverse plane and that there is no net transport of momentum.

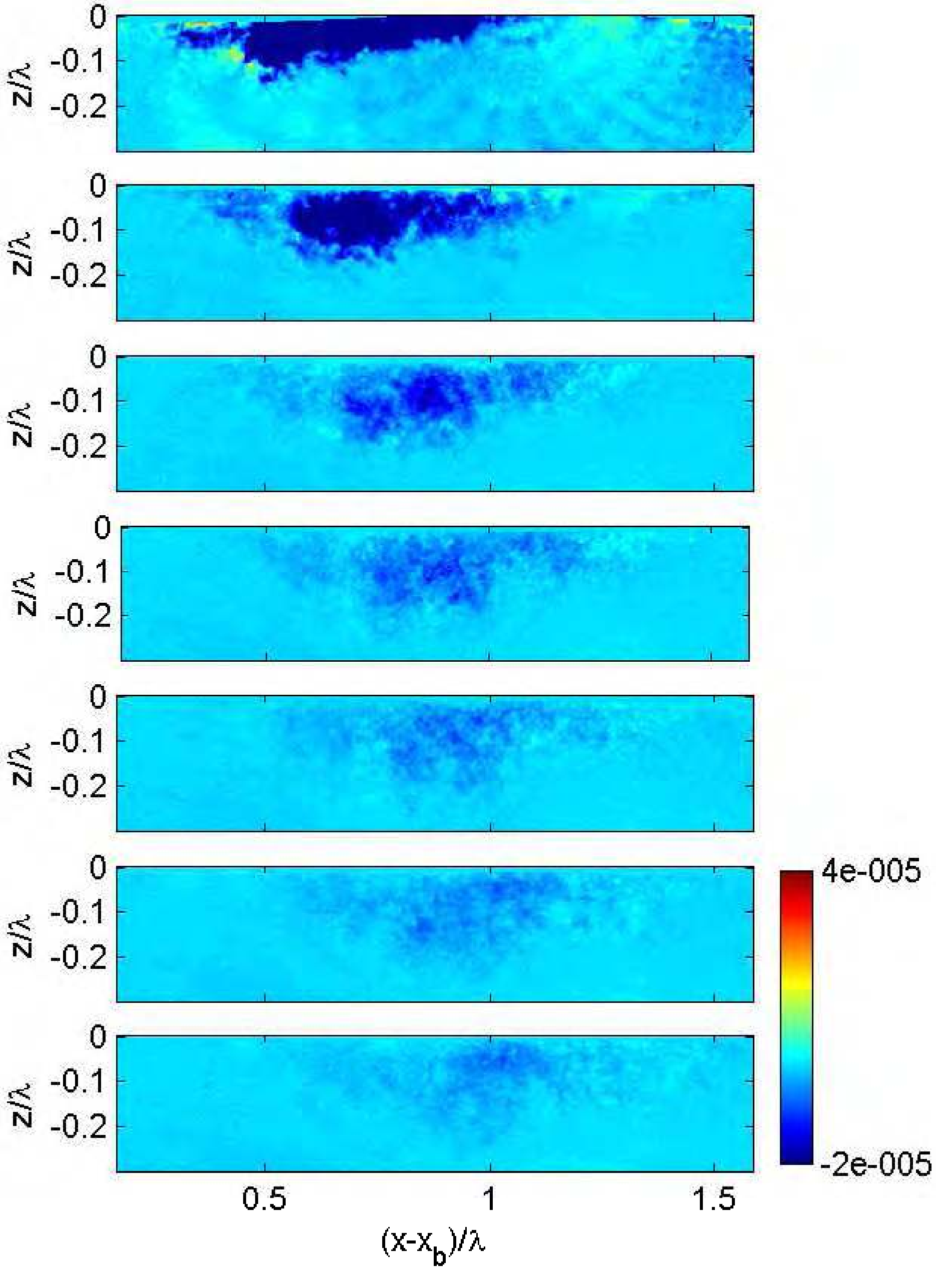

Figure IV.20: The normalized Reynolds stress of the turbulence, $\langle uw \rangle$ in the longitudinal plane. The stress is predominately negative and corresponds to the downward flux of positive momentum in the x-direction.

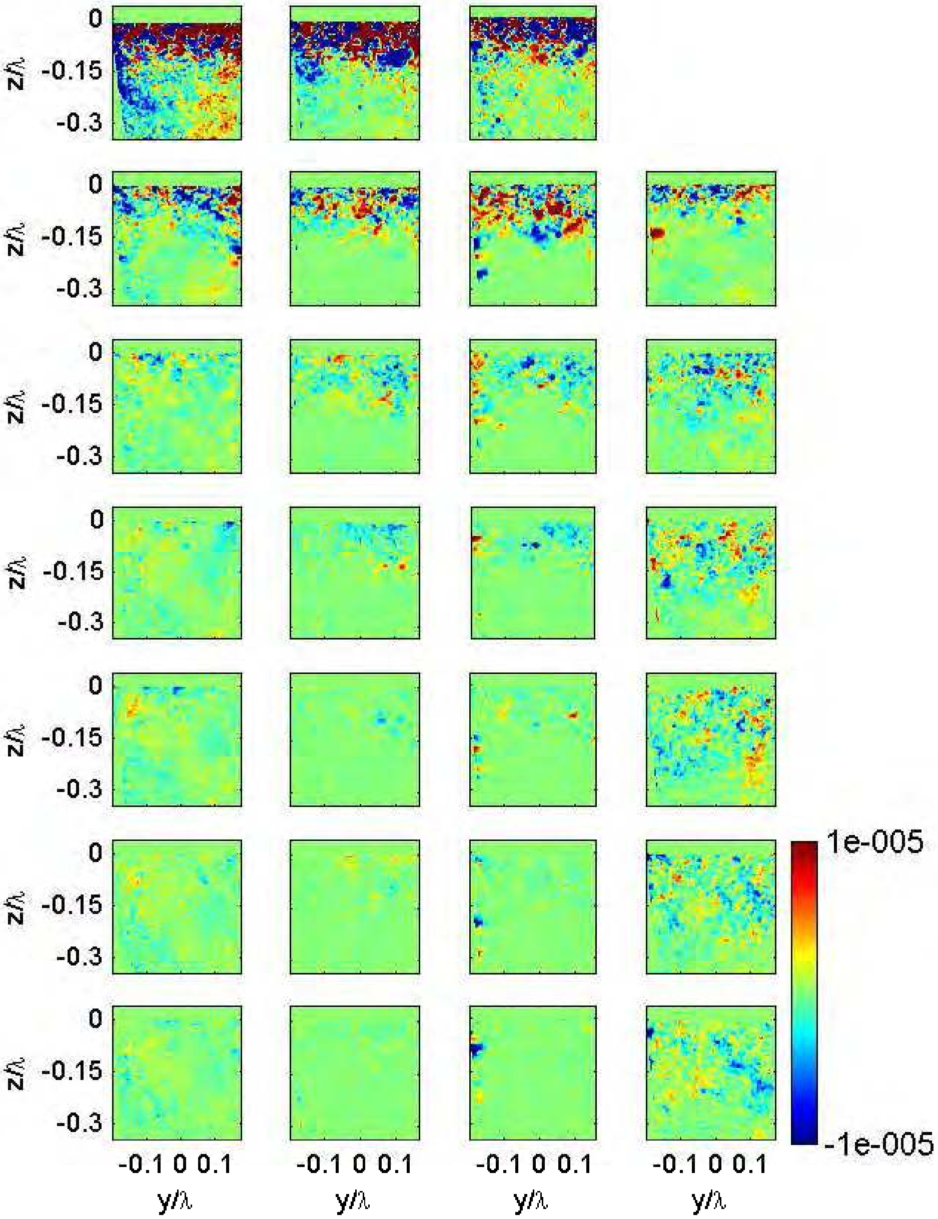

Figure IV.21: The normalized turbulent Reynolds stress ($\langle v'w' \rangle$ of the flow in the transverse plane.

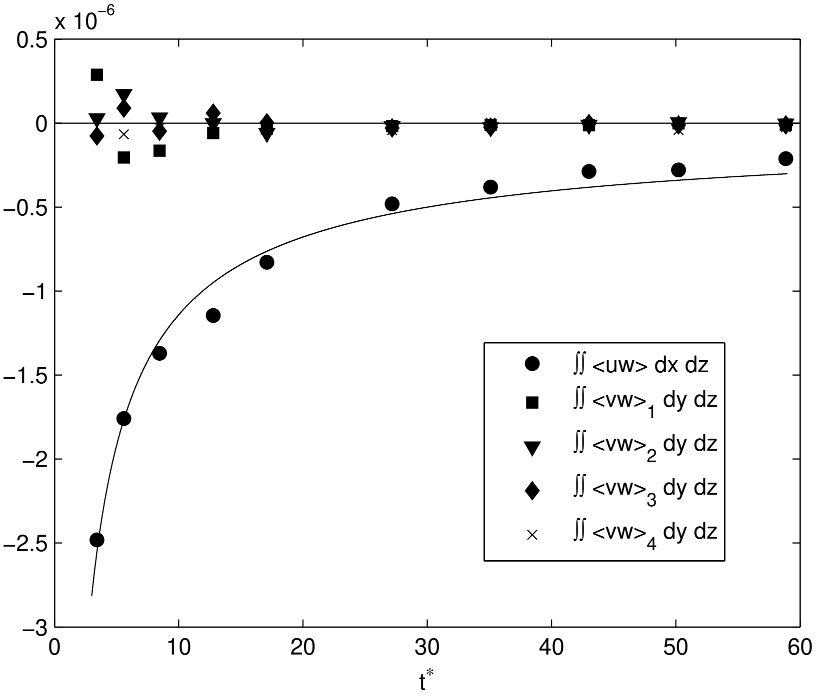

Figure IV.22: The integrated normalized Reynolds stress in both the longitudinal and transverse planes. The values of $\int\int\langle uw\rangle$ dx dz correspond to a net transport of positive horizontal momentum in the negative vertical direction. The net transport in the transverse plane is essentially zero. The subscripts refer to the location of the cross-stream measurement. The solid line is a $t^{-3/4}$ fit to the integrated Reynolds stress in the longitudinal plane.

## IV.3.D Turbulent Vorticity

The mean square vorticity is given by

$$\mathcal{W} = \left\langle (\Omega + \omega)^2 \right\rangle \tag{IV.25}$$

$$= \Omega^2 + \left\langle \omega^2 \right\rangle \tag{IV.26}$$

$$= \mathcal{W}_m + \mathcal{W}_t \tag{IV.27}$$

Where $\mathcal{W}_m$ and $\mathcal{W}_t$ are the squared mean vorticity and the mean squared turbulent vorticity. The mean square vorticity is equal to twice the enstrophy

### Longitudinal plane

We show the mean squared turbulent vorticity in the longitudinal plane in figure IV.23. If full resolved we could consider the mean squared turbulent vorticity can be thought of as a proxy for the dissipation. At the current resolution we cannot resolve the dissipative scales, since the dissipation occurs on scales comparable to the Kolmogorov lengthscale, $\eta$. We can see however that the region over which it is significant correlates well with turbulent cloud. As seen with the previous quantities, it is advected downstream with the coherent structure generated by breaking.

### Transverse plane

The mean squared turbulent vorticity in the transverse plane is shown in figure IV.24. It can be seen to be fairly homogeneous across the channel, similar to the TKE density in the transverse plane.

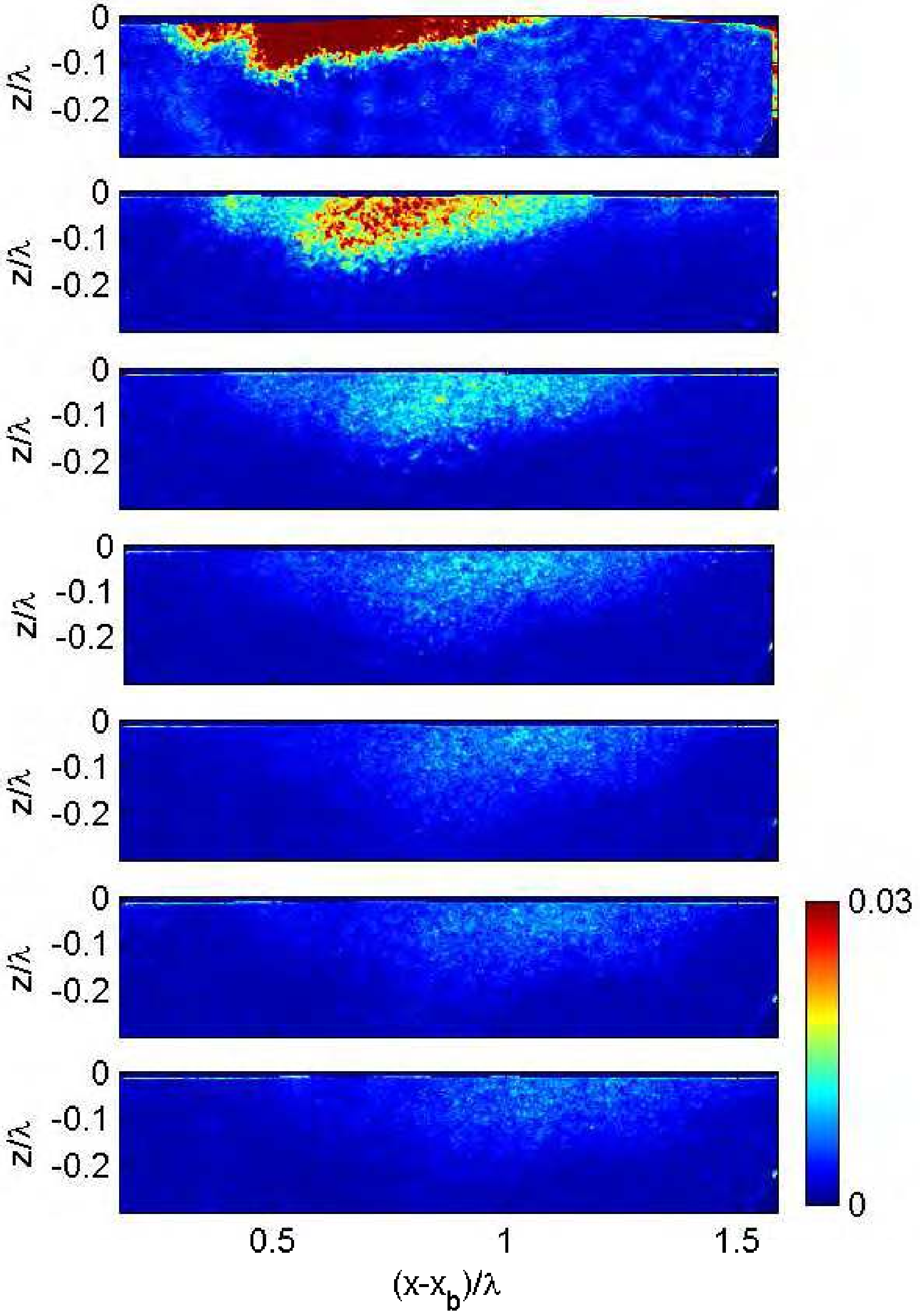

Figure IV.23: The normalized mean squared turbulent vorticity, $\mathcal{W}$, or twice the enstrophy. The squared turbulent vorticity is concentrated in regions of high TKE and decreases quite rapidly.

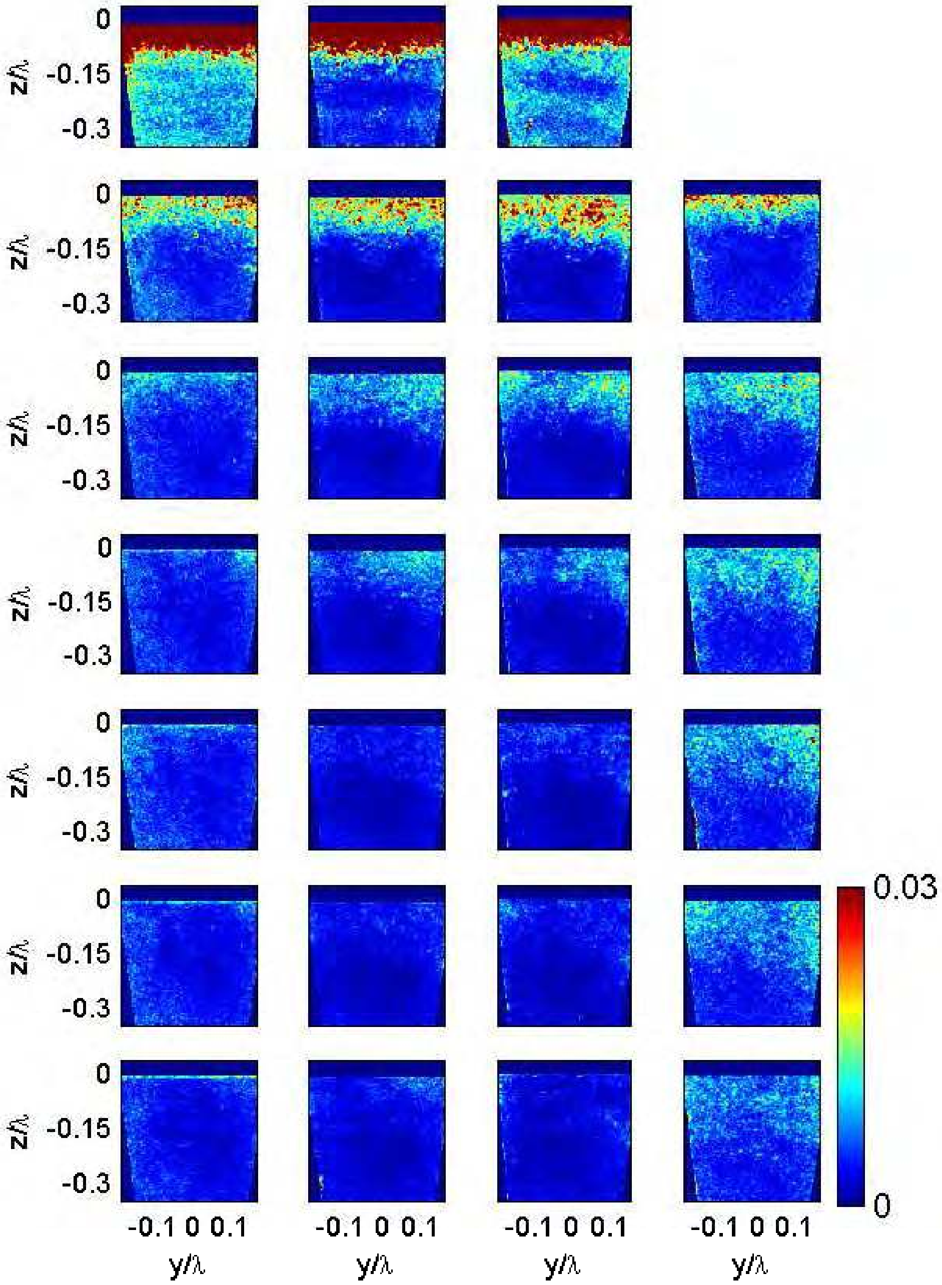

Figure IV.24: The normalized mean squared turbulent vorticity, $\mathcal{W}$, in the transverse plane.

### IV.3.E Time-Dependence of TKE and $E_m$

Figure IV.25a presents integrated quantities of the total energy $E = E_t + E_m$, turbulent kinetic energy $E_t$, and the kinetic energy of the mean flow, $E_m$ in the longitudinal plane. The area over which the integration was conducted was windowed horizontally and restricted to $z > -0.23$. The kinetic energy initially dominates as the surface waves propagate through the measurement region. When $t^* \approx 12$, $E, E_m, E_t$ begin to show a $t^{-1}$ dependence, which is consistent with the findings of RM and MVW.

Figure IV.25b shows the integrated values of the turbulent kinetic energy for both the full-field DPIV, TKE, and the mosaic DPIV, $E_{t_M}$. In order to compare the two results in the longitudinal plane, the full-field measurement is first broken up into three windows corresponding the same dimension as the mosaic DPIV. The integrated energy is calculated in each window and then these three estimates are summed. Due to the slight overlap in the mosaic DPIV (by $\approx 9$ cm) the magnitude of the integrated TKE will be slightly higher in b) than in a), but the time dependence should not change. The full-field measurements are made to within 6 mm of the surface, while the mosaic DPIV is within 2.4 mm. If the full-field measurements are linearly interpolated to the same time values as $E_{t_M}$, then $E_{t_M}$ is seen to be $\approx$14% larger. The integrated TKE density curves appear to have a $t^{-1}$ dependence for $t^* > 12.78$. For $t^* < 12.78$ the decay is slower and is approximately $t^{-\frac{1}{2}}$.

### IV.3.F Results for $t^* < 3.42$

The results of the previous section focused on the full-field evolution of various quantities. The intensity of the turbulent and mean velocities decrease quite rapidly after breaking. RM showed that up to 90% of the total energy dissipated by the flow was lost within the first four wave periods. It is of interest to examine the velocity field for $t^* < 3.42$.

When extending DPIV measurements close to the breaking location a number of concerns need to be addressed. Plunging waves entrain a large amount of air. Lamarre

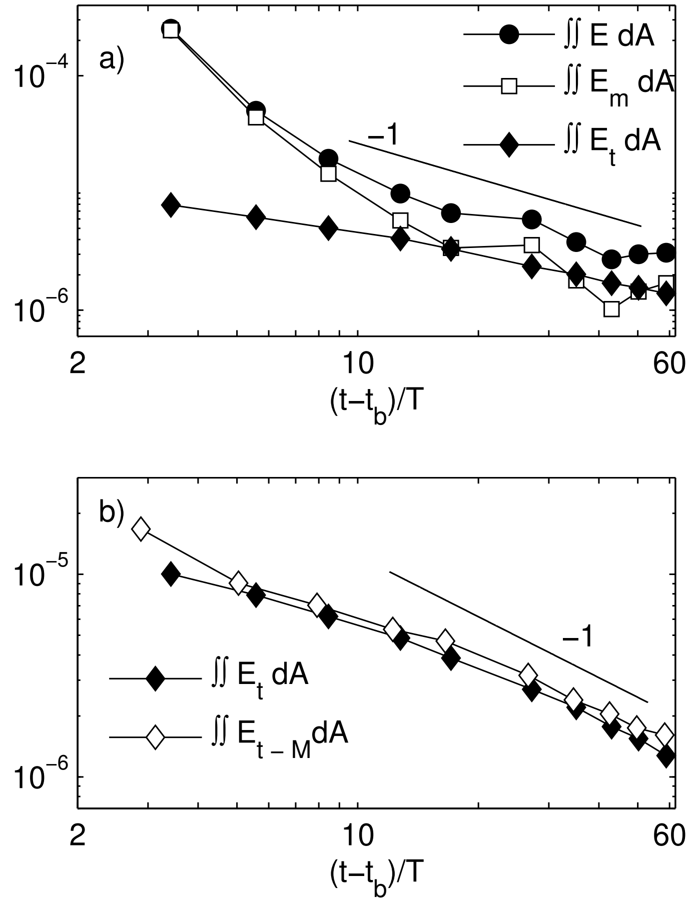

Figure IV.25: a) Integrated $E = E_m + E_t$, $E_m$, and TKE for the full-field DPIV measurements. b) Comparison between TKE of the full-field and $E_{t-M}$ mosaic DPIV.

and Melville (1991) measured void fractions under breaking waves and found that the fraction of air entrained ranged from ≈54% at $t^* = 0.26$ to ≈0.8% at $t^* = 1$. These dense bubble plumes scatter large amounts of light and can make DPIV analysis difficult. Relatively large amplitude surface waves are present at these times and can significantly distort the free surface. With this in mind we present results of the flow for the first four data points we have after breaking, $t^* = [0.54, 1.26, 1.98, 2.70]$.

Figure IV.26 shows a subsection of the raw image data at $t^* = 0.54$ with the computed velocity field overlaid. The vector field has been set to zero above the mean free surface (i.e. mean surface computed from the ensemble-averaged image data), and the vector spacing has been decimated by a factor of three for ease of viewing. There is a highly aerated region at the front of the advancing breaker, but there appear to be sufficient gradients in the image intensity to allow for computation of vector fields. The velocity field shown is the output of the window-shifting step before any outlier removal or filtering is performed. Ryu, Chang, and Lim (2005) used a similar technique in order to measure plunging wave interaction with structures. In regions of the flow which had high void fractions, Ryu et al. (2005) used the bubbles as a tracer.

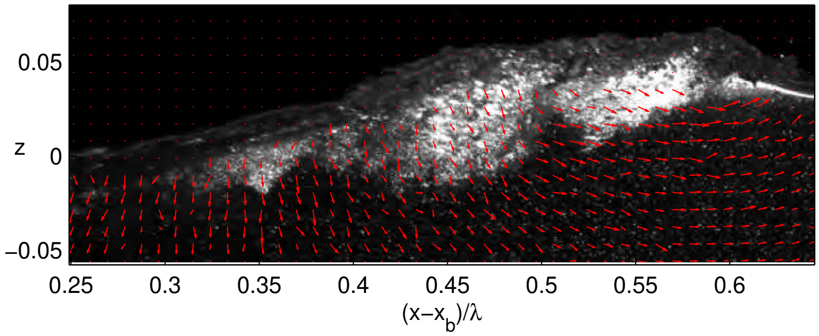

Figure IV.26: Shown is the highly aerated region of active breaking at $t^* = 0.54$. The velocity field shown is the output of DPIV algorithm after window-shifting and before any outlier removal or smoothing has been applied, see section IV.2.B.

### Velocity, Vorticity, and TKE density

The ensemble-averaged velocity field, $(\langle u(\mathbf{x}, t)\rangle, \langle w(\mathbf{x}, t)\rangle)$, is shown in figure IV.27. The dominant feature of the flow is the velocity induced by the surface waves.

Figure IV.28 is the the ensemble-averaged vorticity field, $\langle \omega \rangle$. Since the surface waves are essentially irrotational, taking the curl of the velocity removes their influence and the region being mixed down by the advancing wave is clearly seen. At the front of the breaking event, a region of positive (counter clockwise) vorticity is seen as fluid is swept up and to the right. Following the wave we have a large region of negative (clockwise) vorticity which grows in time and is the source of the large region

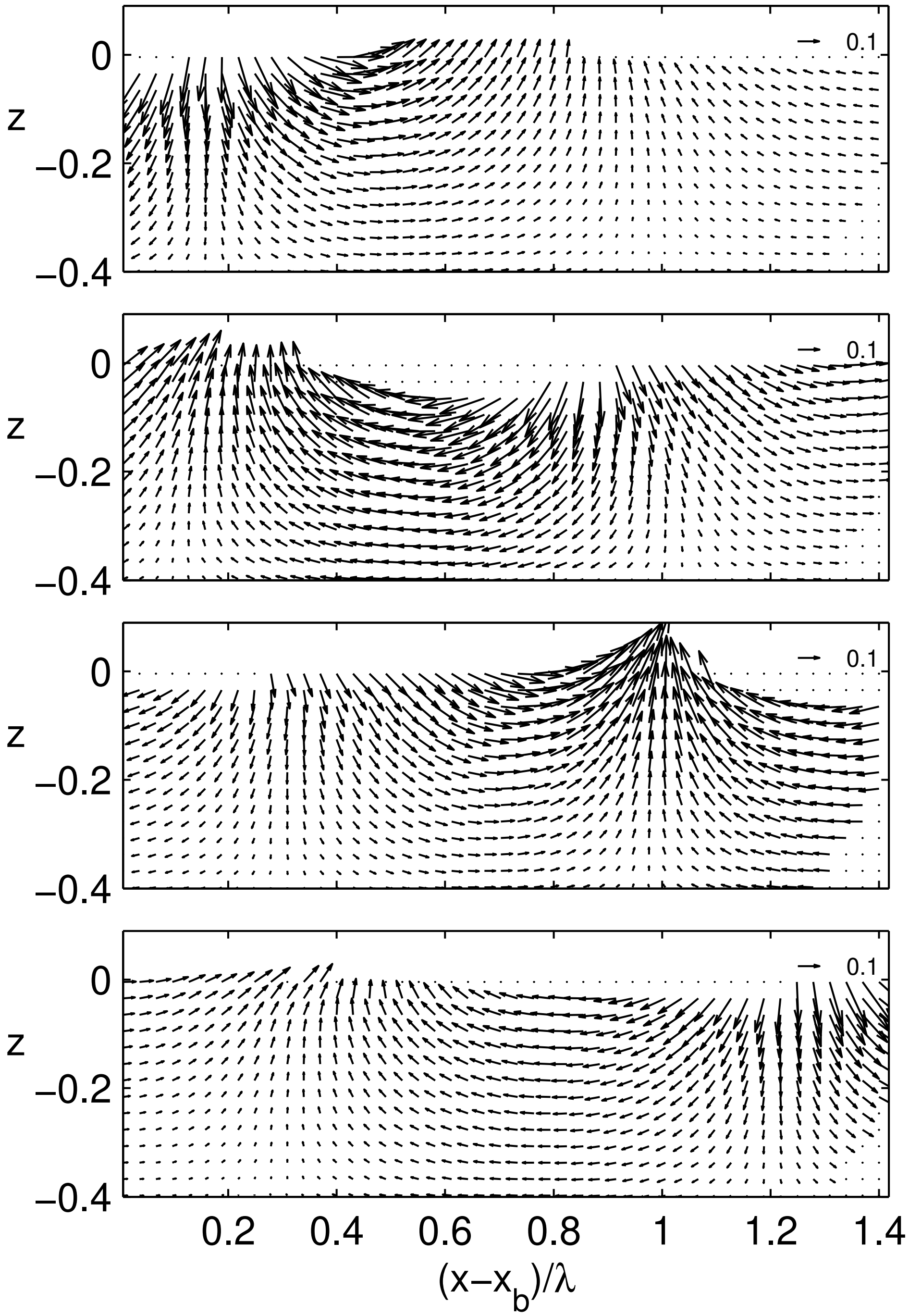

Figure IV.27: Quiver plots of the ensemble averaged velocity field for the first four image pairs collected after breaking, time is $t^* = [0.54, 1.26, 1.98, 2.70]$

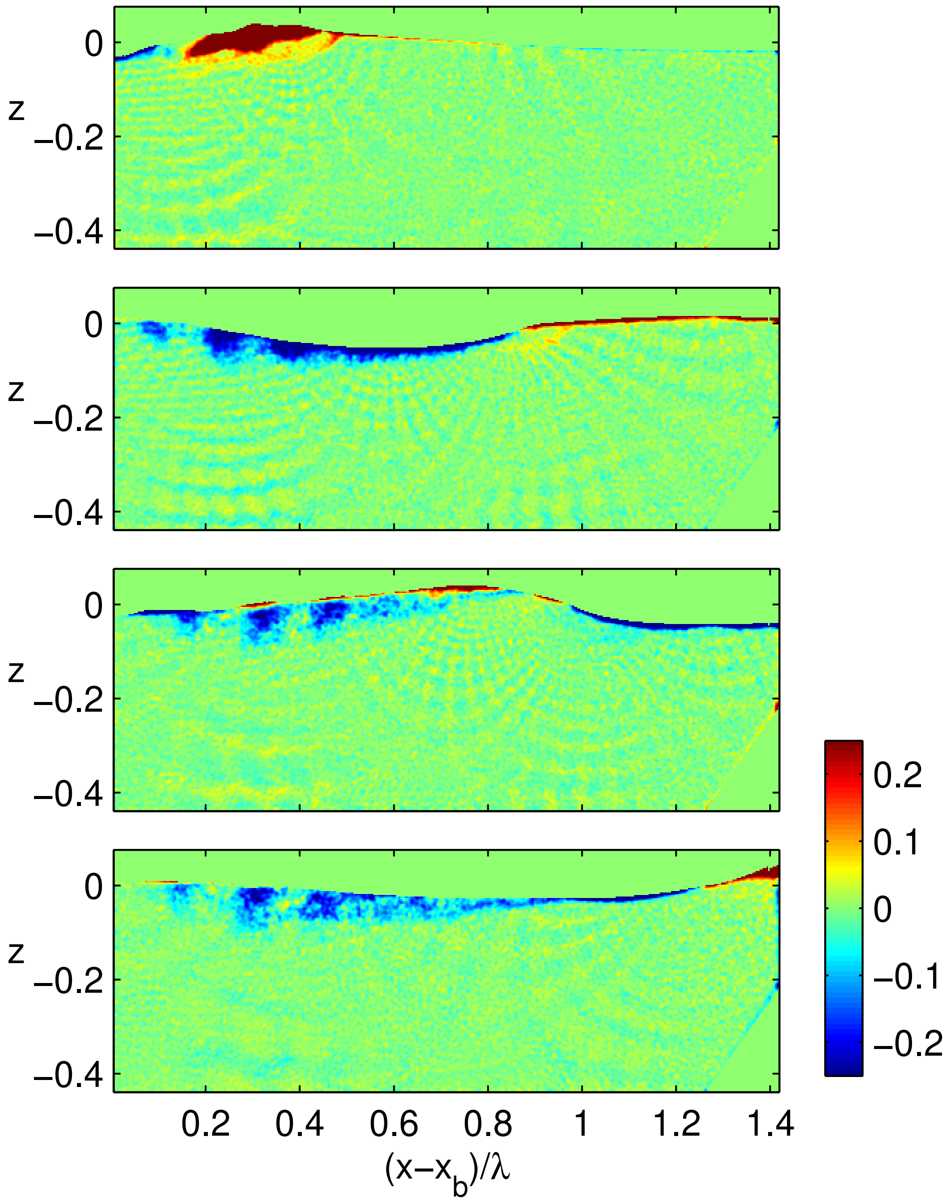

Figure IV.28: The ensemble averaged vorticity for the first four image pairs collected after breaking. Negative vorticity corresponds to a clockwise rotation, and positive vorticity to counter-clockwise rotation. The pattern seen outside of the breaking is thought to be related to the streamlines of the flow.

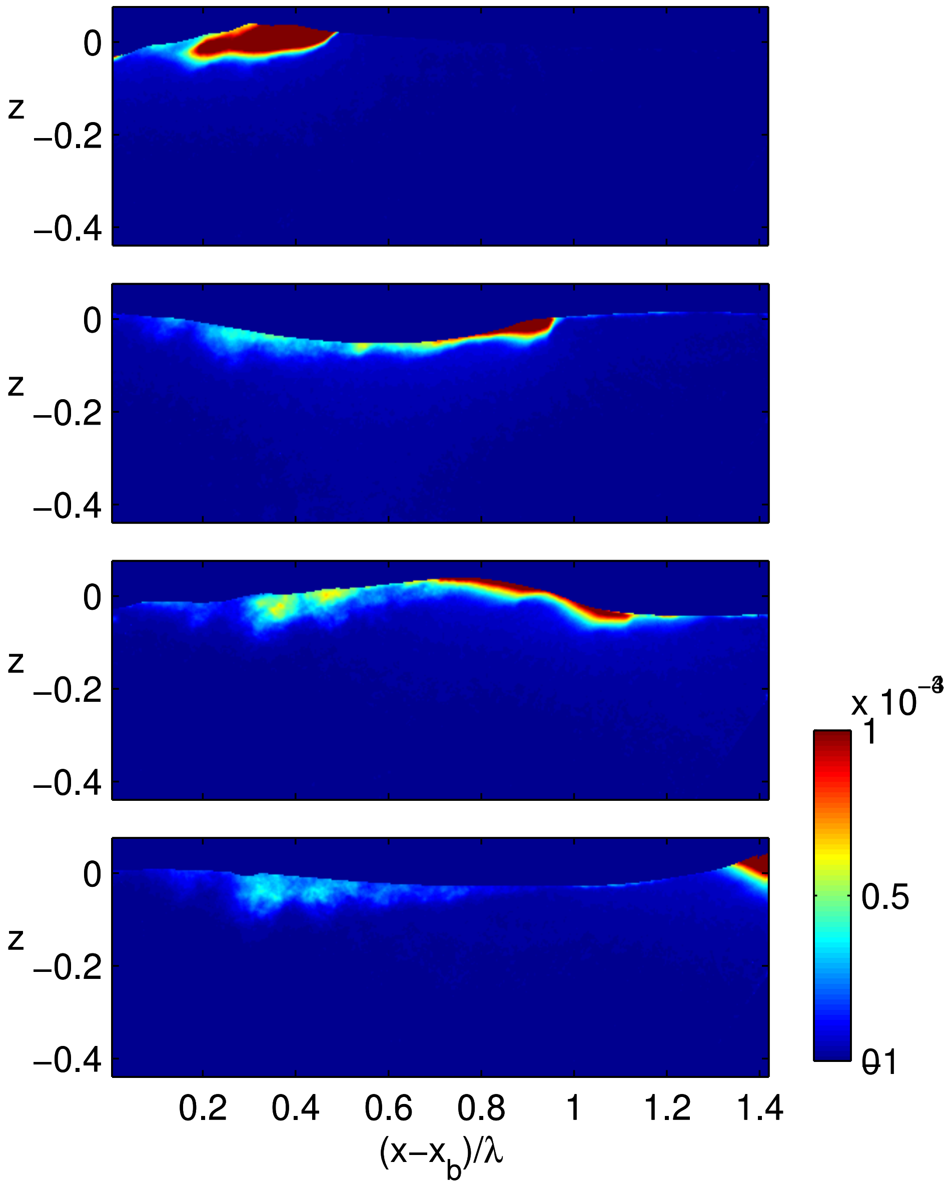

Figure IV.29: The turbulent kinetic energy density of the flow for the first four wave periods.

of negative vorticity seen at $t^* = 3.42$. A mechanism proposed by Bonmarin (1989) seems apply here in which a large eddy is formed which rotates clockwise (negative vorticity). Bonmarin (1989) stated that analysis of cine images of breaking suggested that the falling jet from the plunging wave creates a coherent eddy in the fluid. This is better understood by examining figure IV.30, which is a sequence of images of a plunging breaking wave for $t^* = [0, 0.09, 0.19, 0.27]$ taken by a high-speed camera (1000 Hz). In figure IV.30a the wave has impacted the water surface below and is seen to start to push the water underneath the impact region as it moves forward and down at an angle (figure IV.30b). By $t^* = 0.19$ (IV.30c) a secondary splash-up region is seen and the arrows denote the direction in which the fluid is moving. A clockwise flow is set up which revolves around the entrained air cavity and within the large splash-up region just downstream. The region of counter-clockwise rotation is due to the return flow on the downstream side of the jet impact location. This mechanism would explain the large region of negative vorticity that forms quite soon after breaking, see figures IV.28 and IV.9. However, other sources of vorticity could also be baroclinic generation due to the large void fractions present after breaking or by capillary waves associated with the breaking front sweeping downstream. (Longuet-Higgins, 1992).

Measurements of TKE are shown in figure IV.29. The extent of the mixing agrees well with that of the ensemble averaged vorticity. The energy levels are quite high in the region of the breaking front that is being advected downstream by the surface waves, suggesting a shear layer in which the front edge is highly turbulent.

As seen in figure IV.28 a very distinct pattern is evident outside of the mixed region. This pattern is similar to that seen by Chang and Liu (2000) and Chang and Liu (1999), which they called “pseudo-turbulence”. The pattern seen here is very wavelike and changes as the breaking event propagates to the right. In figure IV.28 for $t^* = 0.54$ and 2.7, the pattern is seen to be less distinct in front of and behind the advancing front. It is thought that the pattern is caused by waves which are being radiated away from the propagating front of the breaking event. The velocities within these bands are quite small and become quite apparent once the gradient is taken, which is why they are

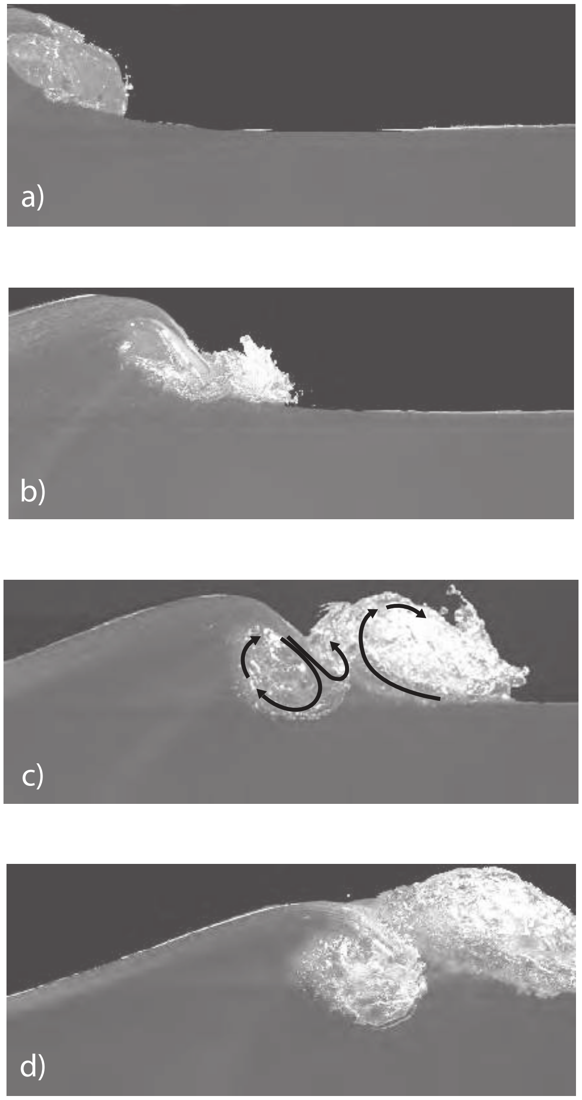

Figure IV.30: A sequence of images of a plunging breaking wave as recorded by a high-speed camera for a) $t^* = 0$, b) $t^* = 0.09$, c) $t^* = 0.19$, and d) $t^* = 0.27$. The arrows in c) show the flow direction for both the initial impact region and the downstream splash-up region.

apparent in figure IV.28 and not in IV.27. This pattern is thought to be due to the flow streamlines, but a firm conclusion has not been drawn yet.

### Estimation of $\nu_T$

The extent of the mixing caused by breaking can be better understood if we remove the distortion caused by the surface waves. We step-through each ensemble-averaged image column by column and use the surface elevation $\eta(x,t)$ to adjust each column up or down relative to the free surface. In this frame of reference the the free surface is now horizontal. These adjusted images are shown in figure IV.31 for $t^* = 0.54 - 2.70$. The mixed region consists of bubbles entrained by the breaking process and particles which have been mixed down from the surface. The boundary of the mixed layer shows an approximately $x^{1/2}$ dependence. We can estimate an eddy viscosity, $\nu_T$, using

$$\nu_T(t) = \frac{\delta(x)^2 U}{x} \tag{IV.28}$$

where $\delta$ is the boundary-layer thickness, $U$ is the speed of the advancing breaking front, and $x$ is the distance from the front.

The length of the mixed region versus $t^*$ is shown in figure IV.32. The initial rate of expansion of the mixed region is quite rapid, $U = 0.66C_c$, where $C_C$ is the center phase-speed of the packet. After $t^* \approx 3$ the length of the mixed region expands more slowly, $U = 0.007C_c$. These results agree with the findings of RM, who found the initial speed to be $U = 0.7 - 0.8C_c$, which after three wave periods, decreased to $U = 0.005 - 0.01C_c$. The area of the mixed region can also be obtained from the raw image files seen in figure IV.31 A plot of the non-dimensional area versus $t^*$ is shown in figure IV.33. The area can be seen to grow as $t^{1/2}$ which matches the time dependence found by RM.

The eddy viscosity is found by fitting the boundary layer thickness, $\delta$ to a $x^{1/2}$ curve and evaluating (IV.28). The thickness of the boundary layer is seen to oscillate consistent with coherent structures or eddies in the ensemble-averaged flow. A minimum and maximum value of $\nu_T$ is found corresponding to the range of these structures. Figure

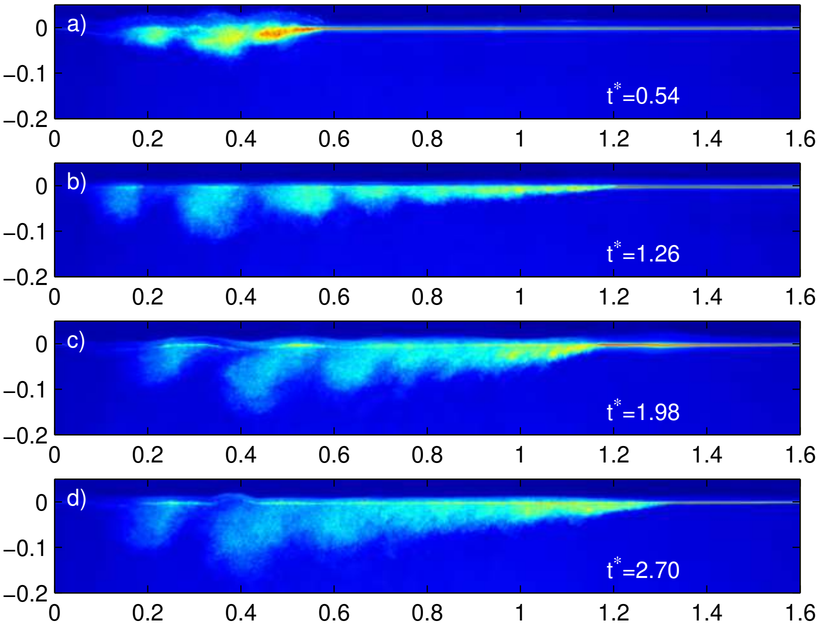

Figure IV.31: The raw ensemble-averaged image data in false-color. The region mixed by breaking consists of air entrained by breaking along with particles mixed down from the surface. Each image has been shifted vertically column by column to give the vertical position relative to the free surface.

IV.34 shows the extracted boundary layer for $t^* = 2.70$ along with the boundary layer showing the range of $\nu_T$.

The value of $\nu_T(t)$ for $t^* < 2.70$ is shown in figure IV.35a and for $t^* > 2.70$ in figure IV.35b. The eddy viscosity is seen to increase linearly in time with a slope of $0.006\text{m}^2\text{s}^{-2}$ for IV.35a and $0.4 \cdot 10^{-4}\text{m}^2\text{s}^{-2}$ for IV.35b.

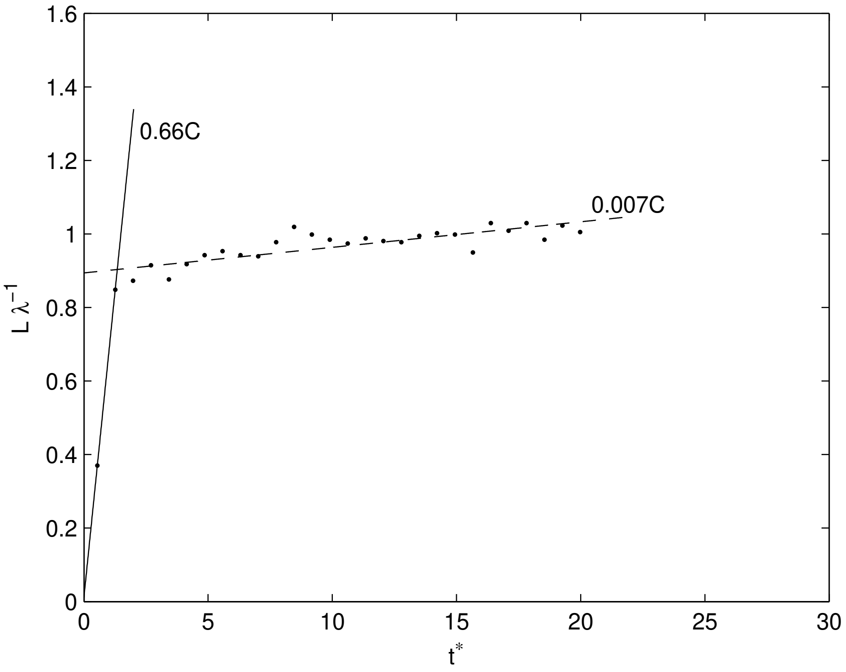

Figure IV.32: The normalized length of the breaking region at the surface. The horizontal extent of the breaking region initially expands quite rapidly with a speed $U = 0.66C_c$ and then slows to $U = 0.007C_c$ after $t^* \approx 3$.

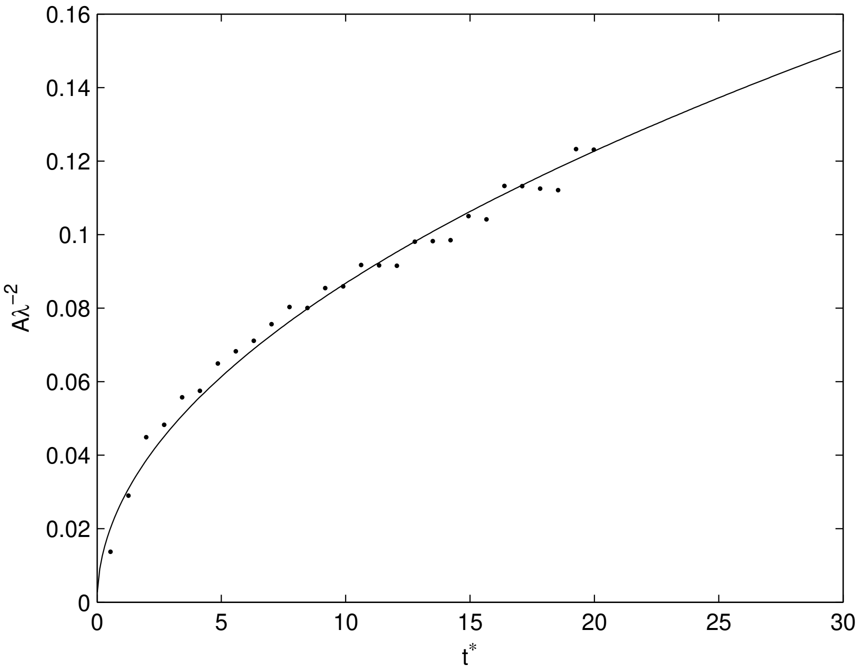

Figure IV.33: Plot of the non-dimensional area mixed by the breaking wave as measured from the raw image files. The solid line is a $t^{1/2}$ fit which is the same time dependence found by RM.

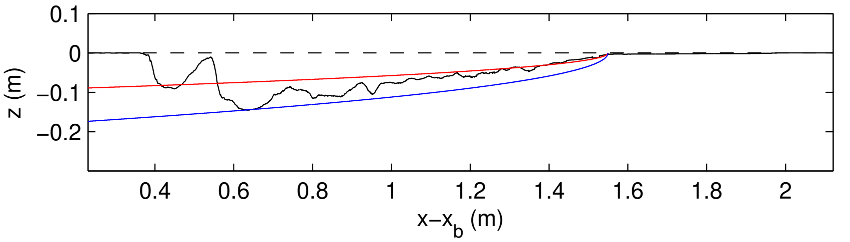

Figure IV.34: The outline of the mixed region for $t^* = 2.70$ superimposed with the boundary layer thickness $\delta(x)$. The red and blue lines denote the range of $\nu_T$ for the given mixed region.

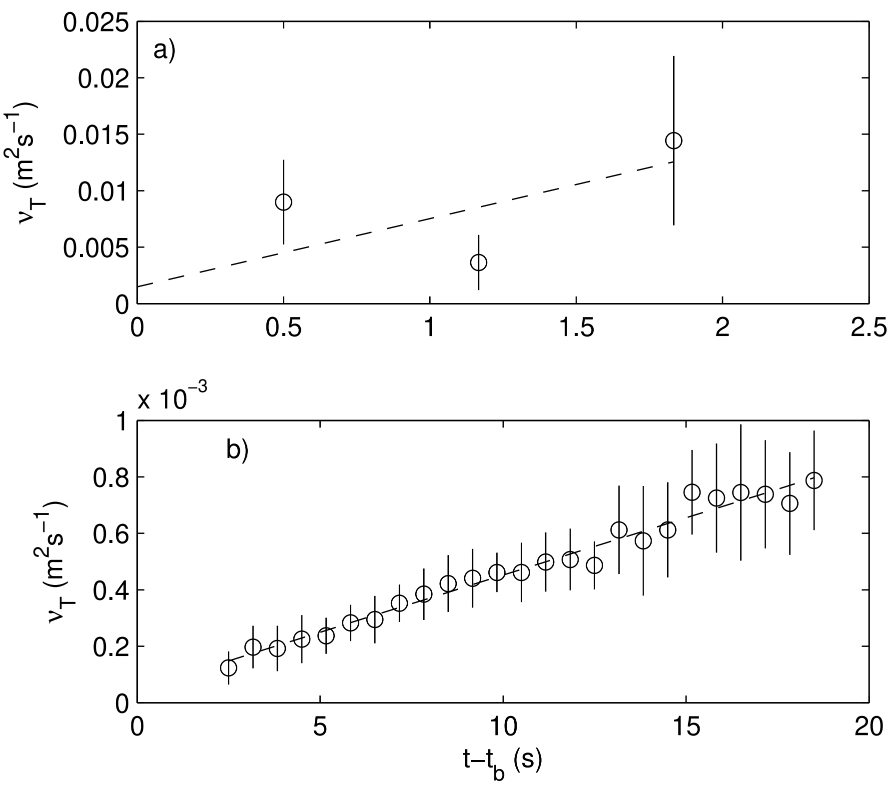

Figure IV.35: The measured eddy viscosity, $\nu_T$ as a function of time after breaking for a) $t^* < 2.70$ and b) $t^* > 2.70$. The vertical bars represent the maximum and minimum values of $\nu_T(t)$ and the dashed line is a least-squares fit of the data to a straight line.

## IV.4 Turbulent Length Scales

To aid in interpretation of the turbulence, it is useful to consider some representative lengthscales, the integral lengthscale and the Taylor microscale. For a given depth in the flow and time the longitudinal integral lengthscale is defined by

$$L_{11} = \int_0^\infty f(r)\,\mathrm{d}r \qquad \text{(IV.29)}$$

where

$$f(r) = \frac{\langle u_1(x_1 + r, t)u_1(x_1, t)\rangle}{\langle u_1(x_1, t)u_1(x_1, t)\rangle}\,, \qquad \text{(IV.30)}$$

and $L_{11}$ denotes the two-point correlation of $u_1$ in the $x_1$ direction. The integral lengthscale is then a measure of the decorrelation lengthscale of the turbulence and is a characteristic lengthscale of the energetic eddies within the flow. $L_{11}$ grows in time as seen in figure IV.36a, and is evaluated at each time for both a fixed point within the flow,$(x^*, z/\lambda) = (0.58, -0.034)$, and a point allowed to move at the speed of which the coherent vortex is deepening, $w = -0.001\text{ms}^{-1}$. The horizontal limits over which (IV.29) is computed, moves with the cloud at an average speed of $u = 0.01\text{ms}^{-1}$.

Another lengthscale derived from the velocity correlation is the Taylor microscale,$\lambda_f$, originally defined by Taylor (1935). By expanding the velocity correlation at the origin, $\lambda_f$ can be seen to be the x-intercept of the parabola which osculates with the velocity correlation at the origin,

$$\lambda_f = \left[-\frac{1}{2}f''(0)\right]^{-1/2}. \qquad \text{(IV.31)}$$

In homogeneous, isotropic turbulence (IV.31) then reduces to

$$\lambda_f^2 = \frac{2u'^2}{\left\langle\left(\frac{\partial u_1}{\partial x_1}\right)^2\right\rangle} \qquad \text{(IV.32)}$$

where $u'$ is the rms value of $u_1$. For the flow considered here, we used (IV.32) to define $\lambda_f$, seen in figure IV.36b. The values of $\lambda_f$ can be seen to decrease with time and are approximately 1/5 the size of $L_{11}$. The dissipation rate in an isotropic homogeneous flow is given by

$$\epsilon = 15\nu\left\langle\left(\frac{\partial u_1}{\partial x_1}\right)^2\right\rangle \tag{IV.33}$$

$$= 30\nu\frac{u'^2}{\lambda_f^2} \tag{IV.34}$$

after substitution of (IV.32). From (IV.34) it can be seen that the Taylor microscale is a lengthscale associated with the dissipation rate and the rms turbulent velocity, see figure IV.36c. A Reynolds number based on the Taylor microscale is given by

$$Re_\lambda = \frac{u'\lambda_f}{\nu} \tag{IV.35}$$

and is commonly used to quantify turbulent flows. Values of $Re_\lambda$ at two depths are shown in figure IV.37 as a function of time. The value of $Re_\lambda$ is initially large and asymptotically approaches 100 with $t^*$ for for both depths. Pope (2000, see figures 6.20, 6.22) shows that for large values of $Re_\lambda$ in statistically stationary flows the separation between the energy containing scales and the dissipative scales grows, a consequence of which an enlarged inertial subrange exists in which viscous effects are negligible. However, this is not a statistically stationary flow and a relatively simple characterization of the conditions under which an inertial subrange exists may not be possible.

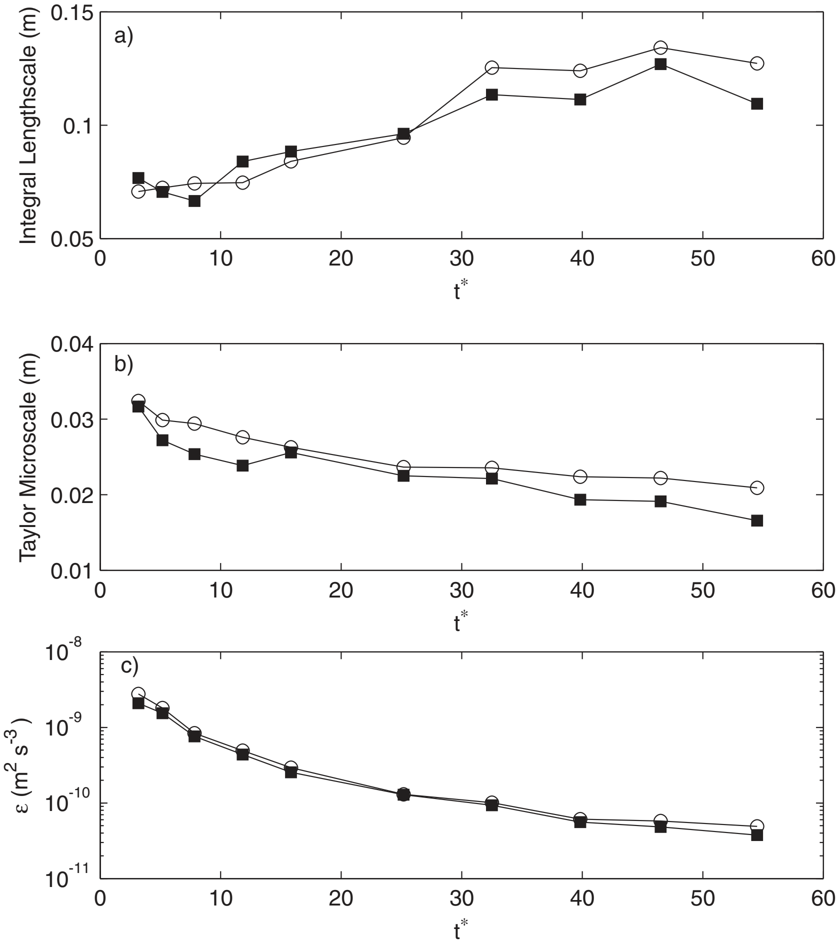

Figure IV.36: a) $L_{11}$, b) $\lambda_f$, and c) $\epsilon = 30\nu u'^2/\lambda_f^2$ as a function of non-dimensional time after breaking. The open symbols correspond to a fixed point in the flow $(x^*, z/\lambda) = (0.58, -0.034)$, while the measurement depth of the solid symbols followed the deepening of the TKE cloud.

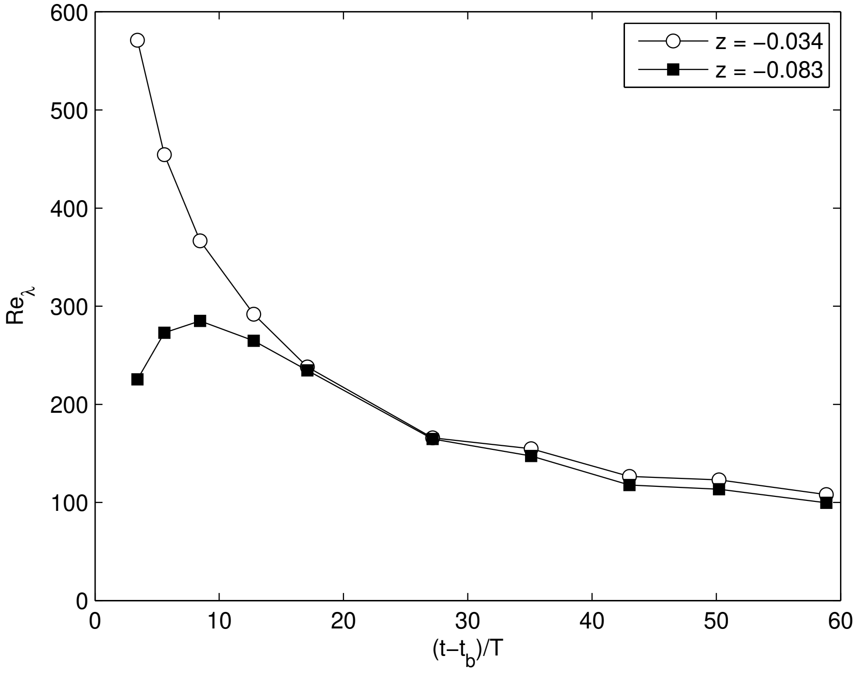

Figure IV.37: Plot of the Taylor microscale Reynolds number, $\mathrm{Re}_\lambda = \frac{u'\lambda_f}{\nu}$ at two depths in the flow.

## IV.5 Wavenumber Spectra

The instantaneous large-scale measurements of the flow along with the large ensemble collected are well suited for computation of spectra over a large range of wavenumbers. The ensemble-averaged one-sided wavenumber spectra are calculated using

$$E_{ii}(k) = \frac{2}{XM} \sum_{m=1}^{M} |\hat{u}_i(k,t)|^2 \qquad \text{(IV.36)}$$

where $X$ is the spatial length of the signal, $k$ is the wavenumber, $M$ is the number of realizations over which the spectrum is averaged, and $u_i(\hat{k}, t)$ is the FFT of $u_i(x, t)$. Prior to computing (IV.36) all datasets in the $x_i$ direction are detrended and windowed using a cosine tapered window applied to the inital and final 10% of the data. Due to the inhomogeneity of the flow, the limits of the window in the $x_1$ direction are set using the vertical lines seen in figure IV.16, i.e. only the energetic portion of the flow is considered. The spectra in the $x_3$ direction extend from the free-surface, $\eta(x, t)$, to $z = -0.23$.

### IV.5.A Measurements of $E_{11}$ and $E_{33}$

Spectra of $E_{11}$ and $E_{33}$ in the $k_1$ direction are shown in figure IV.38 for $z = -0.06$. The normalized times after breaking are the same as the first six times shown in the velocity and TKE fields, $t^* = 3.42 - 50.22$. We can see that for all $t^*$ shown the flow at low wavenumbers is anisotropic. The strain rate of the large eddies is comparable to that of the mean flow. Since the mean flow is anisotropic, $\langle u \rangle > \langle v \rangle, \langle w \rangle$, the large eddies become anisotropic. For a) and b), there appears to be some indication of isotropy for wavenumbers between, $60\,\mathrm{radm}^{-1} < k_1 < 200\,\mathrm{radm}^{-1}$, as the two spectra are nearly equal in magnitude. For an isotropic flow there exists a relationship between $E_{11}$ and $E_{33}$ in the $k_1$ direction, $E_{11}(k_1) = \frac{3}{4}E_{33}(k_1)$ (Pope, 2000). However this apparent relationship is not seen at later times, and thus we do not think this is strong evidence for isotropy within the flow.

During the regime in which surface waves are present, $t^* < 12.78$, there seems to be some evidence of an inertial subrange. As the surface waves propagate away and the coherent vortex becomes apparent within the ensemble averaged flow, the width of the subrange decreases. In d), e), and f) we see a distinct region in which the spectrum decreases less rapidly than $k^{-5/3}$ before beginning to roll off at $k_1 = 350 - 400\,\mathrm{radm}^{-1}$. These spectral "bumps" have been reported previously in the literature for both field measurements (Doron et al., 2001; Nimmo Smith et al., 2005) and in high-Reynolds number flows in the laboratory (Saddoughi and Veeravalli, 1994). The spectral bumps have been attributed to a "bottleneck" phenomenon in which the spectral flux of energy from low wavenumbers exceeds the rate of dissipation at the small scales, causing a build up of energy near the boundary between the inertial subrange and the dissipation range.

The wavenumber spectra at $x^* = 0.54$ and $x^* = 0.84$ are shown in figure IV.39 for $E_{11}$ and $E_{33}$ in the $k_3$ direction. At $t^* = 3.42$ the core of the turbulent cloud is at $x^* \approx 0.54$. For $t^* = 3.42 - 12.78$ there is a marked difference at the low wavenumbers presumably from strong vertical flows in the $k_3$ direction caused by the surface waves. We also see evidence of an inertial subrange for $t^* = 3.42$ and 12.78. The turbulent cloud is propagating to the right and thus as the flow evolves we would expect the turbulent velocity at the downstream location to be larger in magnitude for a given value of $t^* > 3.42$, since the cloud is advecting away from $x^* = 0.54$ and towards $x^* = 0.84$. We see that this is consistent with c)-f) in which the levels at $x^* = 0.84$ decay more slowly than those at $x^* = 0.54$. After the surface waves have passed, the difference in energy density near 12 rad $\mathrm{m}^{-1}$ diminishes. As time moves on the existence of a $-5/3$ spectral range becomes harder to justify. Between 200-300 rad $\mathrm{m}^{-1}$ the spectra at both locations begin to flatten out. As for the spectra in the $k_1$ direction this is thought to be caused by a buildup of energy within these scales as energy is fluxed downspectrum faster than it is dissipated.

The spectrum of $E_{11}(k_1)$ for various values of $t^*$ and $z$ are shown in figure IV.40. A large inertial subrange is present near the surface but decreases with at later times and shows evidence of an energy pileup. For $k$ within the inertial subrange an

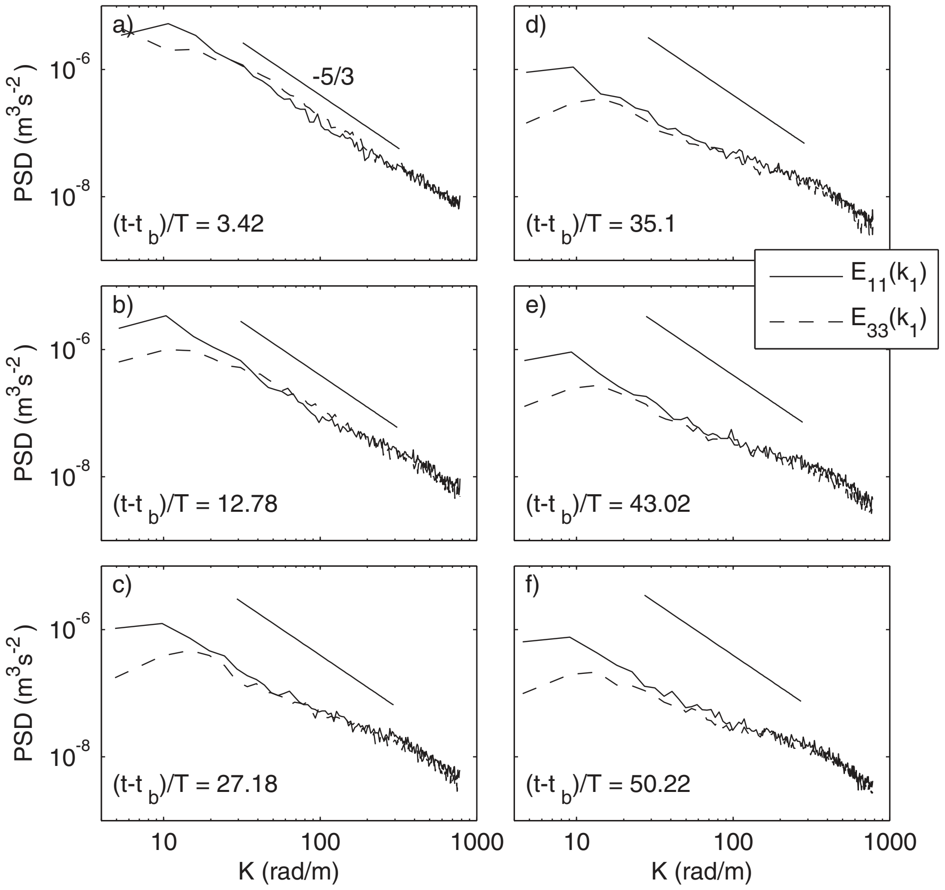

Figure IV.38: Comparison between the measured spectra, $E_{11}$, $E_{33}$ in the $k_1$ direction at $z/\lambda = -0.06$. The solid line has a slope of -5/3.

estimate of the dissipation rate can be found by

$$E_{11}(k_1) = C_1\epsilon^{2/3}k^{-\frac{5}{3}} \tag{IV.37}$$

where $\epsilon$ is the dissipation rate, and $C_1$ is a constant. We see that with depth and time the magnitude of $E_{11}$ decreases, indicating that the dissipation rate decreases as well. If the flux of energy at a given time were approximately constant across the depth of the turbulent region then we would expect to see a pileup of energy increase as we move vertically downward in the flow.

We can extend the spectra to higher wavenumbers by using wavenumber spec-

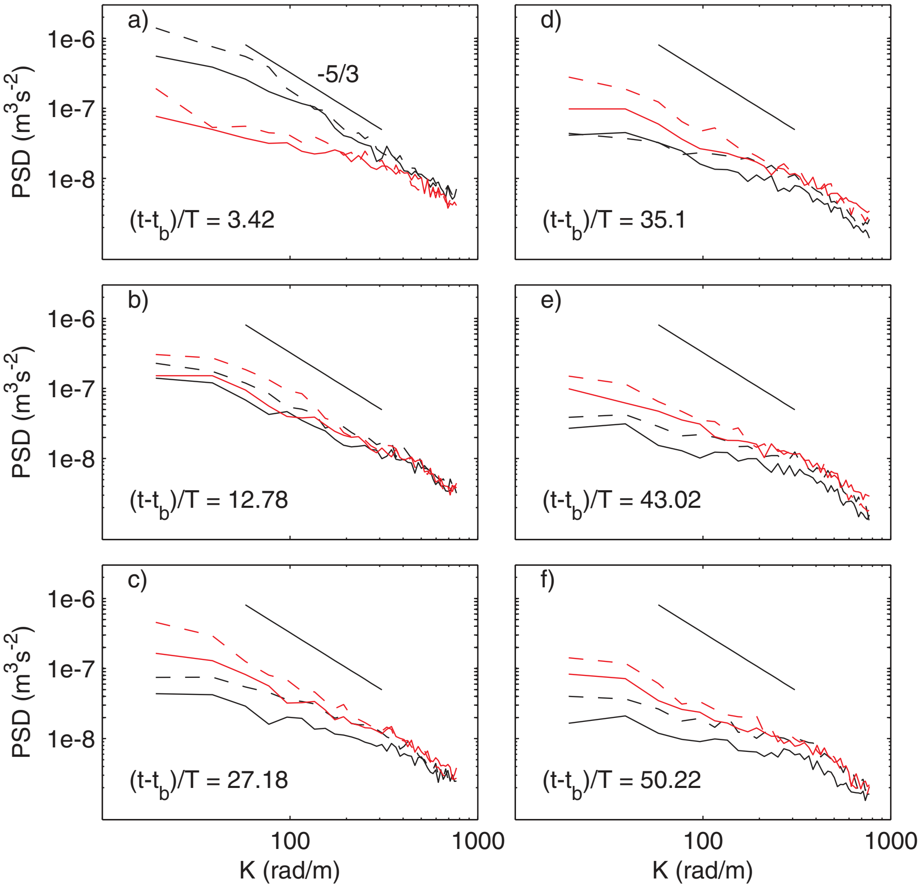

Figure IV.39: Comparison between the measured spectra, $E_{11}$ (solid) and $E_{33}$ (dashed) in the $k_3$ direction. The black lines are for a vertical slice at $x^* = 0.54$ and the red lines at $x^* = 0.84$. The solid line has a slope of $k^{-5/3}$.

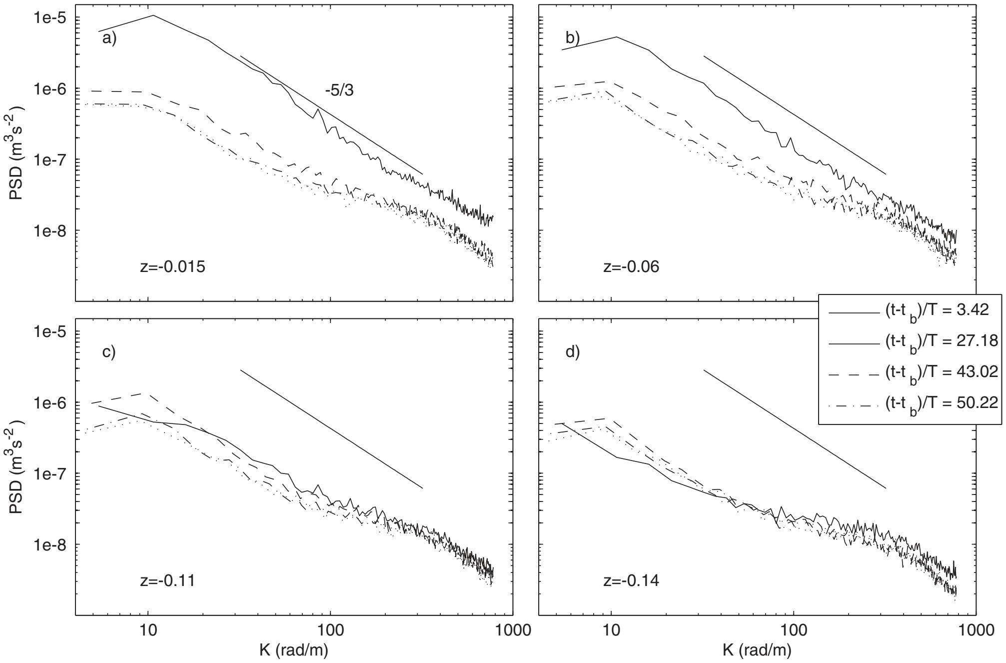

Figure IV.40: Spectra of $u$ in the $x$ direction, $E_{11}(k_1)$, for $t^*$ =[3.42, 27.18, 43.02, 58.86] at a) $z = -0.015$, b) $z = -0.06$, c) $z = -0.11$, and d) $z = -0.14$. The solid black line has a slope of -5/3 and its level is kept fixed for all four figures.

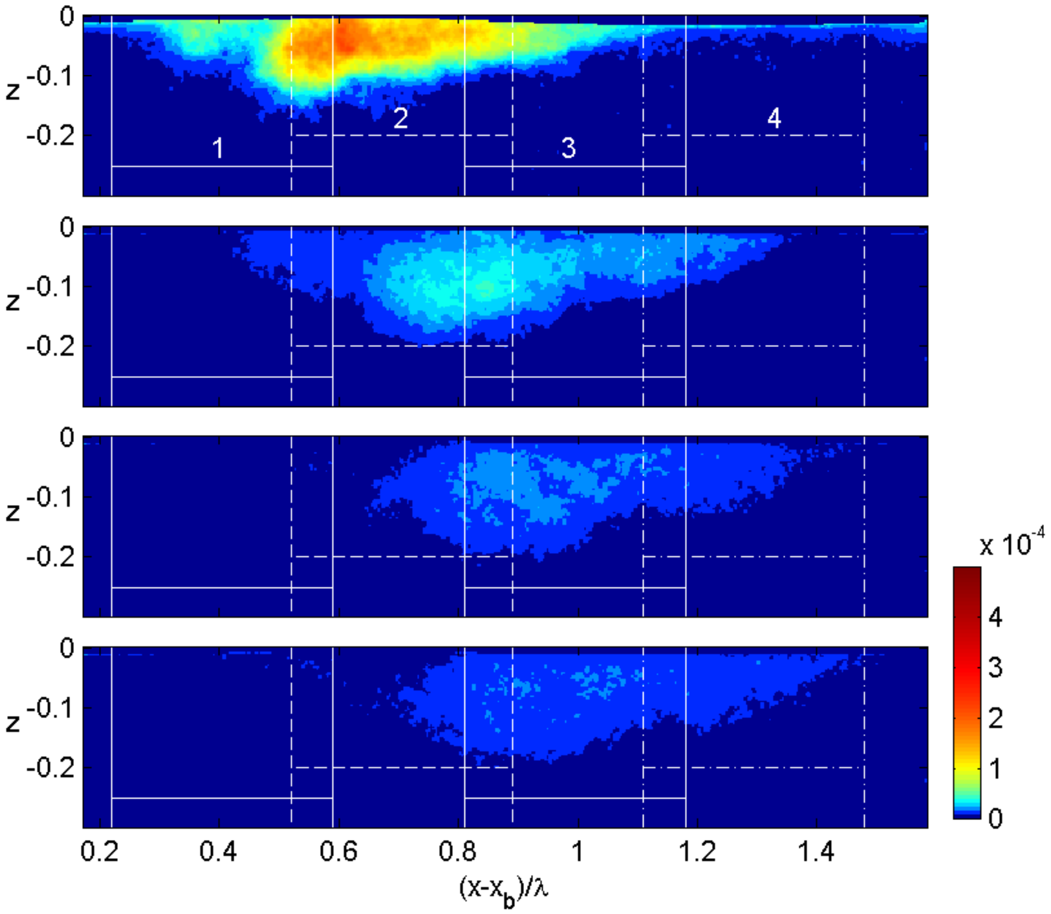

Figure IV.41: Measured TKE superimposed with the limits of the four windows used in the mosaic DPIV for $t^* = [3.42, 27.18, 43.02, 50.22]$. Due to the inhomogeneous nature of the flow, interpreting wavenumber spectra can be difficult, this figure should provide guidance. The horizontal lines help to identify the spatial extent of each window.

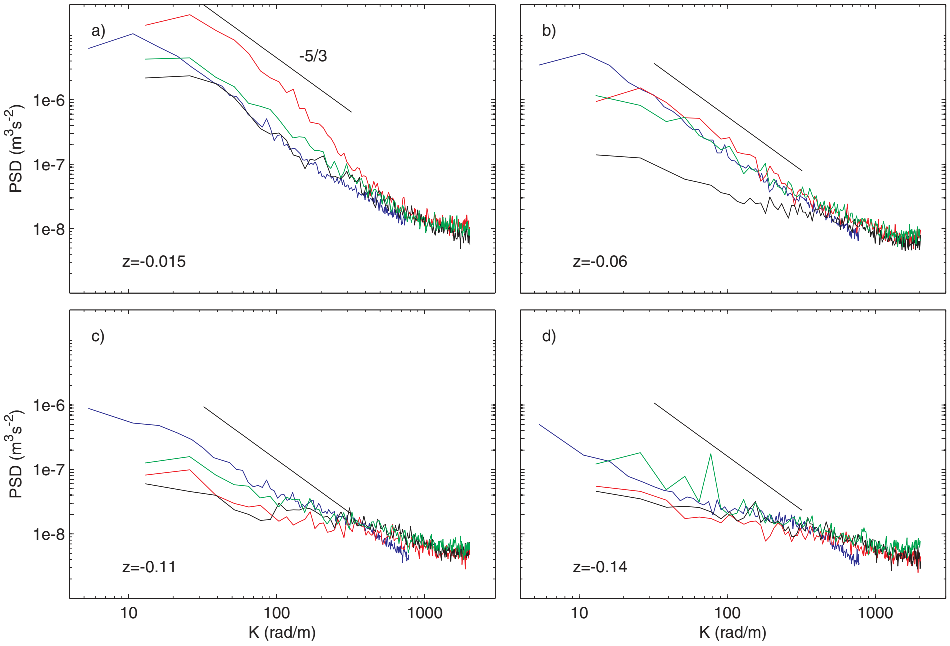

Figure IV.42: Comparison of $E_{11}(k_1)$ for both the full-field measurements and mosaic DPIV at $t^* = 3.42$. $E_{11}$ from window 1 is in green, window 2 in red, and window 3 in black. The full-field spectra are in blue. The panels correspond to four vertical locations, a) $z = -0.019$, b) $z = -0.06$, c) $z = -0.11$, and d) $z = -0.15$. The solid black line has a slope of $k^{-5/3}$

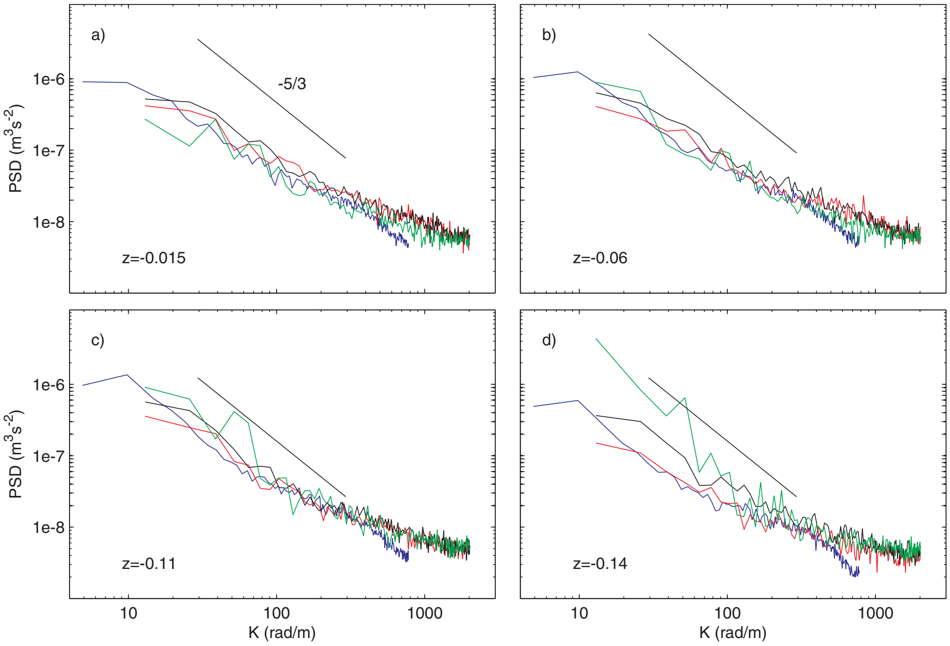

Figure IV.43: Comparison of $E_{11}(k_1)$ for both the full-field measurements and mosaic DPIV at $t^* = 27.18$. $E_{11}$ from window 1 is in green, window 2 in red, and window 3 in black. The full-field spectra are in blue. The panels correspond to four vertical locations, a) $z = -0.019$, b) $z = -0.06$, c) $z = -0.11$, and d) $z = -0.15$. The solid black line has a slope of $k^{-5/3}$

tra computed from the mosaic DPIV, which extends the Nyquist wavenumber from $k_{Ny} = 781$ rad m$^{-1}$ out to $k_{Ny} = 2026$ rad m$^{-1}$. To aid in interpreting the spectra figure IV.41 shows the TKE density for the values of $t^* = [3.42, 27.18, 43.02, 50.22]$ considered in figures IV.42 and IV.43. In figure IV.41 time increases down the page and the extent of the four subwindows are shown by vertical lines. Regardless of the horizontal location or $t^*$, none of the spectra shown in figure IV.42 or IV.43 exhibit the high wavenumber rolloff seen in the spectra from the full-field measurements. For the mosaic DPIV the magnitude of the spectra change due to the inhomogeneity of the turbulent cloud, but over all they show the same spectral shape.

## IV.5.B Compensated Spectra

The spectral bumps described earlier become more apparent when the compensated spectra are shown. The compensated spectrum for $E_{11}(k_1)$ is defined as

$$\Psi_{11}(k_1) = \epsilon^{-2/3} k^{5/3} E_{11}(k_1) \tag{IV.38}$$

with $\epsilon$ the dissipation rate per unit mass, and is plotted in figure IV.44. For each depth and time considered a $k^{-5/3}$ line is fit to the limited inertial subrange to estimate $\epsilon$. The method for estimating the dissipation rate from the wavenumber spectra will be discussed in detail in section IV.6.B. For spectra which did not exhibit an inertial subrange, $\Psi_{11}$ was not computed. The value of the Kolmogorov lengthscale, $\eta = (\nu^3/\epsilon)^{1/4}$ for each depth is computed using the estimate of $\epsilon$ from the spectra corresponding to that location. The horizontal dashed line is the value of $C_1$ (see (IV.53)) that $\Psi_{11}$ is equal to within the inertial subrange. The dominant feature of all of the spectra (excluding $t^* = 3.42$ in a) and b)) is the large hump starting at $k\eta = 0.1$ and extending out to $k\eta \approx 1$. The magnitude of the bump is consistent with that seen in the field by Nimmo Smith et al. (2005), but is larger than that seen in the laboratory (Saddoughi and Veeravalli, 1994). Near the peak, the spectrum can be seen to flatten out as $E_{11}$ begins to roll-off with an approximate $k^{-5/3}$ slope. Compensated spectra for the mosaic DPIV along with the full-field spectra at $t^* = 3.42$ are shown in figure IV.45. Only the data from window 2 are shown since at this $t^*$, window 2 has the highest amount of TKE and has a fairly homogeneous velocity field in the horizontal direction for the depths considered. At this time and depth both spectra exhibit a large inertial subrange, but we can see a rise in the high wavenumber end of $\Psi_{11}$ in both a) and b) which could be representative of the spectral bumps being extended to higher wavenumbers than seen in figure IV.40. However the spectra from the mosaic DPIV is noisier at high wavenumbers and could explain the decrease in slope from a -5/3 dependence.

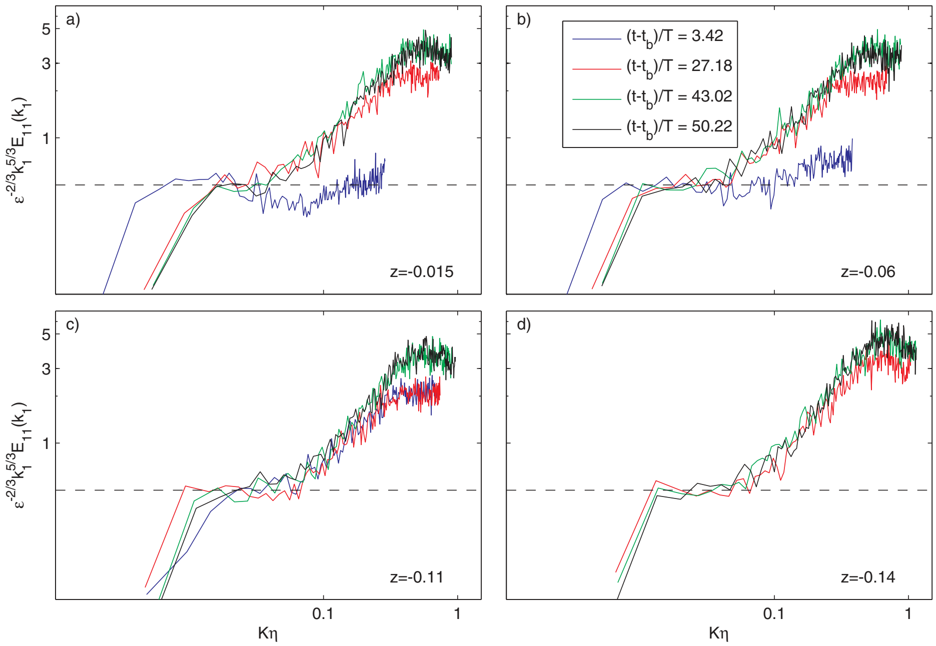

Figure IV.44: Compensated spectra, $\Psi_{11}(k_1) = \epsilon^{-2/3}k^{5/3}E_{11}(k_1)$, at a number of non-dimensional depths and times. For each compensated spectra $\epsilon$ was computed by fitting the spectra to a $-5/3$ curve within the inertial subrange. At $z = -0.14$ (Figure d), there was no evidence of an inertial subrange, so no compensated spectrum is shown. The horizontal dashed line corresponds to $C_1$, as $\Psi_{11}(k_1) = C_1$ within the inertial subrange.

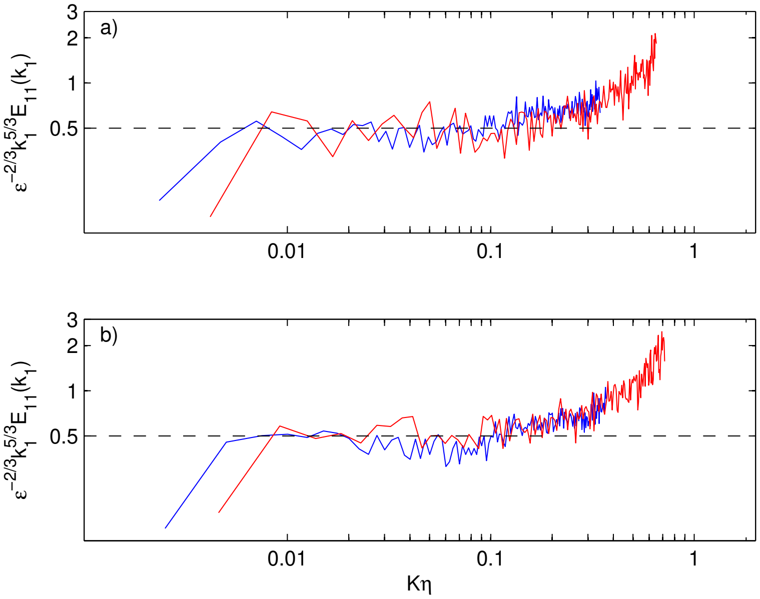

Figure IV.45: Compensated spectra, $\epsilon^{-2/3}k^{5/3}E_{11}(k_1)$, at $t^* = 3.42$. The blue line is the full-field estimate and the red is from window 2. a) is $\Psi_{11}(k_1)$ at $z = -0.015$, and b) is $\Psi_{11}$ at $z = -0.06$.

## IV.6 Turbulent Kinetic Energy Budget

The evolution of the turbulent kinetic energy density is given by

$$\begin{aligned}\frac{\partial q}{\partial t} &+ \langle u_j\rangle\frac{\partial q}{\partial x_j} \\ &= -\frac{\partial}{\partial x_j}\left(\frac{1}{\rho}\left\langle u_j p\right\rangle + \frac{1}{2}\left\langle u_i u_i u_j\right\rangle - 2\nu\left\langle u_i s_{ij}\right\rangle\right) - \left\langle u_i u_j\right\rangle S_{ij} - 2\nu\left\langle s_{ij}s_{ij}\right\rangle\end{aligned} \tag{IV.39}$$

where $q = \frac{1}{2}\langle u_i u_i\rangle$, is the TKE density (Tennekes and Lumley, 1972). The mean stain rate and the fluctuating rate of strain are given by

$$S_{ij} = \frac{1}{2}\left(\frac{\partial\langle u_i\rangle}{\partial x_j} + \frac{\partial\langle u_j\rangle}{\partial x_i}\right) \tag{IV.40}$$

$$s_{ij} = \frac{1}{2}\left(\frac{\partial u_i}{\partial x_j} + \frac{\partial u_j}{\partial x_i}\right) \tag{IV.41}$$

The first term on the left hand side of (IV.40) is the “evolution” and describes the temporal evolution of the turbulent kinetic energy density. The second term is “advection” and describes the distribution of TKE by the mean flow. The first term on the right hand side is work done on the TKE by the pressure gradient and cannot be measured by the means employed here. The next term is the “turbulent transport” and describes the transport of TKE by the turbulent velocities. The third transport term describes the transport of TKE by viscous stresses. For large Reynolds numbers the viscous transport term becomes smaller than the other transport terms and is neglected relative to them. The fourth term is the “production” term, which describes the transfer of energy between TKE and $E_m$ via the mean strain rate. The last term is the “dissipation” term and is the rate at which work is done by the viscous stresses against the fluctuating strain rate and is denoted by $\epsilon$. With the exception of the pressure term, the exclusion of the viscous transport we can evaluate almost all of the remaining terms in (IV.40).

## IV.6.A Integrated terms in the TKE budget

The dissipation term acts on scales near the Kolmogorov lengthscale, $\eta$ defined as

$$\eta = \left(\frac{\nu^3}{\epsilon}\right)^{\frac{1}{4}}. \tag{IV.42}$$

where $\nu$ is the kinematic viscosity. Estimates of $\epsilon$ yield $\eta \approx 0.4$ mm, which is an order of magnitude smaller than the resolution of our velocity estimates. Thus it will be difficult to measure $\epsilon$ directly, however we can measure $\epsilon$ indirectly. We envision a volume that entirely encompasses the turbulent cloud and on the boundaries of which both $u_i$ and $\langle u_i \rangle$ go to zero. If we take the integral of (IV.40) over this volume we obtain

$$\iiint \frac{\partial q}{\partial t}\,\mathrm{d}x\,\mathrm{d}y\,\mathrm{d}z = \iiint \left(-\left\langle u_i u_j\right\rangle \frac{\partial \langle u_i \rangle}{\partial x_j} - \epsilon\right)\mathrm{d}x\,\mathrm{d}y\,\mathrm{d}z \tag{IV.43}$$

where the transport terms and advection have integrated out. The transport terms simply redistribute the turbulence within the volume and the advection term is zero due to the boundary conditions. We can then infer the integrated $\epsilon$ from the balance of the integrated evolution and production terms,

$$\epsilon = q_t - P \tag{IV.44}$$

where $q_t$ is the evolution, $P$ the production, and $\epsilon$ the dissipation.

The locations of the intersections of the transverse and longitudinal planes at which we have all three-dimensional velocity components occur within the extent of the turbulent cloud, so the assumptions made in obtaining (IV.43) do not hold on those boundaries. At least for small times the measurements in the longitudinal plane encompass the entire turbulent cloud. So we can evaluate (IV.43) in this plane after making some assumptions about the flow due to the missing component, $v$, in the longitudinal plane. We first assume that the mean flow is two-dimensional, so $\langle v \rangle \approx 0$ and $\partial\langle\rangle/\partial y$ terms vanish. In order to describe $q$ accurately we need to account for the missing component, $v$. We have measurements of $(u, v, w)$ along the intersection of the transverse and longitudinal planes., and by comparing the averaged values of $q$ in both two and three dimensions we find that

$$q = \frac{1.53}{2}\left(u^2 + w^2\right) \tag{IV.45}$$

where $q$ is the full three-dimensional TKE density. See appendix B for further details. Using the above assumptions (IV.40) becomes

$$\text{Evolution}: \quad \frac{\partial q}{\partial t} \tag{IV.46}$$

$$\text{Advection}: \quad \langle u \rangle \frac{\partial q}{\partial x} + \langle w \rangle \frac{\partial q}{\partial z} \tag{IV.47}$$

$$\text{Production}: \quad -\langle uu \rangle \frac{\partial \langle u \rangle}{\partial x} - \langle ww \rangle \frac{\partial \langle w \rangle}{\partial z} - \langle uw \rangle \left( \frac{\partial \langle u \rangle}{\partial z} + \frac{\partial \langle w \rangle}{\partial z} \right) \tag{IV.48}$$

$$\text{Turbulent Transport}: \quad -\frac{\partial}{\partial x}\langle uq \rangle - \frac{\partial}{\partial z}\langle wq \rangle \tag{IV.49}$$

where we have not included the dissipation term, due to the difficulty in measuring it at the resolution of our experiments.

Due to the fact that measurements are taken in a plane, the volume integral is approximated by an area integral over $x$ and $z$ with a constant width. The horizontal extent of the integration is shown by the vertical white lines in figure IV.16. The vertical extent is from $z/\lambda = -0.34$ to $z/\lambda = 0.023$. The turbulent transport term is seen to be smaller than the other terms for all values, but the advection term is comparatively large for $t^* < 12.78$. This is due to large velocities induced by the surface waves as they pass through the measurement region, see figure IV.7. Despite the non-zero advection term, for completeness we will compute the inferred dissipation and later see how the magnitude of these terms compare for $3.42 \leq t^* \leq 8.46$. The inferred dissipation, $\epsilon = q_t - P$ for $t^* = 3.42 - 58.86$ is shown and is seen to be the largest magnitude term in the balance.

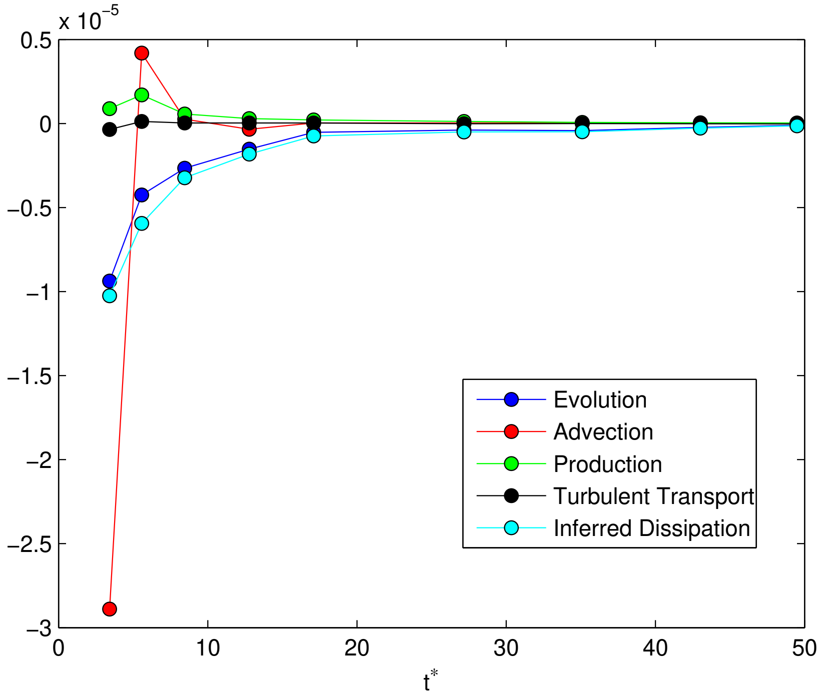

Figure IV.46: Area integrated values of selected non-dimensional terms in the turbulent kinetic energy budget. Terms shown are evolution (blue), advection (red), production (green), turbulent transport (black), and evolution - production (cyan). The initially large values of the advection term are due to the presence of surface waves within the measurement region.

## IV.6.B Dissipation measurements

We will present various methods of estimating the dissipation rate for comparison with the inferred dissipation seen in figure IV.46 assuming that the balance in (IV.43) applies.

In a given flow there exists a representative velocity, $u_0$, and length, $l_0$ which describe the motions of the energy-containing eddies of the flow. The energy contained within these eddies is transferred to smaller and smaller scales until it is ultimately dissipated by the viscosity at scales comparable to the Kolmogorov lengthscale. The energy of these eddies can be scaled as $u_0^2$, while the timescale of decay is of the order $l_0/u_0$. Within an order of magnitude the rate at which energy is dissipated is

$$\epsilon \approx \frac{u_0^3}{l_0}. \tag{IV.50}$$

Equation (IV.50) is known as the inertial estimate of the dissipation rate. The outer velocity scaling will be defined as $u_0 = u'$ where $u'$ is the rms turbulent velocity at a given depth and time,

$$u(z,t)' = \frac{1}{x_2 - x_1} \int_{x_1}^{x_2} \left\langle u(x,z,t)'^2 \right\rangle \mathrm{d}x \tag{IV.51}$$

where the limits $x_1$ and $x_2$ are shown in figure IV.16. The integral lengthscale, $L_{11}$, serves as a measure of the largest scales and is defined by (IV.29). The expression (IV.50) now yields

$$\epsilon_{IE} = \chi \frac{u'^3}{L_{11}} \tag{IV.52}$$

where $\chi$ is a coefficient determined to be 0.3 in section III.5 and $\epsilon_{IE}$ denotes the dissipation rate using the inertial estimate.

Kolmogorov's second similarity hypothesis defines a region in which the statistics of the motion is determined solely by $\epsilon$, independent of $\nu$, for sufficiently high Reynolds number (Kolmogorov, 1991; Pope, 2000). This spatial region is termed the inertial subrange and is one in which the effects of viscosity are not important and energy is simply transferred to smaller scales. In wavenumber space, dimensional analysis yields

$$E_{11}(k_1) = C_1 \epsilon^{2/3} k^{\frac{-5}{3}} \tag{IV.53}$$

where $C_1$ is a constant and has been shown experimentally to be $\approx 0.5$ (Sreenivasan, 1995). We can obtain an estimate of the dissipation rate by fitting a $-5/3$ line within the inertial subrange of the wavenumber spectra and evaluating (IV.53). The symbol $\epsilon_{SF}$ will be used to denote the spectral estimate of the dissipation rate. This estimate requires the existence of an inertial subrange, which was found in section IV.5 to decrease in width with both time and depth. The limits over which the curve was fit to a $k^{-5/3}$ line decreased accordingly. If an inertial subrange is found, this method (along with $\epsilon_{IE}$) has the advantage of being computed over scales which are well resolved by our measurements. Both $\epsilon_{IE}$ and $\epsilon_{SF}$ are integral measures of the flow and thus are averaged values across the turbulent cloud at a given depth. The horizontal extent over which these terms are computed is shown by the vertical white lines in figure IV.16, which has a constant width, $X$, for all depths at a given time. However the width of the turbulent cloud can be seen to decrease with depth. To account for this a scaling factor is applied at each depth to account for the fraction of $X$ which does not contribute to the dissipation.

$$\epsilon(z,t) = \frac{X}{X'}\epsilon'(z,t) \tag{IV.54}$$

where $X'$ is the width of the turbulent cloud at a given depth and $\epsilon'$ is the dissipation rate computed using $\epsilon_{IE}$ and $\epsilon_{SF}$. These estimates are then vertically averaged from the top to the bottom of the cloud. The inferred dissipation from the integrated production and evolution terms will be denoted $\epsilon_{PE}$. The area averaged dissipation rates are shown in figure IV.47.

The inertial estimate, the spectral estimate, and the estimate of the dissipation rate inferred from the balance of integrated production and evolution (PE balance) all agree qualitatively. The fact values of $\epsilon_{PE}$ decrease almost linearly in logspace for $t^* < 12.78$, helps to validate our estimate of $\epsilon_{PE}$ at $t^* = 3.42-5.58$, even though the advection term did not vanish at these times. For $t^* < 12.78$, $\epsilon_{IE}$, $\epsilon_{SF}$, and $\epsilon_{PE}$ all have an apparent $t^{-3/2}$ dependence. After $t^* > 12.78$, $\epsilon_{PE}$ follows a $t^{-5/2}$ dependence, while $\epsilon_{SF}$ and $\epsilon_{IE}$ decay with a $t^{-2}$ and $t^{-3/2}$ dependence respectively. This similarity between estimates is not unexpected since both the inertial estimate and the spectral estimate are based on the assumption that energy is transferred between the large scales of the flow to the small scales of the flow where it is ultimately dissipated, across a region where viscosity is not important. For the production-dissipation term we have a similar interaction since the production term feeds the turbulence via the mean rate of strain and this energy is dissipated at scales where viscosity is important.

In figure IV.25b we see that TKE has a $t^{-1/2}$ dependence for $t^* < 12.78$ and a

$t^{-1}$ dependence for $t^* > 12.78$. The total dissipation rate of TKE per unit width is given by

$$A\epsilon = \frac{\partial E_t}{\partial t} \tag{IV.55}$$

where $A$ is the area over which the dissipation is occurring and $E_t$ is the turbulent kinetic energy density. The area of the breaking region is seen to scale as $t^{1/2}$ in figure IV.33. We would then expect the dissipation rate per unit mass, $\epsilon_m$ to follow a $t^{-2}$ dependence for $t^* < 12.78$ and a $t^{-5/2}$ dependence for $t^* > 12.78$, which agrees with the decay rates seen in figure IV.47.

Using acoustical techniques Veron and Melville (1999) found a $t^n$ dependence of the dissipation rate, with $n = 1 - 1.25$. These estimates however are at a single depth and cannot be assumed to have the same dependence as our measure of $\epsilon$, especially due to the inhomogeneous nature of the turbulent cloud. RM used measures of the time-dependence of the breaking area and TKE to find that $\epsilon$ should follow a $t^{-5/2}$ dependence, which agrees with the $t^* > 12.78$ dependence of $\epsilon_{PE}$, and with the estimate provided by (IV.55).

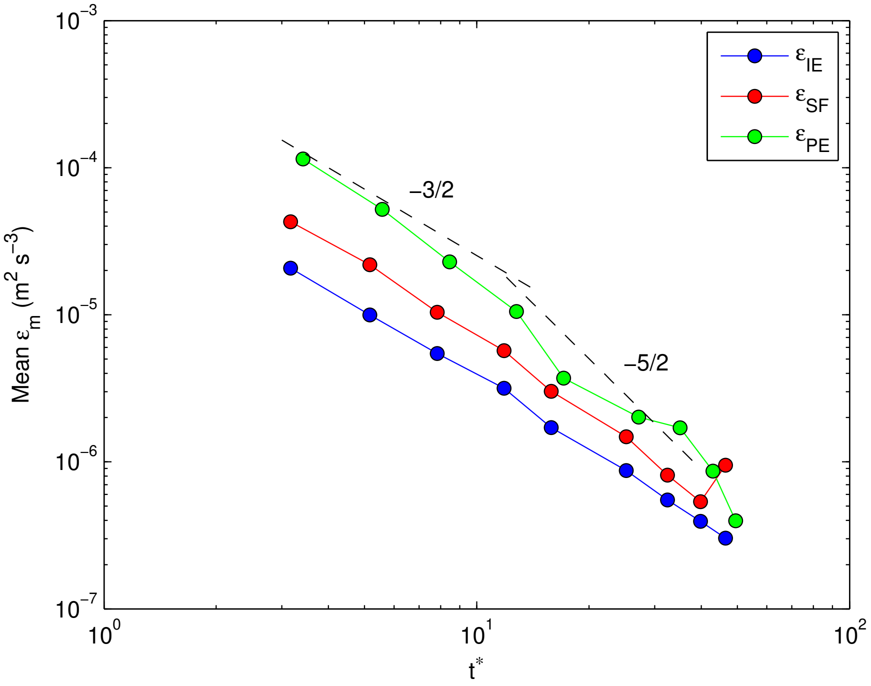

Figure IV.47: Three estimates of the average dissipation rate per unit mass, $\epsilon_m$. The methods used to compute the estimates are: $\epsilon_{IE}$, the inertial estimate of the dissipation rate, $\epsilon_{SF}$, a $k^{-5/3}$ fit to the inertial subrange of the wavenumber spectra, and $\epsilon_{PE}$, an estimate inferred from a balance between the volume integrated production and evolution terms. The dashed lines have a slope of $t^{-3/2}$ and $t^{-5/2}$ as labeled.

## IV.6.C Balances in the TKE Budget

We now revisit the TKE budget to look at relationships between the various components. We will show the evolution, advection, production, and the turbulent transport. Due to the measurement resolution the dissipation term defined as $2\nu s_{ij}s_{ij}$ cannot be directly measured.

The measurements in the longitudinal plane encompass the entire turbulent cloud and thus will be used to present horizontally integrated terms in the TKE budget. The horizontal extent of the integration is shown by the vertical white lines in figure IV.16. The assumptions made in section IV.6.A are applied here in order to approximate the terms in the TKE budget. We assume that the flow is two-dimensional in the mean which yields $\langle v \rangle = 0$ and $\partial \langle \rangle / \partial y = 0$. We will also use a scaling factor to account for the missing component, $v$, in the TKE density, see appendix B for further details. Equations (IV.46)-(IV.49) show the results of these assumptions for the terms in the TKE budget that we can measure.

Despite the large number of experimental repeats in the longitudinal plane, at later times the signals are still quite noisy. This is due to the lower signal to noise from the DPIV measurements as the magnitude of the flow velocity decreases. Of the terms shown the turbulent transport term is the noisiest, due to it being the derivative of a third-order correlation. In order to separate the noise from the signal we first compute the vertical wavenumber spectrum of the horizontally integrated turbulent transport term from $z/\lambda = -0.44$ to $z/\lambda = -0.25$. In this region the signal is entirely noise, i.e. it lies outside of the turbulent cloud. The temporally averaged spectrum, from $t^* = 1.26{-}57.42$ is shown in figure IV.48.

A separation between the low-wavenumber end of the spectrum and the high-wavenumber regime is seen to occur at $K_z = 130$ rad m$^{-1}$. We then low-pass filter the horizontally integrated terms in the TKE budget using a running-mean filter of width, $z/\lambda = 0.036$, which corresponds to $K_z = 130$ rad m$^{-1}$.

The presence of surface waves within the measurement region complicate the computation of these terms. This is particularly true for the evolution term, since the absolute location of the turbulent cloud changes with the free surface as the waves pass. To simplify the comparisons the horizontal integrals are cutoff at a depth corresponding to the lowest point in the free surface at a given value of $t^*$.

The horizontally integrated evolution, advection, production, and turbulent transport are shown in figures IV.49 and IV.50 for $t^* = [3.42, 5.58, 8.46]$ and $t^* = [12.78, 17.10, 27.18]$. We can see that at $t^* = 3.42$ the advection term dominates, and is due to the large vertical velocity associated with the surface waves at this time, see figure IV.7. By $t^* = 5.58$ we see that the advection term has changed sign due to the surface wave induced velocity, but the remaining terms in the budget are now of the same magnitude. For the terms shown, there seems to be a balance between the evo-

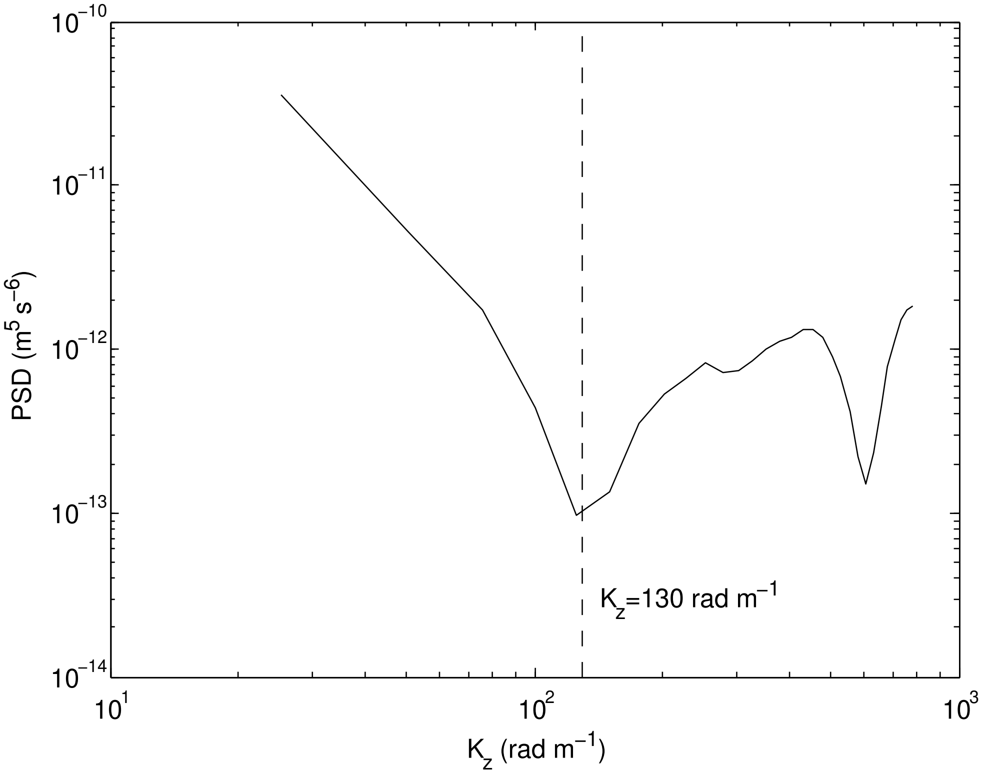

Figure IV.48: Vertical wavenumber spectrum of the horizontally averaged turbulent transport term, computed from $z/\lambda = -0.44$ to $z/\lambda = -0.25$. The spectrum shown was temporally averaged from $t^* = 1.26 - 57.42$. The spectrum can be seen to begin to show a clear delineation between the low-wavenumber and high-wavenumber regimes at $K_z = 130$ rad m$^{-1}$.

lution and advection terms as well as between the production and turbulent transport terms. There is also a predominately negative transport due to the turbulence near the surface, which becomes positive at depth. We see similar results for $t^* = 8.46$, but with the advection term again having changed sign near the surface, but remaining positive at depth. The approximately constant value of the evolution term below $z/\lambda$ is attributed to the presence of a long wave in the tank generated by the breaking process. A similar result is seen for $t^* = 17.10$, and is consistent with a long wave propagating upstream and reflecting off of the wave paddle.

For $t^* > 12.78$ we see similar profiles, with the advection term decreasing significantly as the surface waves leave the measurement region. The production term also decreases and the evolution and transport terms are the remaining dominant terms. This suggests that perhaps after breaking the main exchange of energy to the turbulence is through the surface waves, and that the coherent vortex simply slowly propagates the turbulent cloud downstream. Further knowledge of the dissipation rate would help to further understand the dynamics of the turbulent cloud. The ability to model such a flow as seen here could also lead to an understanding of the size and role of the pressure transport term in the balance, and also help to validate the relative magnitude of the terms seen here.

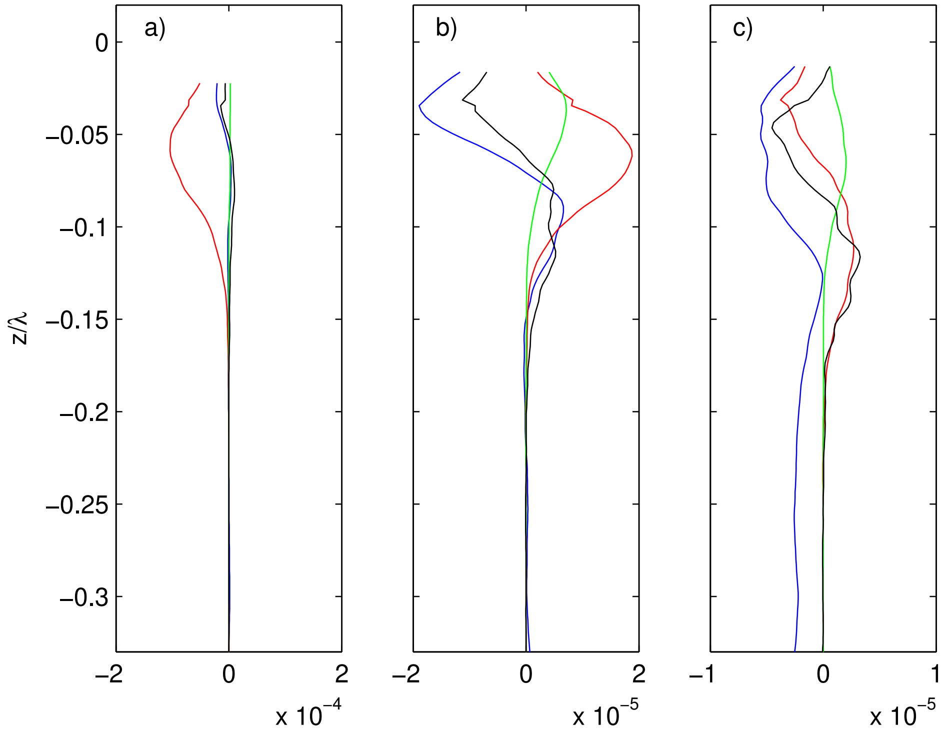

Figure IV.49: Horizontal integrals of non-dimensional terms in the TKE budget in the longitudinal plane for a) $t^* = 3.42$, b) $t^* = 5.58$, and c) $t^* = 8.46$. The assumptions outlined in (IV.46)-(IV.49) were used to estimate the quantities shown. The terms shown are evolution (blue), advection (red), production (green), and turbulent transport (black). Note the change in horizontal scale between each subfigure.

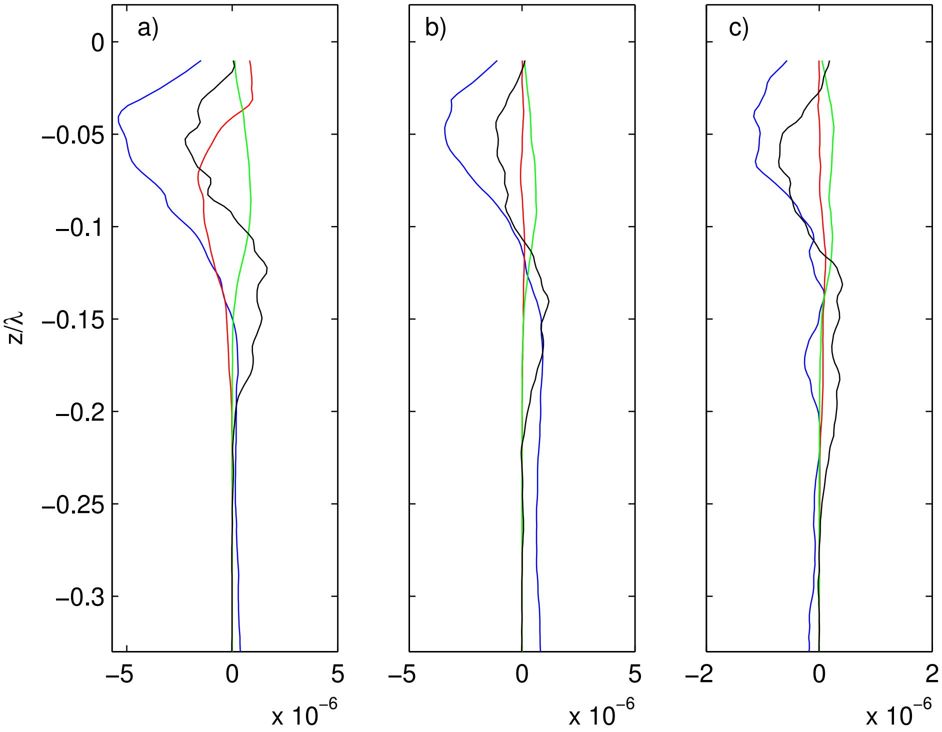

Figure IV.50: Horizontal integrals of non-dimensional terms in the TKE budget in the longitudinal plane for a) $t^* = 12.78$, b) $t^* = 17.10$, and c) $t^* = 27.18$. The assumptions outlined in (IV.46)-(**??**) were used to estimate the quantities shown. The terms shown are evolution (blue), advection (red), production (green), and turbulent transport (black). Note the change in horizontal scale between each subfigure.

These measurements contrast with Chang and Liu (1999) who studied quasi-periodic breaking using DPIV in a sheet along the centerline of a wave tank, the longitudinal plane. In order to account for $v$, a scaling factor derived from shear flows was used (Svendsen, 1987)

$$k = \frac{1.33}{2}\left\langle u'^2 + w'^2 \right\rangle . \tag{IV.56}$$

Chang and Liu (1999) found an apparent balance between advection, production, and dissipation within a few wave periods. Their estimate of the dissipation rate was computed in the same way as our residual value, while ignoring pressure transport relative to turbulent transport. A control volume beneath the trough of a wave was used to compute the various components of the TKE budget. For each run 10 waves were used, and the experimental data was collected between the third and fourth breaking event. The nature of breaking considered is quite different from the case we have investigated, due to the depth of the water and the quasi-periodic nature of the breaking which could also account for the increased role of the advection term.

In their stochastic model of breaking Sullivan et al. (2004) presented terms in the turbulent kinetic energy budget for Couette flow, shear-driven flow, as well as flow driven entirely by breaking. The estimates of the energy budget terms show a distinct difference from those obtained by Chang and Liu (1999). Consistent with our findings, the turbulent transport term dominates near the surface. Additionally they find that the pressure transport term is of the same order of magnitude as production. While some of these similarities support our findings it is important to note that the flow is qualitatively different from what we measured in the laboratory, due to the fact that their results are based on multiple three-dimensional breaking events across the computational domain while we have a single two-dimensional breaking wave.

As an appendix to their paper on laboratory measurements, MVW presented tentative estimates of the terms in the TKE budget. Similar to Chang and Liu (1999), MVW used an approximation to for $v$ to account for the unmeasured out-of-plane velocity using

$$k = \frac{1.5}{2}\left\langle u'^2 + w'^2 \right\rangle \tag{IV.57}$$

which assumes that $v^2 = (u^2 + w^2)/2$. To account for the dissipation rate the isotropic estimate

$$\epsilon = 15\nu\left\langle \left(\frac{\partial u}{\partial x}\right)^2 \right\rangle \tag{IV.58}$$

was used. These terms were then averaged horizontally and the results implied an apparent balance between the advection and the transport terms, but the shape of the terms does compare well with the measurements shown in figures IV.49 and IV.50.

## IV.7 Discussion

### IV.7.A Spectral bumps

The wavenumber spectra in both the $k_1$ and $k_3$ directions exhibit a feature in which a bump appears where the spectrum falls off slower than $k^{-\frac{5}{3}}$ for wavenumbers higher than the apparent inertial subrange. These bumps have been seen previously in both the field and in the laboratory, using a variety of measurement techniques, thus we do not feel it is an artifact of the processing or another source of noise. The feature persists when we extend the cutoff wavenumber from $\approx 700$ rad m$^{-1}$ to $\approx 2000$ rad m$^{-1}$. The thought is that there is a build up of energy in scales near the boundary between the inertial subrange and the dissipation range. The cause of this build up is thought to be caused by an inability of the flow to dissipate energy faster than the rate at which energy is fluxed down from the larger scales.

Figure IV.40 shows wavenumber spectra for four depths and values of $t^*$. For times close to breaking, $t^* \approx 5$, and near the surface, a large inertial subrange is seen which extends all the way up to 500 rad m$^{-1}$. As either $t^*$ or $z$ increase the existence of a region in which energy is piling up becomes more pronounced. We see from figure IV.51 that the dissipation decreases in magnitude with depth. At a given location if the energy flux at the large scales is nearly constant with depth, or at least decaying slower than $\epsilon$, then a decreasing $\epsilon$ should bring about this pileup.

The balance of the volume-integrated TKE budget yields an inferred measure of the dissipation rate. The inverse timescale of these terms is shown in figure IV.52 for $q_t/q, P/q, (q_t - P)/q$ where $q_t$ is the evolution term, $P$ the production term, and $q$ the TKE density. For $t^* < 8.46$ the surface-wave induced velocities do not go to zero at the edges of the boundary and thus a strict balance between evolution, production, and dissipation does not apply. However for $t^* > 8.46$, both the integrated turbulent transport and advection terms become small, validating the assumption made. The inverse timescale of the inferred dissipation is larger than both evolution and production for all values of $t^*$, as we would expect from comparison with the integrated terms in

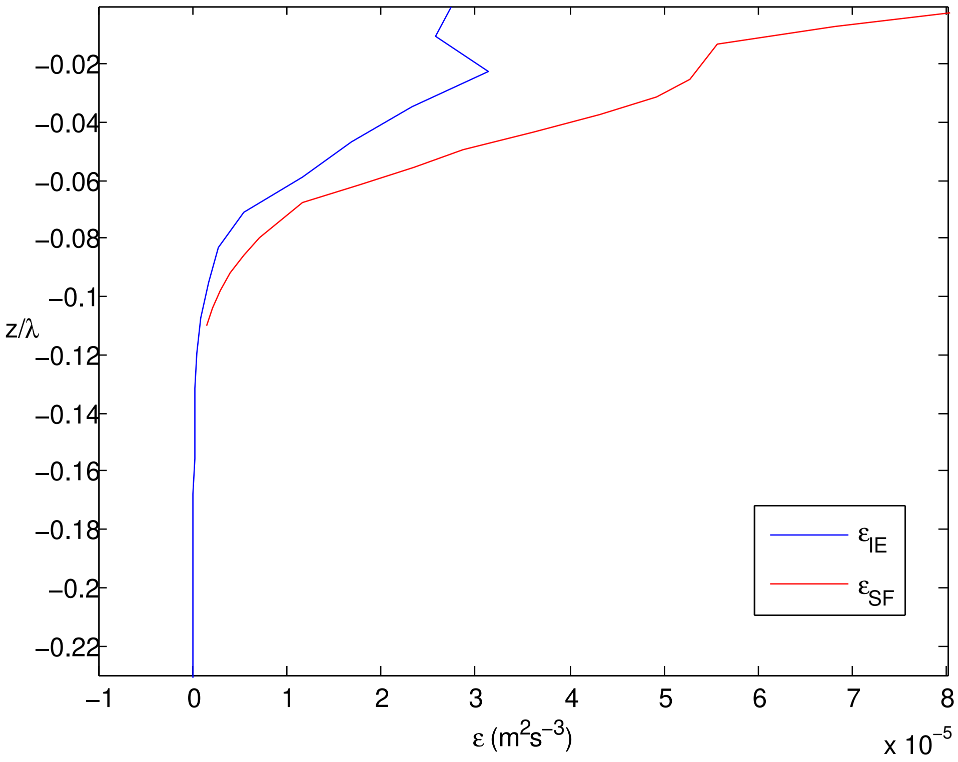

Figure IV.51: The horizontally averaged dissipation rate as a function of $z/\lambda$ for $t^* = 3.42$. $\epsilon_{IE}$ is the inertial subrange estimate and $\epsilon_{SF}$ is the fit to the inertial subrange.

the TKE budget, figure IV.46. We do not see any point at which the rate of production exceeds that of the dissipation which would support the idea of an energy pileup, since the production term describes the transfer of energy from the ensemble averaged flow to the turbulence. This accumulation of energy seen in the wavenumber spectra could be a more local phenomenon which is concentrated spatially on a small scale, which in turn could contribute little overall when integrated and not become apparent in these area-integrated terms.

### IV.7.B Estimation of the breaking parameter, *b*

Phillips (1985) proposed a statistical description of breaking based on the dis-

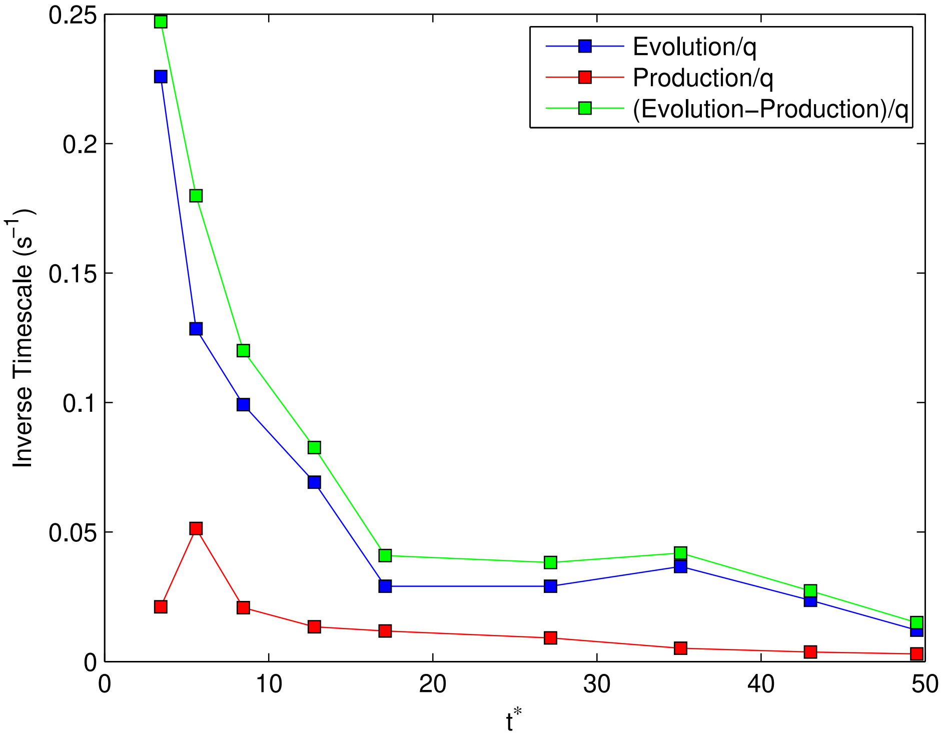

Figure IV.52: The magnitude of the inverse timescale of the production and evolution from the area integrated TKE budget, see (IV.43). The magnitude of the inverse timescale of inferred dissipation from the balance of evolution and production is also shown.

tribution of breaking fronts per unit area of ocean surface. He then defined the average rate of energy loss for breaking waves with velocities in the range ($\mathbf{c}, \mathbf{c} + \mathrm{d}\mathbf{c}$) to be

$$\epsilon(\mathbf{c})\,\mathrm{d}\mathbf{c} = b\rho g^{-1} c^5 \Lambda(\mathbf{c})\,\mathrm{d}\mathbf{c}. \tag{IV.59}$$

Here $\Lambda(\mathbf{c})$ is a distribution of breaking fronts on the ocean surface where $\Lambda(\mathbf{c})\mathrm{d}\mathbf{c}$ is the average total length of breaking fronts per unit surface area, and $b$ is the breaking parameter which was shown in Chapter III to be strongly dependent on the slope of the breaking wave. MVW used their measurements of the Reynolds stress to estimate the breaking parameter, $b$. We wish to use the results of section IV.3.C to estimate $b$ following MVW and then compare the result with that found in Chapter III.

MVW stated that the total amount of momentum transported vertically by the breaking event per unit area of whitecap is given by

$$M = \int_0^{\tau_t} \rho_w \overline{uw}\,\mathrm{d}t, \tag{IV.60}$$

$$= \tau_t \rho_w [\overline{uw}], \tag{IV.61}$$

where $M$ is the momentum, $\rho_w$ the density of water, $\tau_t$ the decay timescale of the turbulence, $\overline{uw}$ is the horizontal average of the Reynolds stress in the longitudinal plane, and where the square brackets represent a time average. Using Phillips' distribution the area swept out by breaking per unit area is given by $c\tau_b\Lambda(c)\,\mathrm{d}c$, where $\tau_b$ is the time of active breaking during which momentum is transferred from the surface waves to the fluid. Thus the distribution of momentum flux is

$$I(c)\,\mathrm{d}c = \frac{\tau_t}{\tau_b}\rho_w[\overline{uw}]\tau_b c\Lambda(c)\,\mathrm{d}c. \tag{IV.62}$$

MVW then used $\tau_b \approx 2\pi C_c/g$, $\tau_t = \mathcal{J}\tau_b$, and $c = 0.8C_c$, where $C_c$ is the phase speed of the wave, $c$ is the speed of the advancing front, and $\mathcal{J}$ is a numerical factor. We have shown in figure IV.32, that the speed of the advancing wave front for the breaking wave considered here is given by $c = 0.67C_c$, as opposed to $0.7 - 0.8C_c$ found by RM. These values were then combined with (IV.62) to yield

$$I(c)\,\mathrm{d}c = \mathcal{J}\frac{2\pi}{(0.67)^3 g}\frac{\rho_w[\overline{uw}]}{C_c^2}c^4\Lambda(c)\,\mathrm{d}c \tag{IV.63}$$

Since the wave energy and momentum densities are related by $M = C_c^{-1}E$, use of (IV.59) yields an estimate of $b$ from (IV.63),

$$b = \mathcal{J}\frac{2\pi}{(0.67)^3}\frac{[\overline{uw}]}{C^2} \tag{IV.64}$$

An estimate of $[\overline{uw}]$ is computed from a time-series at fixed $z$ corresponding to the depth of maximum $\overline{uw}$ for $t^* = 3.42$, $z = -0.03$. The time spacing of the data presented is irregular so we will fit a line to $\overline{uw}$ and use this to compute the time average. We find $b = 0.0147$ which agrees within a factor of two with the estimate as measured in Chapter III for the wave packet considered, $b = 0.0219$. In section III.2.C we derived a model of $b$ based on the inertial estimate of breaking,

$$b = \chi 2^{\frac{3}{2}} h k_c^{\frac{5}{2}} \tag{IV.65}$$

where $\chi$ is a constant and $hk_c$ is the slope based on the height the wave plunges, see figure III.2. For plunging breaking waves, $\chi$ was measured to be 0.3 and $hk_c$ for the wave packet considered in these DPIV measurements was 0.21. The value of $b$ predicted by the model using (IV.65) is then 0.0171, as compared to $b = 0.0147$ as measured using (IV.64).

## IV.8 Conclusions

We have presented measurements of the large-scale turbulent structure of breaking waves in the laboratory using DPIV in both the streamwise and cross-stream directions.

The large coherent vortex seen by RM and MVW is again seen here, but with sufficient spatial scale to image the whole vortex at once. By separating out the velocity field induced by the surface waves we see that the large vortex becomes apparent up to seven wave periods earlier.

The initial formation of the breaking region is quite rapid. The depth of the ensemble-averaged mixed region is seen to follow a $x^{1/2}$ dependence and permits the the measurement of an eddy viscosity, $\nu_T$.

The turbulent kinetic energy density is seen to follow a $t^{-1/2}$ dependence for times while the surface waves are present, and then begins to decay faster for $t^* > 12.78$. The advection term is significant for $t^* \leq 17.10$ and is the dominant term at $t^* = 3.42$, due to the surface-wave induced velocities. The turbulent transport and evolution terms is seen to be significant for $t^* \geq 5.58$, while production is significant for $5.58 < t^* < 17.10$ and decreases in magnitude but is still non-zero for later times.

The wavenumber spectra exhibit an inertial subrange near the surface for small $t^*$. A region in which the spectra become less steep leads to the formation of a bump in the compensated spectra. The formation of this bump seems to be consistent with an imbalance between the energy flux from the large scales and the viscous dissipation rate.

The experimental configuration allows us to measure all three components of $u_i$ at four vertical locations within the flow. Comparison of TKE using both $(u, w)$ and $(u, v, w)$ have shown that $q = 1.53q'$ where $q'$ is TKE in the longitudinal plane and $q$ is the full three-dimensional TKE.

While the dissipation rate, $\epsilon = 2\nu s_{ij}s_{ij}$, could not be directly measured we can infer a value from an implied balance of evolution $(q_t)$, production $(P)$, and dissipation $(\epsilon)$ in the volume integrated TKE budget. Comparison of the inferred dissipation, $\epsilon = q_t - P$ with integral measures of the dissipation rate using inertial and spectral estimates show good agreement.

The breaking parameter discussed at length in Chapter III was estimated from the distribution of momentum flux using the Reynolds stress in figure IV.20 using the methodology proposed by MVW. For the experimental data shown here $b = 0.0147$, while $b$ measured in Chapter III was found to be $b = 0.0219$. However the model of the plunging wave event developed in Chapter III finds $b = 0.0178$. Small errors in estimating the speed of the advancing front, can become significant when estimating $b$, and could account for some of the variability found.

# Appendix A

# Wave packet generation and experimental setup

This appendix describes the theory and methodology of generating breaking wave packets for the experiments described in Chapters IV and III. The construction and application of the wavemaker transfer function, the settling time of the tank, and the experimental setup are also described.

## A.1 Packet generation

The technique used for the generation of a breaking wave packet is based on a method initially proposed by Longuet-Higgins (1974) and subsequently used by Rapp and Melville (1990) and others. In this method a packet of waves of varying frequency are generated in a tank such that the phases add at the desired focal point and generate a breaking event. For completeness we outline the details on the generation of the wave packet as given by Rapp and Melville (1990). We describe the free surface displacement as

$$\eta(x,t) = \sum_{n=1}^{N} a_n \cos(k_n x - \sigma_n t - \phi_n) \qquad \text{(A.1)}$$

where $a_n$ is the amplitude of the $n$th component, $k_n$ is the wavenumber, $\sigma_n = 2\pi f_n$ the angular frequency, $\phi_n$ the phase, and $N$ the total number of frequency components. The dispersion relationship relates $\sigma_n$ to $k_n$,

$$\sigma_n = gk_n \tanh(k_n d) \tag{A.2}$$

where $d$ is the depth of the water and $g$ is the gravitational constant. Since we wish the packet to focus at a location $(x_b, t_b)$ we can adjust the phases such that

$$\cos(k_n x_b - \sigma_n t_b - \phi_n) = 1 \tag{A.3}$$

We then re-arrange (A.3) to get

$$\phi_n = k_n x_b - \sigma_n t_n + 2\pi m \tag{A.4}$$

with $m = (0, \pm 1, \pm 2, \ldots)$. We can then substitute (A.4) into (A.1) and $\eta(x, t)$ becomes

$$\eta(x, t) = \sum_{n=1}^{N} a_n \cos[k_n(x - x_b) - \sigma_n(t - t_b)] \tag{A.5}$$

We wish to express the surface displacement at the paddle, whose mean location will be defined as $x = 0$. Thus, (A.5) becomes

$$\eta(0, t) = \sum_{n=1}^{N} a_n \cos[-k_n x_b - \sigma_n(t - t_b)] \tag{A.6}$$

In order to simplify the frequency spectrum, Rapp and Melville (1990) set $a_n$ to be constant. We will adjust the $a_n$ to keep the slope of each component, $a_n k_n$, constant so that the contribution to the energy spectrum would be equal for each component, a technique used by Loewen and Melville (1991), Lamarre and Melville (1991), and Melville et al. (2002). A measure of the strength of breaking is given by

$$S = \sum a_n k_n \tag{A.7}$$

which we will call the input slope, and it represents the maximum slope as defined by linear theory.

The dimensional analysis outlined in Rapp and Melville (1990) states that the functional relationship and parametric dependence of the surface displacement for the wave packet is

$$\eta k_c = \eta k_c(x k_c, t f_c; a k_c, \Delta f / f_c, x_b k_c) \tag{A.8}$$

Here $f_c, k_c$ are the center wavenumber and frequency components of the wave packet and $\Delta f/f_c$ is the normalized range of frequencies used in generating the wave packet. To generate the packet the theoretical surface elevation at the breaking location is calculated using (A.5). The intersection of the lines in the $x-t$ plane that correspond to the group velocities of the high and low frequency limits of the packet defines the theoretical breaking location, $(x_b, t_b)$. These group velocity lines are extended back to the origin to obtain the width of the generated signal in time. The signal is then windowed using a tapered cosine window on the first and last 10% of the signal. The window, $y$, is given by

$$y_i = \begin{cases} \frac{1}{2}\left(1 - cos\left(\frac{2\pi i}{n}\right)\right) & \begin{array}{l}\text{for i = 0, 1, ..., m - 1} \\ \text{for i = n - m, n - m + 1, ..., n - 1}\end{array} \\ 1 & \text{elsewhere} \end{cases} \tag{A.9}$$

where $n$ is the number of points and $m = n/10$.

## A.1.A Transfer Function

In order to accurately reproduce a given surface profile the transfer function of the computer-wave-maker system needs to be measured. The system can be thought of as a black box and be described in the following manner.

$$\eta(0,t) = v(t) * h(t) \tag{A.10}$$

$$\hat{\eta}(0,f) = \hat{V}(f)\hat{H}(f) \tag{A.11}$$

$$\tag{A.12}$$

Here the $v(t)$ is the voltage signal being applied to the wavemaker and $h(t)$ is the transfer function, $*$ denotes a convolution and $\hat{V}(f), \hat{H}(f)$ the Fourier transform of the voltage and the transfer function.

To measure the phase and the amplitude of the transfer function,

$$H(f) = |H(f)|e^{-i\phi(f)} \tag{A.13}$$

a number of small-amplitude sine waves were generated over the range of frequencies encountered in the experiments, $f = 0.4$Hz-2.0Hz. Measurements were taken at three distances from the wave paddle, $x = [2.15\,\mathrm{m}, 4.17\,\mathrm{m}, 10.94\,\mathrm{m}]$. The first of these distances was chosen to lie outside of the range of evanescent waves generated at the paddle Dean and Dalrymple (1991). The hydraulic system was warmed up and waves with an amplitude of 0.2 V were recorded for 70 s. The start of the signal was modulated through a hyperbolic tangent profile to minimize the Fresnel envelope associated with an impulsive start (Longuet-Higgins, 1974). The amplitude and phase change for each frequency was then calculated after the maximum wave amplitude was reached and the phase of each component was extrapolated back to the wave paddle. A third order polynomial fit was applied to the amplitude data and a quadratic fit to the linear data was used. The amplitude and phase of this measured transfer function is plotted in figure (A.1) and is given by

$$|H(f)| = -0.13f^3 - 0.96f^2 + 4.22f - 0.70 \tag{A.14}$$

$$\Delta\Phi = 1.32f^2 - 3.36f + 3.36 \tag{A.15}$$

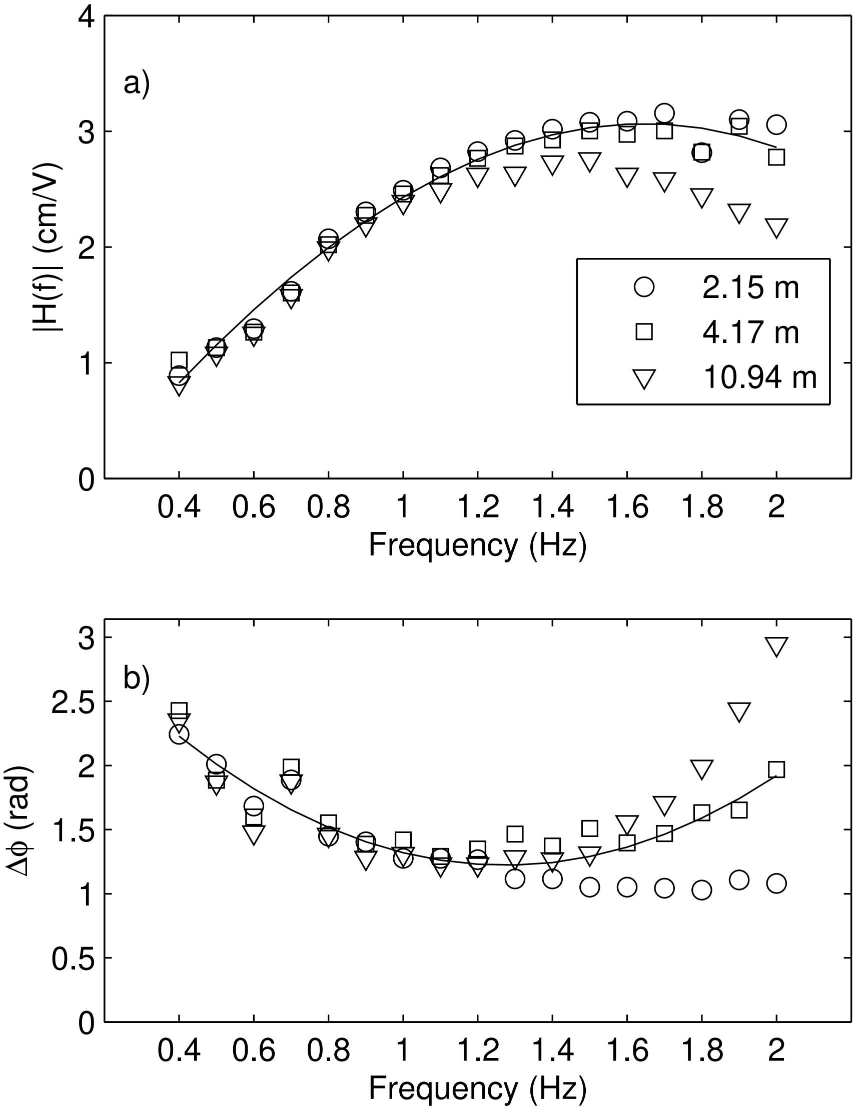

Figure A.1: Plot of the a) amplitude, and b) phase of the transfer function. The symbols are data from the three wave gauges used in the measurement of the transfer function.

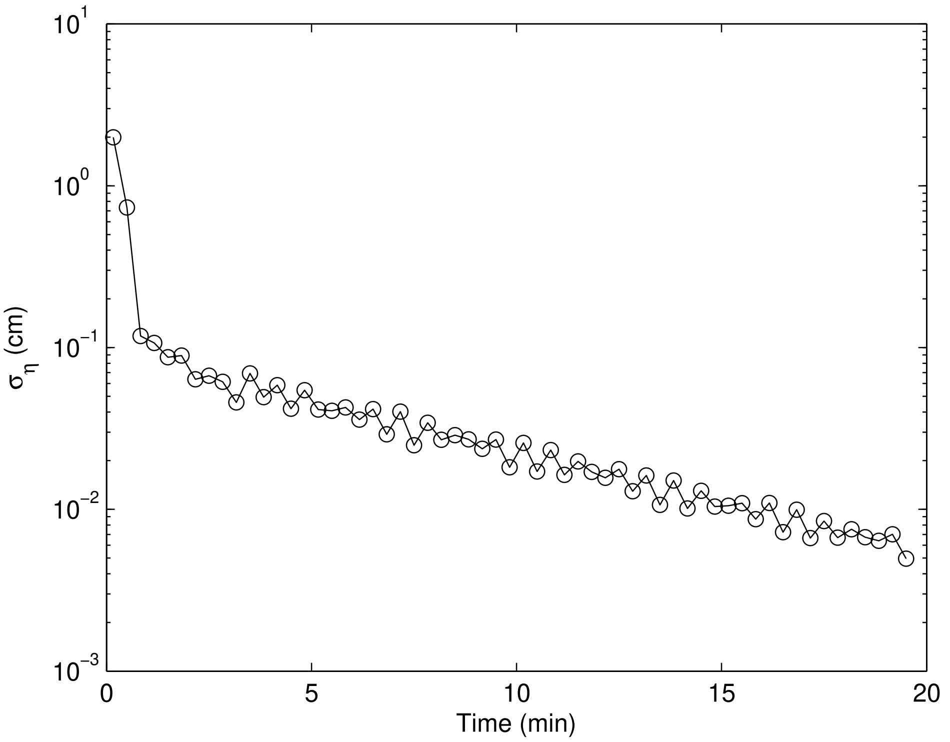

Figure A.2: Standard deviation of the surface elevation measured every 20s for 20 min. $t = 0$ is the time of the breaking event.

### A.1.B Settling Time

In order to assure repeatability between repeats of a breaking event the energy in the tank needs to be allowed to dissipate. The horsehair covered beach at the far end of the wave tank helps to reduce the energy within the tank. To quantify the rate at which the tank settles a wave gauge was placed in the tank and surface elevations were recorded for 20 min after breaking. The standard deviation over a subset of 20s is plotted as a function of time in figure A.2. The time between repeats for the experiments in Chapters III and IV was 10 minutes after which the standard deviation of the surface elevation is at 0.22 mm.

### A.1.C Experimental setup in Chapters III and IV

The layout of the setup for the experiments described in Chapters III and IV is shown in figure A.3. For the experiments in III only the lines labeled 5 and 6 were used. The data acquisition computer handled all of the input and output of analog signals and a LabView Virtual Instrument (VI) was written to run without user interaction. The wave gauge calibration procedure consisted of displacing the gauge by increments of 2 cm over a ±10 cm range. The gauge was held fixed at a given depth for 5 s in the quiescent tank and an average value calculated. A 3rd order polynomial fit of the data to the A/D range (±10 V) of the card was used for calibration. At the start of every run before the paddle was started, 10 s of quiescent data was collected for use in removal of the DC level from the measurement. The period of the lowest mode of the tank is given by

$$T = \frac{2L}{\sqrt{gH}} \tag{A.16}$$

where $L$ is the length of the tank and $H$ the water depth. The period for this tank is 24s, which is larger than the 10s delay at the start, but after 10 minutes the variability induced by this mode should be small.

A sample output of the calibration procedure is shown in figure A.4.

For the experiments in Chapter IV the analog instrumentation was the same as in Chapter III. The DPIV system was built around a commercially available DPIV package called PixelFlow from Viosense Corporation. The PIV computer controls the laser signal timing as well as records the video imagery to a pair of SCSI disks. The D/A computer controls the analog input and output needed for the set of experiments. A LabView program was written to synchronize the start of the wave paddle with the recording of the wave gauge signals. In a continuous run mode the camera outputs a TTL compatible frame-enable signal corresponding to the output of a frame (line 1) and this signal was used as the timebase for the DPIV measurements. This TTL signal is then processed by the DPIV software to generate timing signals for the two laser heads based on the desired $\Delta t$ of the system (line 3). The laser outputs a sync signal approximately 130 ns before outputting a laser pulse. This sync signal is fed to the D/A computer (line

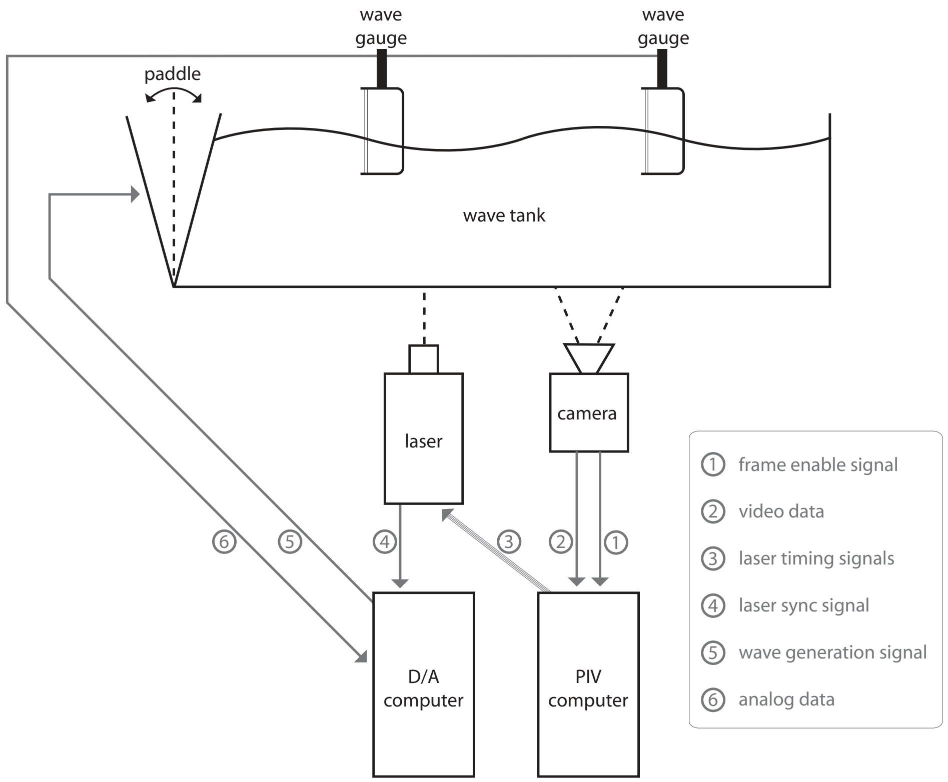

Figure A.3: Schematic showing the experimental layout and flow of the timing signals through the system for the experiments in Chapters III and IV. Line 6 represents all of the analog data which includes the wave gauges, hydrophone measurements, and the paddle feedback signal.

4) which then triggers the synchronized analog input and output of the system (lines 5 & 6).

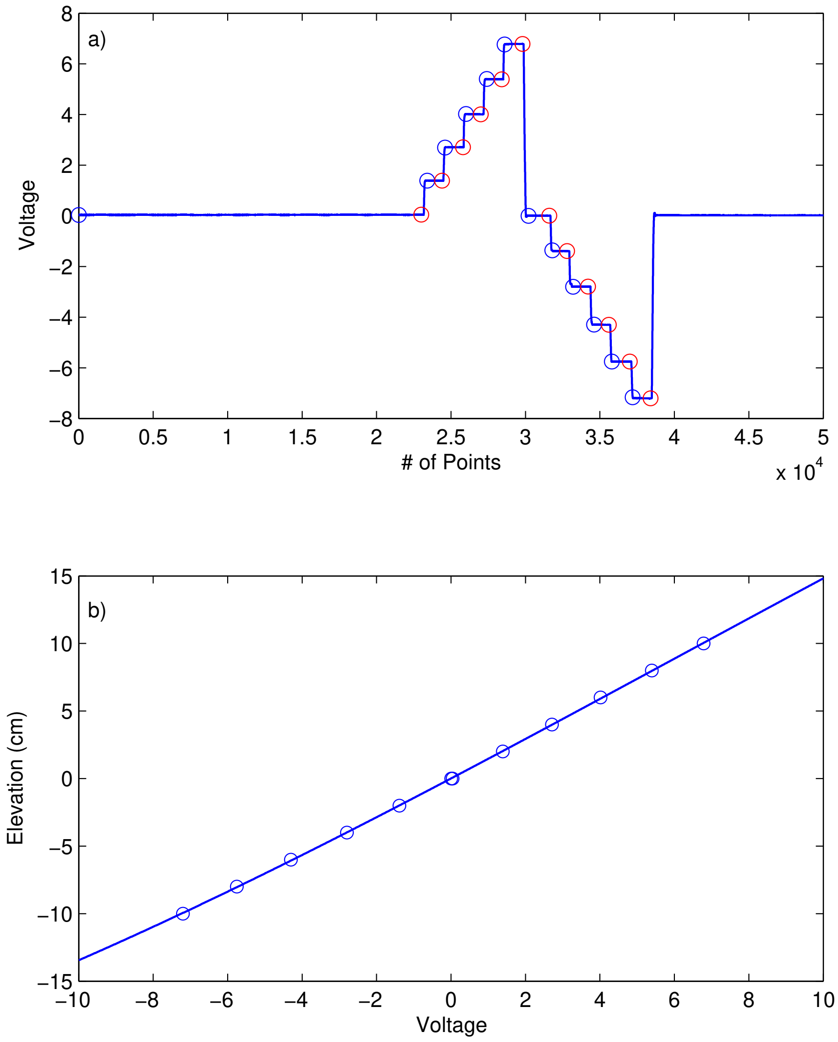

Figure A.4: Example plot of the output of the wave gauge calibration program. Figure a) is the raw output of the gauge with circles showing the start and stop locations of each plateau. Figure b) is the data plotted against the elevation along with the 3rd order polynomial fit.

# Appendix B

# Comparison of TKE density in two and three dimensions

Due to the nature of the DPIV technique, often one plane of the flow is captured and thus only two components of the flow are measured. The mean flow can be considered two-dimensional, but the turbulence is inherently three-dimensional and thus the missing component needs to be accounted for.

Svendsen (1987) presented measurements of TKE under surf-zone waves and argued that they exhibited characteristics of plane wakes based on the results of Battjes and Sakai (1981) from quasi-steady breaking. To account for the $v$ component, the relative strengths of $u'^2, v'^2, w'^2$ for a plane wake were used and the turbulent kinetic energy density, $q$, was found to be

$$q = \frac{1.33}{2}\left(\left\langle u^2 \right\rangle + \left\langle w^2 \right\rangle\right). \tag{B.1}$$

Chang and Liu (1999) used this estimate of $q$ to account for the missing component, $v$, in DPIV measurements of quasi-periodic breaking in the laboratory. RM presented laser-Doppler anemometer measurements of unsteady breaking in the laboratory and used $\langle v'^2 \rangle = \langle w'^2 \rangle$, since $\langle u'^2 \rangle > \langle w'^2 \rangle$.

Previously MVW made the assumption

$$\left\langle v^2 \right\rangle \approx \frac{1}{2}\left(\left\langle u^2 \right\rangle + \left\langle w^2 \right\rangle\right) \tag{B.2}$$

which yields

$$q = \frac{1.5}{2}\left(\left\langle u^2\right\rangle + \left\langle w^2\right\rangle\right). \tag{B.3}$$

The present measurements allow comparison of the estimate of $q$ from the longitudinal plane with the full three-dimensional field at the four cross-stream locations. To estimate the necessary scaling factor in each plane we first average vertically and then horizontally,

$$\overline{q}, \overline{q'}, \overline{q''} = \frac{1}{Z(x_2 - x_1)} \int_{x_1}^{x_2} \int_{-H}^{\eta} q, q', q'' \, \mathrm{d}z \, \mathrm{d}x \tag{B.4}$$

where $Z = \eta + H$ and $x_1$, $x_2$ are the horizontal limits of integration and the overbar denotes an area average. The two-dimensional TKE density in the longitudinal plane is given by $q' = \frac{1}{2}\langle u^2 + w^2\rangle$ and by $q'' = \frac{1}{2}\langle v^2 + w^2\rangle$ in the transverse plane. The three-dimensional turbulent kinetic energy density, $q$, is defined as

$$q = \frac{1}{2}\left(\left\langle u^2 + \frac{w|_x^2}{2}\right\rangle + \left\langle v^2 + \frac{w|_y^2}{2}\right\rangle\right) \tag{B.5}$$

where $w|_x$ and $w|_y$ are measurements of $w$ in the longitudinal and transverse planes respectively.

The relative magnitude of $u$, $v$, and $w$ change with time, so we take the temporal average to define a mean scaling factor,

$$\frac{1}{t_2 - t_1} \int_{t_1}^{t_2} \frac{\overline{q}}{\overline{q'}} \, \mathrm{d}t = 1.53. \tag{B.6}$$

$$\frac{1}{t_2 - t_1} \int_{t_1}^{t_2} \frac{\overline{q}}{\overline{q''}} \, \mathrm{d}t = 1.66. \tag{B.7}$$

A comparison between the mean value of $\overline{q(t)}$, 1.53 $\overline{q'(t)}$, and 1.66 $\overline{q''}$ is shown in figure B.1.

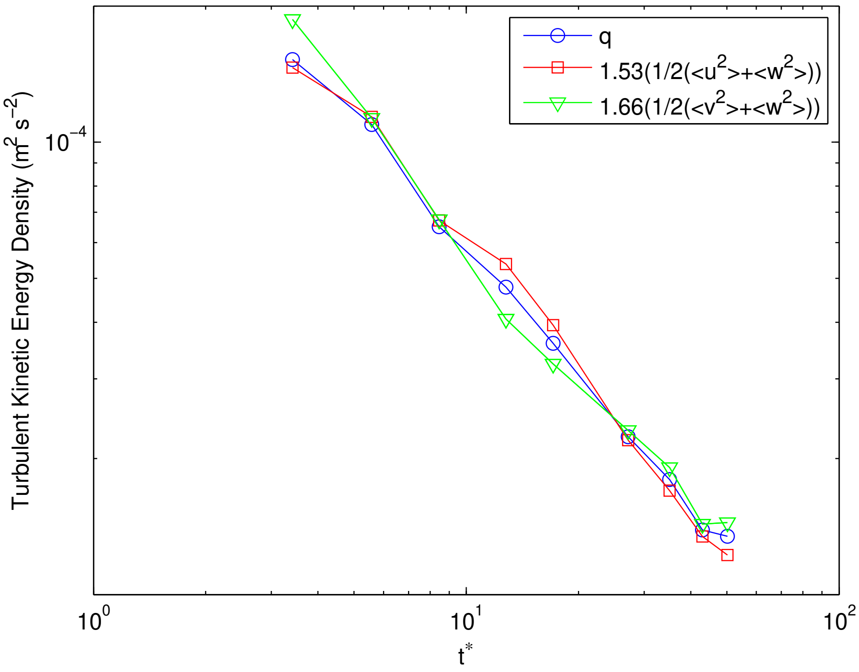

Figure B.1: Comparison between the area-averaged two-dimensional estimate in the longitudinal plane $1.53(1/2(\langle v^2\rangle + \langle w^2\rangle))$ and the transverse plane, $1.66(1/2(\langle v^2\rangle + \langle w^2\rangle))$ as well as the area-averaged three-dimensional measurement of $q(t)$ (see (B.4)).

# References

Abramowitz, M., and Stegun, I., 1964: *Handbook of Mathematical Functions*. U.S. Govt. Printing Office, Washington, D.C. 11

Banner, M. L., and Peregrine, D. H., 1993: Wave breaking in deep water. *Annu. Rev. Fluid Mech.*, **25**, 373–397. 29

Batchelor, G., 1967: *An Introduction to Fluid Dynamics*. Cambridge University Press. 67

Battjes, J., and Sakai, T., 1981: Velocity field in a steady breaker. *J. Fluid Mech.*, **111**, 421–437. 168

Bonmarin, P. J., 1989: Geometric properties of deep-water breaking waves. *J. Fluid Mech.*, **209**, 405–433. 67, 99, 119

Chan, E. S., and Melville, W. K., 1988: Deep-water plunging wave pressures on a vertical plane wall. *Proc. R. Soc. Lond. A*, **417**, 95–131. 6

Chang, K., and Liu, P. L., 1998: Velocity, acceleration, and vorticity under a breaking wave. *Phys. Fluids*, **10**, 327–329. 68

Chang, K., and Liu, P. L., 1999: Experimental investigation of turbulence generated by breaking waves in water of intermediate depth. *Phys. Fluids*, **11**, 3390–3400. 68, 119, 151, 152, 168

Chang, K., and Liu, P. L., 2000: Psuedo turbulence in piv breaking-wave measurements. *Exp. Fluids*, **29**, 331–338. 75, 79, 80, 119

Chen, G., Kharif, C., Zaleski, S., and Li, J., 1999: Two-dimensional Navier-Stokes simulation of breaking waves. *Phys. Fluids*, **11**, 121–133. 70, 99

Christensen, K. T., 2004: The influence of peak-locking errors on turbulence statistics computed from piv ensembles. *Exp. Fluids*, **36**, 484–497. doi:10.1007/s00348-003-0754-2. 75

Dabiri, D., and Gharib, M., 1997: Experimental investigation of the vorticity generation within a spilling water wave. *J. Fluid Mech.*, **330**, 113–139. 67

Dean, R. G., and Dalrymple, R. A., 1991: *Water Wave Mechanics for Engineers and Scientists*. World Scientific. 96, 162

Deane, G. B., and Stokes, D., 2002: Scale dependence of bubble creation mechanisms in breaking waves. *Nature*, **418**, 839–844. 31, 32, 43

Doron, P., Bertuccioli, L., Katz, J., and Osborn, T. R., 2001: Turbulence characteristics and dissipation estimate in the coastal ocean bottom boundary layer from piv data. *J. Phys. Oceanog.*, **31**, 2108–2131. 3, 131

Duncan, J. H., 1981: An experimental investigation of breaking waves produced by a towed hydrofoil. *Proc. R. Soc. Lond. A*, **377**, 331–348. xi, 2, 30, 31, 32, 34, 35, 36, 60, 61, 63

Duncan, J. H., 1983: The breaking and non-breaking wave resistance of a two-dimensional hydrofoil. *J. Fluid Mech.*, **126**, 507–520. 2, 30, 32, 34, 60, 63

Duncan, J. H., 2001: Spilling breakers. *Annu. Rev. Fluid Mech.*, **33**, 519–547. 29

Duncan, J. H., Philomin, V., Behres, M., and Kimmel, J., 1994: The formation of spilling breaker water waves. *Phys. Fluids*, **6**, 2558–2560. 67

Duncan, J. H., Qiao, H., Philomin, V., and Wenz, A., 1999: Gentle spilling breakers: crest profile evolution. *J. Fluid Mech.*, **379**, 191–222. 67

Hinze, J. O., 1975: *Turbulence*. McGraw-Hill. 70

Jiang, L., Perlin, M., and Schultz, W., 1998: Period tripling and energy dissipation of breaking standing waves. *J. Fluid Mech.*, **369**, 273–299. 6, 24, 25

Kolmogorov, A., 1991: The local structure of turbulence in incompressible viscous fluid for very large reynolds numbers. *Proc. R. Soc. Lond. A*, **434**, 9–13. 144

Komen, G. J., Hasselmann, S., and Hasselmann, K., 1984: On the existence of a fully developed wind-sea spectrum. *J. Phys. Oceanog.*, **14**, 1271–1285. 29

Lamarre, E., and Melville, W. K., 1991: Air entrainment and dissipation in breaking waves. *Nature*, **351**, 469–472. 31, 43, 67, 113, 160

Lin, J. C., and Rockwell, D., 1995: Evolution of a quasi-steady breaking wave. *J. Fluid Mech.*, **302**, 29–44. 67

Loewen, M. R., 1991: *Laboratory Measurements of the Sound Generated by Breaking Waves*. Ph.D. thesis, Massachusetts Institute of Technology and Woods Hole Oceanographic Institution. 43

Loewen, M. R., and Melville, W. K., 1991: Microwave backscatter and acoustic radiation from breaking waves. *J. Fluid Mech.*, **224**, 601–623. xiii, 31, 37, 38, 43, 52, 54, 55, 60, 72, 160

Longuet-Higgins, M., and Dommermuth, D., 2001a: On the breaking of standing waves by falling jets. *Phys. Fluids*, **13**, 1652–1659. 6

Longuet-Higgins, M., and Dommermuth, D., 2001b: Vertical jets from standing waves. ii. *Proc. R. Soc. Lond. A*, **457**, 2137–2149. 6

Longuet-Higgins, M., and Drazen, D., 2002: On steep gravity waves meeting a vertical wall: a triple instability. *J. Fluid Mech.*, **466**, 305–318. 1

Longuet-Higgins, M. S., 1974: Breaking waves-in deep or shallow water. In *Proc. 10th Symp. on Naval Hydrodynamics*, editors R. Cooper, and S. Doroff, 597–605. Office of Naval Research, Arlington, Virginia. 11, 41, 63, 72, 159, 162

Longuet-Higgins, M. S., 1975: Integral properties of periodic gravity waves of finite amplitude. *Proc. R. Soc. Lond. A*, **342**, 157–174. 26

Longuet-Higgins, M. S., 1992: Capillary rollers and bores. *J. Fluid Mech.*, **240**, 659–679. 67, 119

Longuet-Higgins, M. S., 1995: On the disintgration of the jet in a plunging breaker. *J. Phys. Oceanog.*, **25**, 2458–2462. 68

Longuet-Higgins, M. S., and Turner, J. S., 1974: An 'entraining plume model' of a spilling breaker. *J. Fluid Mech.*, **63**, 1–20. 63

Melville, W. K., 1994: Energy dissipation by breaking waves. *J. Phys. Oceanog.*, **24**(10), 2041–2049. xi, xiii, 2, 31, 32, 33, 35, 36, 37, 54, 55, 60, 63

Melville, W. K., 1996: The role of surface-wave breaking in air-sea interaction. *Annu. Rev. Fluid Mech.*, **28**, 279–321. 29

Melville, W. K., and Matusov, P., 2002: Distribution of breaking waves at the ocean surface. *Nature*, **417**, 58–63. 33

Melville, W. K., and Rapp, R. J., 1985: Momentum flux in breaking waves. *Nature*, **317**, 514–516. 42

Melville, W. K., Romero, L., and Kleiss, J. M., 2005: Extreme wave events in the Gulf of Tehuantepec. In *Rogue Waves, Proc. ŚAha HulikoŠaŠ Hawaiian Winter Workshop*, editors P. Müller, and D. Henderson, 23–28. 65

Melville, W. K., Veron, F., and White, C., 2002: The velocity field under breaking waves: coherent structures and turbulence. *J. Fluid Mech.*, **454**, 203–233. 32, 33, 65, 69, 75, 160

Mercer, G. N., and Roberts, A. J., 1992: Standing waves in deep water: their stability and extreme form. *Phys. Fluids A*, **4**, 259–269. 6, 8, 25

Miles, J., 1962: Transient gravity wave response to an oscillating pressure. *J. Fluid Mech.*, **13**, 145–150. 11

Nimmo Smith, W. A. M., Katz, J., and Osborn, T., 2005: On the structure of turbulence in the bottom boundary layer of the coastal ocean. *J. Phys. Oceanog.*, **35**, 72–93. 3, 131, 138

Pearson, B. R., Krogstad, P.-Å., and van de Water, W., 2002: Measurements of the turbulent energy dissipation rate. *Phys. Fluids*, **14**(3), 1288–1290. 65

Perlin, M., He, J., and Bernal, L. P., 1996: An experimental study of deep water plunging breakers. *Phys. Fluids*, **8**(9), 2365–2374. 68, 99

Phillips, O. M., 1985: Spectral and statistical properties of the equilibrium range in wind-generated gravity waves. *J. Fluid Mech.*, **156**, 505–531. 29, 30, 31, 154

Phillips, O. M., Posner, F. L., and Hansen, J. P., 2001: High range resolution radar measurements of the speed distribution of breaking events in wind-generated ocean waves: Surface impulse and wave energy dissipation rates. *J. Phys. Oceanog.*, **31**(2), 450–460. 2, 32, 33, 60

Pope, S. B., 2000: *Turbulent Flows*. Cambridge University Press. 127, 130, 144

Raffel, M., Willert, C., and Kompenhans, J., 1998: *Particle Image Velocimetry*. Springer. 75, 79

Rapp, R. J., and Melville, W. K., 1990: Laboratory measurements of deep-water breaking waves. *Phil. Trans. R. Soc. Lond. A*, **331**, 735–800. xii, 31, 33, 37, 42, 45, 51, 52, 66, 159, 160

Ryu, Y., Chang, K.-A., and Lim, H.-J., 2005: Use of bubble image velocimetery for measurement of plunging wave impinging on structure and associated greenwater. *Meas. Sci. Technol.*, **16**, 1945–1953. doi:10.1088/0957-0233/16/10/009. 115

Saddoughi, S., and Veeravalli, S., 1994: Local isotropy in turbulent boundary layers at high reynolds number. *J. Fluid Mech.*, **268**, 333–372. 3, 131, 138

Sreenivasan, K. R., 1984: On the scaling of the turbulence energy dissipation rate. *Phys. Fluids*, **27**(5), 1048–1051. 65

Sreenivasan, K. R., 1995: On the universality of the Kolmogorov constant. *Phys. Fluids*, **7**(11), 2778–2784. 144

Sullivan, P. P., McWilliams, J. C., and Melville, W. K., 2004: The oceanic boundary layer driven by wave breaking with stochastic variability. Part 1. Direct numerical simulations. *J. Fluid Mech.*, **507**, 143–174. 33, 70, 152

Svendsen, I., 1987: Analysis of surf zone turbulence. *J. Geophys. Res.*, **92**(C5), 5115–5130. 69, 151, 168

Taylor, G. I., 1935: Statistical theory of turbulence. *Proc. R. Soc. Lond. A*, **151**(873), 421–444. 126

Tennekes, H., and Lumley, J. L., 1972: *A First Course In Turbulence*. MIT Press. 86, 140

Veron, F., and Melville, W. K., 1999: Pulse-to-pulse coherent doppler measurements of waves and turbulence. *J. Atmos. Ocean. Tech.*, **16**, 1580–1597. 69, 70, 146

Willert, C. E., 1997: Stereoscopic digital particle image velocimetry for application in wind tunnel flows. *Meas. Sci. Technol.*, **8**, 1465–1479. 74